DYNAMICAL SYSTEMS APPROACH TO THE INVESTIGATION OF THERMOACOUSTIC INSTABILITIES

A THESIS

submitted by

PRIYA SUBRAMANIAN

for the award of the degree

of

DOCTOR OF PHILOSOPHY

DEPARTMENT OF AEROSPACE ENGINEERING
INDIAN INSTITUTE OF TECHNOLOGY MADRAS.

APRIL 2011

THESIS CERTIFICATE

This is to certify that the thesis titled **DYNAMICAL SYSTEMS APPROACH TO THE INVESTIGATION OF THERMOACOUSTIC INSTABILITIES**, submitted by **PRIYA SUBRAMANIAN**, to the Indian Institute of Technology, Madras, for the award of the degree of **Doctor of Philosophy**, is a bona fide record of the research work done by him under our supervision. The contents of this thesis, in full or in parts, have not been submitted to any other Institute or University for the award of any degree or diploma.

Prof. R. I. Sujith
Research Guide
Professor
Dept. of Aerospace Engineering
IIT Madras.

Place: Chennai

Date: 30th April 2011

to appa, ambi and ammai

ACKNOWLEDGEMENTS

During my doctoral studies I have experienced a multitude of serendipitous events. A chain of events in which many people were at the right time, at the right place and found the right words to make me see. Chief among them has been my guide, Professor R. I. Sujith. He has shaped my academic life, both in the recent past and in my future, with his unflinching faith in me. I shall strive to live up to what he sees in me.

I am much indebted to the members of my doctoral committee, Professor S. R. Chakravarthy, Professor M. Ramakrishna, Professor K. Srinivasan and Professor P. Chandramouli for their valuable suggestions and guidance during the course of my doctoral work. I would also like to thank the constant support that I have received from Professor J. Kurian, Professor P. Sriram and Professor K. Bhaskar who have helped and guided me in their capacity as the Head of the Department of Aerospace Engineering. I have been constantly supported by Mrs. Mekala, Mr. Sundar, Mr. Stephen, Shankar Sir, Mr. Kennedy and Mr. Shiva at the Department of Aerospace Engineering, who have made my stay at IIT Madras very pleasant.

I would like to thank Dr. P. Wahi of IIT Kanpur for his Zen style guidance; which consists of showing me the way and then waiting for me to reach the solution by myself. I am grateful to Professor W. Polifke for his faith in me, his generous support during my visits to TU Munich and many suggestions over the years. I am much obliged to Professor N. Gupte for introducing me to nonlinear dynamics. Her teaching and support have changed the phase portrait of my life. I am also indebted to Professor P. J. Schmid and Professor R. Govindarajan for introducing me to the field of fluid dynamics and stability, their critical comments and enthusiastic support of this work. I thank Professor M. K. Verma for his generous hospitality during my visits to IIT Kanpur and Dr. M. P. Juniper for many fruitful discussions. I thank Mr. A. Saha at IIT Kanpur for helping me to use DDEBIFTOOL and for his collaboration in the application of the method of multiple scales. I am grateful for the opportunity I had during my dissertation to work

with with Dr. F. Selimefendigil at TU Munich.

I would like to acknowledge the support of all the people who shared the lab with me over the years. Particularly, I thank the old timers Manav, Koushik, Kushal, Varun and Rahul who taught me about research by their own approaches to it. I have learnt a lot from my discussions with Guru, Balaji, David, Vikrant, Bharat, Sharath, Aditya, Lipika, Girish sir and Rana sir. I am lucky to have found friends who share their work and life with me in Vinu, Sathesh, Joseph, Ralf, Thomas, Vivek, Vishnu, Pushkarini, Tharun, Devendra, Ramgopal and Raji. My life has been enriched in many ways from the lessons that I have learnt from them. I thank Vinu for showing me the strength of silence, Sathesh for teaching me that tremendous effort goes in to make things look effortless, Joseph for inspiring me with his dogged pursuit of knowledge and Ralf for reminding me to dot my i's and cross my t's.

ABSTRACT

KEYWORDS: thermoacoustic instabilities; dynamical systems; non-normality; transient growth; sub-critical transition to instability; numerical continuation; period-doubling; quasiperiodicity; routes to chaos.

Thermoacoustic instabilities severely restrict the operating regimes and reduce the life of gas turbines as they induce large amplitude pressure fluctuations. During instability, excessive vibrations and oscillatory thermal loads occur in the system. In order to find safe operating ranges, where instabilities can be avoided, stability analysis of thermoacoustic systems are performed. Thermoacoustic instabilities are analyzed using models of thermoacoustic systems. Two time domain models of practical thermoacoustic systems are considered in the present investigation. First, a Rijke tube model in which the heat release rate is modelled in terms of time delayed responses to acoustic perturbations. The second model is of a ducted premixed flame system in which a partial differential equation is used to describe the evolution of the source of unsteady heat release rate. Linear stability of thermoacoustic systems is performed using eigenvalues. Classical linear stability analysis based on eigenvalues is a robust estimator of the asymptotic behavior of linear systems. However, thermoacoustic interaction is non-normal and the associated eigenvectors are non-normal to each other. Transient growth can occur due to the non-orthogonal eigenvectors and therefore the investigation of stability in thermoacoustic systems must adopt a non-modal approach.

A horizontal Rijke tube model whose evolution is described by a set of delay differential equations is considered. Analytical estimates of bifurcation points are employed to identify the regions of bistability. The nature of the Hopf bifurcation along with the estimates of the stability and amplitude of periodic states near the Hopf point are obtained using the method of multiple scales. Estimates of fold bifurcation points are obtained by employing the method of harmonic balance. Stability boundaries and bifurcation plots are obtained using numerical continuation methods. This thesis is the first

work in which numerical continuation methods have been applied to the investigation of thermoacoustic systems with an explicit time delay. In this model, transition to instability occurs via sub-critical Hopf bifurcation. The regions of global stability, global instability and bistability are characterized. Further, interesting dynamical behavior such as co-existing multiple attractors, quasiperiodic behavior and period doubling route to chaos are observed. Results of linear stability boundaries and bifurcation behavior from this reduced order model are compared with experiments.

A ducted premixed flame system is modelled using the acoustic equations for momentum and energy, together with the equation for the evolution of the flame front obtained from the kinematic *G*-equation. As the unsteady heat addition acts as a volumetric source, the flame front is modelled as a distribution of monopole sources. The state space variables in the model include the monopole source strengths in addition to the acoustic variables. Inclusion of these variables in the state space is essential to account for the transient growth due to non-normality. Thus, the energy due to fluctuations considered in the this analysis accounts for the energy of the monopole sources in addition to the acoustic energy. The optimal initial condition for transient growth, has significant projections along the strength of the monopole distribution in addition to projections along the acoustic variables of velocity and pressure. A parametric study of the variation in transient growth due to change in parameters such as flame location and flame angle is performed.

Comparison of linear and corresponding nonlinear evolutions highlights the role of transient growth in sub-critical transition to instability. The notion of phase between acoustic pressure and heat release rate as an indicator of stability is examined. Stability boundaries and bifurcation plots for the ducted premixed flame system are obtained, where both sub- and super-critical Hopf bifurcations are observed. In both the analysis of a horizontal Rijke tube and a ducted premixed flame, the nature of the asymptotic states of the system are identified using tools from dynamical systems' theory. It is observed that a system can exhibit different routes to chaos such as period doubling and Ruelle-Taken's routes for different configurations.

TABLE OF CONTENTS

LIST OF TABLES

LIST OF FIGURES

ABBREVIATIONS

ODE	Ordinary Differential Equation
DDE	Delay Differential Equation
SVD	Singular Value Decomposition
TVD	Total Variation Diminishing
WENO	Weighted Essentially Non-Oscillatory scheme
CFL	Courant-Friedrichs-Lewy number

NOTATION

a	radius of duct
b	radius of burner
c_0	speed of sound
c_1, c_2	damping coefficients
d_w	diameter of wire
e	eigenvector
l_c	radius of wire
p	pressure
q	heat release
s	pseudoarclength
t	time
t_{max}	time at which maximum amplification occurs
u	velocity
x	radial co-ordinate
y	axial co-ordinate
y_f	location of unsteady heat source along the duct
B	linear operator
E	energy due to fluctuations
EV	matrix of eigenvectors
F	nonlinear operator
F_χ	Jacobian matrix
G_{max}	growth factor
H_i	monopole strength averaged over the cross-sectional area of duct
K	non-dimensional heater power
L	length of duct
L_W	length of wire
M	Mach number
Pe	Peclet number
R	resultant
Re	Reynolds number
S	cross-sectional area
S_L	laminar flame speed
S_i	monopole strength per unit length
T	time period
T_W	temperature of wire
U	matrix of left singular vectors
V	matrix of right singular vectors

α	angle that the unperturbed flame makes with the flow
χ	vector of state variables
γ	ratio of specific heat coefficients
δ	Delta function
ϵ	amplitude of perturbation
$\eta_j, \dot{\eta}_j/j\pi$	temporal coefficients of jth Galerkin mode
λ	eigenvalues
λ_1	Lyapunov exponent
μ	vector of parameters
ϕ	equivalence ratio
$\triangle q_R$	heat of reaction per unit mass of unburnt mixture
σ	singular value
τ	time lag
θ	phase between acoustic pressure and unsteady heat release rate
ξ	signed distance of perturbed flame shape from unperturbed state
$\Gamma(\chi_0, \mu_0)$	solution component connected to the solution (χ_0, μ_0)
Σ	matrix of singular values
$\Phi(T)$	Monodromy matrix at the fundamental period T
$\Gamma(\chi_0, \mu_0)$	solution component connected to the solution (χ_0, μ_0)
$\alpha_\epsilon(B)$	ϵ-pseudospectral abscissa of B
$\omega(B)$	numerical abscissa of B
$\alpha(B)$	spectral abscissa of B
$\kappa(B)$	Kreiss constant for B
$\varphi(B)$	upper bound for transient growth of B
$(\tilde{x})$	dimensional quantity
$(\bar{x})$	mean of quantity x
$(\dot{x})$	rate of change of x with time
$(x)'$	fluctuating part of x
$Re(x)$	real part of quantity x
$Im(x)$	imaginary part of quantity x
$(x)^T$	transpose of matrix x
$(x)_f$	quantity x at the location of heat source
$(x)_i$	quantity x at the ith value
$(x)_0$	quantity x at unperturbed state
$(x)_c$	quantity x non-dimensionalised to combustion scale
$(x)_a$	quantity x non-dimensionalised to acoustic scale
$\|x\|$	L^2 norm of vector x
$\|x\|$	modulus/absolute of quantity x

CHAPTER 1

INTRODUCTION

1.1 Motivation

Thermoacoustic systems consist of an acoustic field along with a source of unsteady heat release rate. For example, the source of heat release rate fluctuations can be a flame located within the duct as found in gas turbines or an electrically heated mesh as in the case of a Rijke tube. Unsteady flow through the duct interacts with the source of heat release rate and causes it to fluctuate. These heat release rate fluctuations can further act as a source of acoustic fluctuations and the coupled system can reach self-sustained large amplitude oscillations. These self-sustained oscillations are termed as thermoacoustic instability. Thermoacoustic instabilities induce large amplitude pressure fluctuations and are therefore responsible for excessive vibrations and oscillatory thermal loads on the system. They can even cause flame blowout to occur. Thermoacoustic instabilities severely restrict the operating regimes and reduce the life of gas turbines. Therefore, the need to avoid thermoacoustic instability plays a significant role in the development of combustors for rockets and gas turbines (McManus *et al.*, 1993).

The interaction between unsteady flow and heat release rate fluctuations can occur in many ways. The unsteady flow velocity can directly modulate the surface area of the flame which can lead to heat release rate fluctuations as investigated by Boyer and Quinard (1990). Fluctuations in flow rates of the reactants can give rise to equivalence ratio fluctuations which in turn can cause unsteady heat release rate (Lieuwen and Zinn, 1998). Acoustic oscillations can also modulate the burn rate of the flame directly (Wu *et al.*, 2003). The methods described above list some of the ways in which the acoustic field directly interacts with the source of heat release rate fluctuations. However, this interaction can also happen indirectly as follows. Flow within combustors have shear. In a shear flow, acoustic oscillations can give rise to instability waves which can amplify the roll up of the shear layer. Later the shear layer breaks down into small scale motions

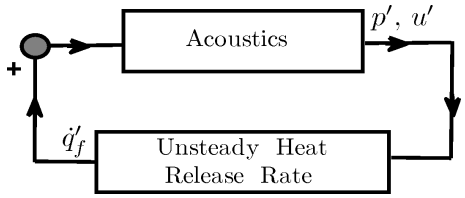

Figure 1.1: Feedback loop in thermoacoustic systems.

giving rise to unsteady heat release rate (Poinsot *et al.*, 1987). This indirect interaction can also cause instability in thermoacoustic systems.

An illustration of the interaction between acoustic field and the source of unsteady heat release rate is given in Fig. 1.1. The fluctuations in velocity u' and pressure p' due to the acoustic field can cause heat release rate oscillations $\dot{q}'_f$. Lord Rayleigh (1878) made the observation that if the heat release rate fluctuations $\dot{q}'_f$ occur at the time of greatest compression, i.e. when acoustic pressure is maximum, the amplitude of the acoustic oscillation increases. Assuming the convention that heat added to the system is positive, Rayleigh's observation states that for maximum driving, both the evolutions of acoustic pressure and the unsteady heat release rate must reach their respective maximums at the same time.

When the phase angle θ between the acoustic pressure and unsteady heat release rate is between the range $-90^\circ < \theta < 90^\circ$, it indicates addition of energy to the acoustic oscillations (acoustic driving). During thermoacoustic interaction, energy losses can occur due to viscous dissipation, radiation from open ends, heat transfer, etc (acoustic damping). If the energy added to acoustic oscillations from unsteady heat release rate is more than the energy losses, the system becomes unstable and the oscillation amplitude increases. Interactions of the unsteady heat release rate with the acoustic field drive thermoacoustic instability over a time period T in a system of volume V, if the Rayleigh criterion given below is satisfied (Putnam *et al.*, 1986; Sterling and Zukowski, 1991; Zinn and Lieuwen, 2006).

$$\int_{dV} \int_{T} p'(t)\dot{q}'_f(t)\, dt\, dV > \text{Damping}\,. \tag{1.1}$$

Thermoacoustic instabilities are analyzed using models of thermoacoustic systems. In general, models of thermoacoustic systems can include nonlinear effects in the dy-

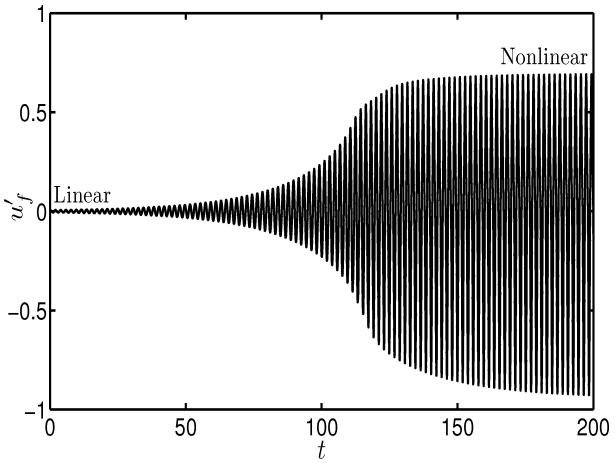

Figure 1.2: Evolution of acoustic velocity to a limit cycle in a linearly unstable Rijke tube system.

namics of heat release rate and also in acoustic wave propagation. Large amplitude fluctuations are observed in solid rocket motors of the order of $10 - 50\%$ of the mean pressure (Bloomshield *et al.*, 1997). Therefore, nonlinear stability analysis of solid rocket motors must include the nonlinear effects in acoustic wave propagation such as steepening of a compression wave to form a shock (Yang *et al.*, 1990; Culick, 2006; Mariappan and Sujith, 2010*b*). Alternatively, thermoacoustic systems such as laboratory combustors or gas turbine combustors are characterized with amplitudes of the acoustic pressure fluctuations less than 5% of the mean pressure (Lieuwen, 2002) which are not significant enough to introduce nonlinear gas dynamic effects (Dowling, 1997). Thus stability analysis of these thermoacoustic systems include only nonlinear effects in the heat release rate dynamics.

A typical evolution of acoustic velocity oscillations in a horizontal Rijke tube is shown in Fig. 1.2. The system is linearly unstable and it is observed that the oscillations grow from a small amplitude initial condition to self-sustained oscillations. During the period of initial growth when the amplitude of the oscillations is small, the effect of the nonlinear terms in the system model can be assumed to be negligible. The evolution of the system can then be approximated using a set of linear differential equations. This set of equations can be recast as

$$\frac{d\chi}{dt} = B\chi\,, \tag{1.2}$$

where B is the linear operator and χ is the vector of state variables. Classical linear

stability analysis investigates the eigenvalues λ_i of this linear operator B which are in general complex numbers. The real part of λ_i indicates the growth rate and the imaginary part indicates the frequency of oscillations. If all the eigenvalues λ_i of B have negative real parts, the evolution decays and the system is linearly stable. If one or more of λ_i have positive real part, the eigenvectors corresponding to the frequencies specified by the value of $Im(\lambda_i)$, grow at the rates specified by the magnitudes of the corresponding $Re(\lambda_i)$ and the system is linearly unstable.

The linear operator B is a function of the system parameters. Therefore, the eigenvalues λ_i change when the values of the system parameters are varied. When the real part of λ_i changes from negative to positive value, the nature of stability of the system changes and evolutions change qualitatively. This qualitative change in stability is called a bifurcation. Parameter combinations at which the system loses linear stability form the linear stability boundary. Classical linear stability analysis can be used to identify the frequency and growth rate at the loss of linear stability. Using this information, linear stability boundaries of the system can be determined for different system configurations.

During instability, the amplitude of oscillations grows exponentially to large values and reaches a constant value as shown in Fig. 1.2, when the acoustic driving and acoustic damping balance each other. This constant amplitude oscillation is called as a limit cycle oscillation. Nonlinear effects become significant at large amplitudes of oscillations. The amplitude of limit cycles cannot be predicted by a linear stability analysis. Further, during large amplitude evolutions, the frequency of oscillations can change over time. However, accurate estimation of the amplitude and frequency of acoustic oscillations during limit cycle is important from the design point of view for gas turbines (Zinn and Lieuwen, 2006). Therefore a nonlinear stability analysis of thermoacoustic systems is required. Results from nonlinear stability analysis are collected in a visual representation of the system state for different parameter values, i.e. a bifurcation plot. The next section lists in detail previous works related to both linear and nonlinear stability analysis of thermoacoustic systems.

1.2 Stability analysis of thermoacoustic systems

Stability analysis of thermoacoustic systems have been performed in order to understand the mechanisms which cause thermoacoustic instability, to establish stable ranges of operation and to identify limit cycle characteristics. Thermoacoustic system are governed by the acoustic equations for momentum and energy along with a model for the unsteady heat release rate. Heat release rate fluctuations can be modelled using either a response function (Schuller *et al.*, 2003; Dowling, 1997) or using a separate evolution equation Dowling (1999). The model of a thermoacoustic system consists of a set of partial differential equations. These partial differential equations are converted into ordinary differential equations by either a modal expansion (Zinn and Lores, 1971; McManus *et al.*, 1993) or by spatial discretisation (Schmid and Henningson, 2001) which are then linearized. Classical linear stability analysis investigates the eigenvalues of the set of linear equations to determine the stability of the system. Nonlinear stability analysis of thermoacoustic system are performed using the describing function technique (Dowling, 1997; Noiray *et al.*, 2008). In the describing function technique, the quasi-linear approximation of the unsteady heat release rate response is used as the source term in the acoustic energy equation. In the following subsections, stability analysis of different thermoacoustic systems are briefly reviewed. Both linear and nonlinear stability analysis are considered for each system and the results of linear stability analysis are listed before the results of nonlinear stability analysis in each subsection.

1.2.1 Rijke tube

The Rijke tube consists of a source of heat release rate fluctuations such as an electrical heater located within a duct which is open at both ends (Rijke, 1859). The power supplied to the heater serves to cause thermoacoustic oscillations in the Rijke tube. Self-sustained thermoacoustic oscillations were observed in a Rijke tube when the heater was positioned at certain axial locations of the tube with the heater power above a threshold power level (Rijke, 1859). An explanation for the occurrence of this instability in a Rijke tube was given by Rayleigh (1878). He explained that instability occurs when the heater is placed at locations where the unsteady heat release rate is in phase with the

acoustic pressure oscillations. Carvalho *et al.* (1989) used a linear model to describe the unsteady heat release rate due to acoustic velocity at the heater. The excitation of different modes at different axial locations of the heater was predicted using a linear stability analysis. Stability analysis of the Rijke tube with multiple sources and complex geometries was performed by Bittani *et al.* (2002).

The pressure fluctuations arising during instability in a Rijke tube are not significant enough to include the nonlinear effects in acoustic wave propagation. Therefore, only the nonlinearity in the heat release rate response of the heater to acoustic velocity perturbations is considered. A nonlinear stability analysis of a Rijke tube was performed by Kwon and Lee (1985). Computational fluid dynamic (CFD) technique based analysis were also used to study Rijke tube oscillations with the heat source being considered as a heated flat plate (Hantschk and Vortmeyer, 1999) or as a circular cylinder (Mariappan and Sujith, 2010*a*). Hantschk and Vortmeyer (1999) showed that the limit cycle amplitudes during instability are a function of the nonlinear response of the heater. Heckl (1990) performed both theoretical and experimental analysis of instabilities in a Rijke tube. She concluded that flow reversal occurring at the heater and losses from the ends of the duct were the two deciding factors in determining limit cycle amplitude. The transfer functions obtained from CFD simulations of flow around heated cylinders (Kwon and Lee, 1985) have been used for nonlinear stability analysis of a Rijke tube (Matveev, 2003*b*). Matveev (2003*b*) also performed experiments to obtain stability maps and bifurcation plots for an electrically heated horizontal Rijke tube.

1.2.2 Premixed flame

The model of a ducted premixed flame can be used to investigate thermoacoustic instabilities in laboratory combustors. The stability characteristics of a ducted premixed flame can be investigated using a kinematic approach to model the flame front (Kerstein *et al.*, 1988). Boyer and Quinard (1990) used this kinematic model of a premixed flame to obtain the response of the premixed flame front to acoustic velocity perturbations. Bloxsidge *et al.* (1988) performed a linear stability analysis for a premixed flame stabilized in a duct. Predictions for the frequency and growth rate of oscillations near the

onset of instability were obtained from this linear analysis which matched the experimental results of Langhorne (1988). The analysis by Bloxsidge *et al.* (1988) indicated that the relationship between heat release rate oscillations and the acoustic velocity fluctuations at the flame front is a function of the frequency of oscillations and the mean flow.

Fleifil *et al.* (1996) investigated the response of a premixed flame front to different acoustic frequencies and observed that low frequency oscillations have a strong impact on the heat release rate oscillations. This relationship between the response of the flame front and acoustic velocity perturbations can be obtained as transfer functions in the linear regime. The premixed flame is forced at different frequencies ω with an acoustic velocity amplitude $\epsilon = u'/\bar{u}$. The resulting fluctuations in heat release rate $\dot{q}'_f$ over a steady heat release rate of $\dot{\bar{q}}_f$ are measured. Transfer function TF of a flame is complex valued function of frequency which is calculated as

$$TF(f) = \frac{\dot{q}'_f/\dot{\bar{q}}_f}{u'/\bar{u}}\,. \tag{1.3}$$

Schuller *et al.* (2003) used a linear model for the flame front and derived transfer functions for conical and V-flame configurations. The derived analytical expressions for linear transfer functions matched transfer functions obtained from numerical simulations. Experiments were performed for both V-flame (Durox *et al.*, 2005) and conical flame (Birbaud *et al.*, 2006) configurations to obtain their transfer function characteristics. Annaswamy *et al.* (1997) employed an evolution equation for the heat release rate which is valid in the linear regime in addition to the evolution of acoustic variables to study the stability of a ducted premixed flame.

Nonlinear stability analysis of premixed flames include the nonlinearity in the response of the unsteady heat release rate to acoustic velocity perturbations. This is because, during instabilities in premixed combustors, the acoustic pressure fluctuations encountered are not large enough to cause nonlinear effects of acoustic wave propagation to become significant (Peracchio and Proscia, 1999). Dowling (1997) proposed a nonlinear model for the heat release rate response of a premixed flame, which saturates when the acoustic velocity amplitude at the flame holder approaches the mean flow

velocity. Experimental investigations of the nonlinear response of a ducted, conical, laminar premixed flame (Karimi *et al.*, 2009) and an ensemble of anchored premixed flames (Noiray *et al.*, 2006) subjected to acoustic excitation of varying amplitudes were performed to characterize the transfer function of the premixed flame. Noiray *et al.* (2008) used the amplitude dependent transfer functions to investigate the stability of a ducted premixed flame system using the describing function approach.

Dowling (1999) used the front-tracking equation to model the evolution of a premixed flame in the investigation of the thermoacoustic instability in a ducted premixed flame. The equations for the acoustic field are evolved together with the nonlinear front tracking equation for the flame. During instability, large amplitude oscillations can occur which can cause the flame to flashback for part of the cycle. Flash back of the flame occurs when the mean velocity is lower than the speed at which the flame front is propagating into the unburnt mixture, i.e. the laminar flame speed. Dowling (1999) modelled a ducted premixed flame which can capture flashback during part of the cycle and used this model to investigate nonlinear self-excited oscillations in the system. Thermoacoustic instabilities are also encountered in cases when the flame is not premixed. The next subsection details some of the literature which investigate thermoacoustic instability in non-premixed or diffusion flames.

1.2.3 Non-premixed flames

Investigations of non-premixed combustion systems or diffusion flames use the classical Burke-Schumann geometry (Burke and Schumann, 1928) for analysis. This model neglects stream-wise diffusion to approximate the diffusion flame within a narrow zone or surface. Unsteady analysis of diffusion flames was performed by Cuenot *et al.* (2000) using laminar flamelet models. Response of the diffusion flame system to acoustic forcing was studied experimentally (Hertzberg, 1997; Buckmaster, 2002). Nonlinear analysis of diffusion flames listed below consider only the nonlinearity in the heat release rate response to acoustic velocity perturbations. This is because, similar to the premixed combustors, amplitude of the limit cycle oscillations are not large enough to induce nonlinear effects in acoustic wave propagation in diffusion flame driven ther-

moacoustic systems.

Tyagi *et al.* (2007*a*) highlighted the nonlinearity in the combustion response of non-premixed flames to velocity perturbations. Results obtained using the infinite rate chemistry were compared with results obtained when the effects of finite rate chemistry were included. The nonlinear response of the diffusion flame system to mass fraction was investigated using analytical methods by Tyagi *et al.* (2007*b*). They also used numerical methods to analyze the nonlinear response of a diffusion flame to acoustic velocity oscillations. Balasubramanian and Sujith (2008*b*) adopted an analytical approach to investigate the effect of velocity fluctuations on the diffusion flame response and concluded that the response has an exponential dependence on the amplitude of fluctuations. This heuristic model for the unsteady heat release rate developed by Balasubramanian and Sujith (2008*b*), when combined with an acoustic model, exhibits many nonlinear phenomena such as saturation and dominant mode change during evolution Yoon *et al.* (2001).

1.2.4 Thermoacoustic engines

Thermoacoustic instabilities are also observed in thermoacoustic engines where the temperature gradient across the stack can lead to instabilities (Swift, 1988). Linear stability analysis of a thermoacoustic engine was performed by Atchley (1992) whose analysis of a helium-filled prime mover matched quality factors for the first three longitudinal modes of oscillations obtained from experiments. Watanabe *et al.* (1997) performed a linear stability analysis of quasi- one-dimensional model of a thermoacoustic engine. A time domain model of the system was formulated and predictions from the model were compared with data from experiments.

Yuan *et al.* (1997) performed the nonlinear stability analysis of the same quasi-one-dimensional model of a thermoacoustic engine. The results of the nonlinear model when compared with experiments were able to describe the growth and saturation of oscillations during instability. A two-dimensional model for thermoacoustic engines was developed by Hamilton *et al.* (2002) who employed it for the investigation of nonlinear oscillations in a thermoacoustic engine. Recently, a low Mach number analysis of ther-

moacoustic engines was performed by Hireche *et al.* (2010). This time-domain model employs a singular perturbation technique to reduce computational effort required to model the stack and captured transient processes when amplitude grows before reaching a steady state.

1.2.5 Solid rocket motors

Analysis of thermoacoustic instabilities in solid rocket motors (SRMs) has been an area of interest as they can resonate with structural modes of the rocket, cause melting of combustor walls and can damage the payload with excessive vibrations (Sutton, 2001). Linearized equations for thermoacoustic instability in solid rocket motors were investigated by Culick (1963). Complex frequencies were obtained for the instability which can charaterise both the frequency of oscillations and its growth rate. Linear response functions for the propellant response to oscillations in the acoustic variables were obtained to investigate thermoacoustic instability of the solid rocket motor. Admittance functions were obtained by (Culick, 1968) which related the fluctuations in mass addition rate were related to acoustic velocity and pressure fluctuations. The admittance function was experimentally obtained by Price (1984). Inclusion of other phenomena such as vorticity (Flandro, 1995*a*) and flow turning (Flandro, 1995*b*) were also performed in the linear stability analysis of solid rocket motors.

In contrast to other thermoacoustic systems described previously in subsections 1.2.1 to 1.2.4, nonlinear effects due to acoustic wave propagation cannot be ignored in solid rocket motors. Culick (1976) included the nonlinear gas dynamic effects and obtained an analytical condition for the existence of limit cycle oscillations. Nonlinearities in the response of propellant to acoustic perturbations were also included by Levine and Baum (1993) to analyze the stability of solid rocket motors. Culick (1994) showed that nonlinear gas dynamic effects are not sufficient to cause triggering. Wicker *et al.* (1996) included nonlinear coupling between unsteady burn rate and acoustic variables to demonstrate the possibility of triggered instability. Jahnke and Culick (1994) applied the continuation methods from dynamical systems' theory to characterize instabilities in solid rocket motors. Pitchfork and torus bifurcations were observed in this analysis.

Ananthkrishnan *et al.* (2005) addressed the problem of modal truncation in the determination of stability in solid rocket motors. Their model for a solid rocket motor included nonlinear combustion response with a velocity coupling term and was seen to reproduce sub-critical transition to instability observed in experiments.

1.2.6 Summary of review on stability analysis

The above review is incomplete and serves only to introduce previously adopted approaches to stability analysis in thermoacoustic systems. Linear analysis of stability has been performed using the classical approach of examining the eigenvalues of the linear set of ordinary differential equations obtained for the system. If all eigenvalues were negative, the system was considered to be stable to perturbations. Nonlinear stability analysis has been performed using both a response function for the nonlinear heat release rate model (Dowling, 1997) or using a nonlinear evolution equation (Dowling, 1999) to model the unsteady heat release rate. Nonlinear stability analysis is necessary to characterize the asymptotic state of system during instability. Also, an interesting dynamical behavior observed in solid rocket motors when a stable system became 'triggered' to instability with a large amplitude initial condition. This behavior is discussed in the next section.

1.3 Sub-critical transition to instability

The stability of a system changes from stable to unstable when a system parameter is varied. This change in stability can occur in one of two ways. Super-critical transition to instability is observed when the stability of the system at a given configuration does not depend on the initial condition. Sub-critical transition to instability occurs when a linearly stable system becomes unstable and asymptotically reach another state for suitable initial conditions (Hillborn, 1994). Wicker *et al.* (1996) defined triggered instability as

"Triggered instability refers to initiation of unstable pressure oscillations by a finite amplitude pulse in a system that is otherwise stable to small perturbations."

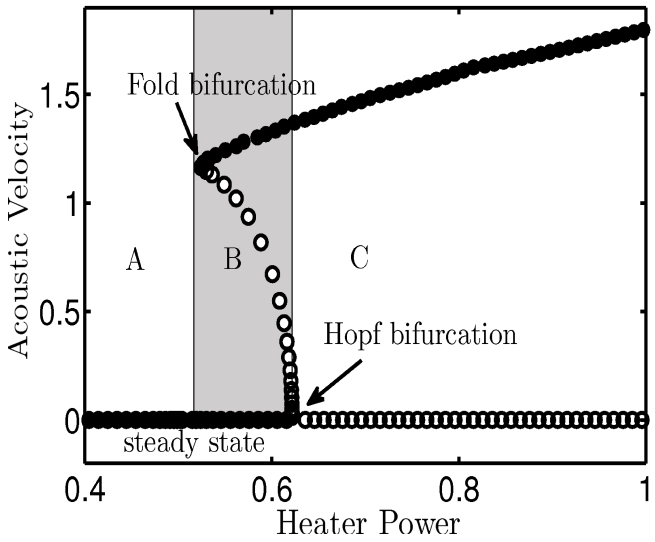

Figure 1.3: Bifurcation plot for the variation of heater power in a horizontal Rijke tube displaying sub-critical transition to instability. Globally stable (Region A), globally unstable (Region C) and bistable (Region B) are marked.

A typical bifurcation plot of a horizontal Rijke tube is shown in Fig. 1.3 in which a measure of the acoustic velocity of the system is plotted as a function of the heater power. The bifurcation plots exhibits sub-critical transition to instability and the range of heater power can be divided into three different regions. In the region marked by A, perturbations of any magnitude decay with time. This region is therefore known as the region of global stability. The region marked by C is linearly unstable and any perturbation in this region causes the system to reach a limit cycle. Region C is also called the region of global instability. In region B shaded in grey, the system can reach either a steady state or limit cycle oscillations depending on the amplitude of the initial condition. As two stable states of the system co-exist, this region is called as the region of bistability. In contrast, super-critical transition to instability consists of only regions A and C with no region of bistability between them.

In Fig. 1.3 the solid circles indicate stable solutions and hollow circles indicate unstable solutions. The unstable solutions are not observed as asymptotic states of the system but are the projections of the unstable limit cycles on the plane of the bifurcation plot. An initial condition above the value given by the these unstable solutions will cause the system to become unstable and evolve to limit cycle oscillation. Therefore, this type of triggered instability is observed as a hysteresis loop in experiments. For smooth variation of the parameter, transition occurs at different parameter values based

on the current state of the system as stable or unstable. In systems with hysteresis, the range of parameters for which the system is stable becomes a function of the amplitude of the perturbation. This sensitivity to the amplitude of the initial perturbation results in difference between the stability boundaries determined from a linear and nonlinear analysis. Hysteretic behavior is also observed in thermoacoustic systems such as the Rijke tube (Matveev, 2003*b*) and premixed combustors (Lieuwen, 2002) in addition to solid rocket motors. Experiments of a premixed combustor exhibited both sub-critical and super-critical transition to instability were observed (Lieuwen, 2002).

Lieuwen (2002) also notes that triggering does not always require a large amplitude initial perturbation to make the system reach a limit cycle. The system can evolve to a limit cycle from a small but finite amplitude initial condition which is of the level of noise in the system. This behavior is compared to hydrodynamic stability of a laminar Poiseuille flow. To quote Zinn and Lieuwen (2006),

" Although large-amplitude disturbances are generally required to initiate unstable oscillations in nonlinearly unstable systems, a system may be nonlinearly unstable at low-amplitude disturbances that are of the order of the background noise level. This scenario is somewhat analogous to the hydrodynamic stability of a laminar Poiseuille flow, which is linearly stable but becomes increasingly susceptible to destabilization by nonlinear mechanisms with increasing Reynolds numbers."

The next section explores the linear mechanism of non-normality and the transient growth resulting from non-normality which causes Poiseuille flow to become more susceptible to instability. This same mechanism can cause sub-critical transition to instability in thermoacoustic systems from a small but finite amplitude initial condition. The phenomenon of non-normality causes finite time amplification of perturbations in a system. It was first investigated in the context of meteorological systems by Farrell (1988*a*) and Farrell and Ioannou (1993). Parallel investigations into the transition to turbulence in laboratory shear flows were investigated (Trefethen *et al.*, 1993; Chagelishvili *et al.*, 1994, 1996). The non-normal nature of the shear flows has been associated with the mechanism of sub-critical transition to instability or bypass transition (Farrell, 1988*b*). The next section lists literature which investigate non-normal effects in the occurrence of hydrodynamic instabilities and thermoacoustic instabilities.

1.4 Non-normality

Hydrodynamic instability is of interest in diverse fields such as engineering, meteorological, oceanography and astrophysical systems as they are governed by the mechanics of fluid flow (Drazin and Reid, 2004). Hydrodynamic stability in viscous shear flows has been investigated using classical linear stability analysis of the Orr-Sommerfeld equation. Critical Reynolds numbers for transition to instability in plane Poiseuille flow has been calculated using this method to be $Re = 5770$ (Orzag, 1971). However, experimentally obtained values for this critical Reynolds number was found to vary between $1035 < Re < 8000$ (Gustavsson, 1981). Gustavsson (1981) attributed this discrepancy between calculated and observed critical Reynolds numbers, to the normal mode assumption used in classical stability analysis. Classical linear stability analysis using eigenvalues describes only the asymptotic state of the evolution of a system. Therefore, it is incapable of capturing transient behavior of the system. Relaxation of the normal mode assumption in stability analysis can give rise to linear mechanisms which can cause short-time algebraic growth of disturbances. If the transient growth is large enough to cause nonlinear effects to become significant, the system can transition to instability (Schmid, 2007). This non-modal approach to stability analysis has been adopted to explain transition to instability in hydrodynamic flows (Butler and Farrell, 1992; Reddy and Henningson, 1993; Schmid and Henningson, 2001).

Linear equations governing the evolution of a system can be written of the form given in Eqn. 1.2 where χ is the vector of state variables and B is a linear operator. Non-normality is a property of the operator B such that it does not commute with its adjoint, i.e. $BB^T \neq B^TB$ (Schmid and Henningson, 2001). Non-normal systems have non-orthogonal eigenvectors and can exhibit transient growth (i.e. finite time growth) even when the eigenvalues indicate asymptotic stability. Consider Fig. 1.4 which shows two eigenvectors of a non-normal system at different instances of time t_1 and t_2. A linearly stable system with all its eigenvalues having a negative real part indicates that the evolution of the system projected along the eigenvectors will decay with time. The rate of decay of the eigenvectors will be dictated by the real part of the respective eigenvalues. Figure 1.4 (a) shows the resultant of the eigenvectors e_1 and e_2 at time t_1 as R. At a later instant in time t_2, both the eigenvectors e_1 and e_2 have decayed in magnitude to

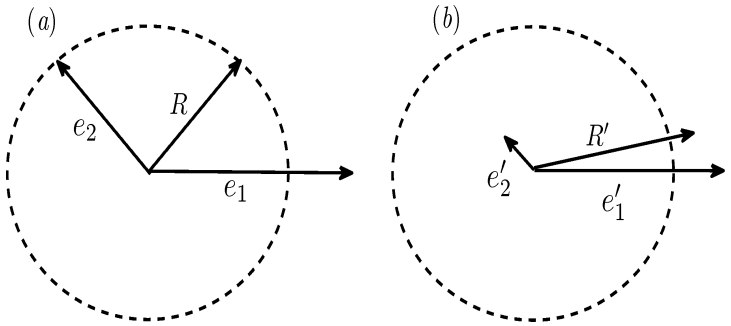

Figure 1.4: Transient growth in a non-normal system. Non-orthogonal eigenvectors e_1 and e_2 are given at (a) time $t = t_1$ and (b) $t = t_2 > t_1$. The eigenvectors decay with time while the resultant R displays transient growth.

vectors e_1' and e_2' as shown in Fig. 1.4 (b). However, the resultant given by R' has grown in magnitude. This growth is transient and eventually the resultant vector also decays along with the eigenvectors. Transient growth due to non-normality can be quantified with tools such as pseudospectra of the linear operator, pseudospectral abscissa and Kreiss constant of the linear operator B (Trefethen and Embree, 2005). Maximum transient growth can be obtained by perturbing the system with the optimal initial condition. The optimal initial condition can be obtained for a given system configuration by the singular value decomposition (SVD) of the linear operator (Farrell and Ioannou, 1996; Schmid and Henningson, 2001) or by the method of adjoint optimization (Bottaro *et al.*, 2003; Mariappan and Sujith, 2010*a*; Juniper, 2010).

Similar to hydrodynamic stability theory, classical stability analysis of thermoacoustic systems listed in Section 1.2, also assume a modal approach. However, the assumption of normal modes holds good for acoustic fields in resonators only when the acoustic boundary conditions specify a fully open or closed end and in the absence of oscillatory heat addition (e.g. combustion). Recently, Nicoud *et al.* (2007) have shown that the presence of a source of unsteady heat release and non-trivial boundary conditions can make the eigenmodes non-orthogonal. Balasubramanian and Sujith (2008*a*) have demonstrated that the linear operator governing thermoacoustic systems is non-normal. Therefore, a modal approach to stability analysis can be misleading in thermoacoustic systems. Both hydrodynamic and thermoacoustic systems are governed by nonlinear equations. In hydrodynamic systems the nonlinear terms in the governing differential equations conserve kinetic energy (Chu and Kovasznay, 1958). The conservative nature of the nonlinear terms makes a linear mechanism of growth to be a necessary condition

for the occurrence of sub-critical transition to instability (Reddy and Henningson, 1993; Krechetnikov and Marsden, 2009). In thermoacoustic systems, the nonlinear terms in the governing equations do not conserve energy. The non-conservative nature of the nonlinear terms relaxes the need for a linear mechanism of growth to be necessary for sub-critical transition to instability. Therefore, sub-critical transition to instability in thermoacoustic systems can occur even when transient growth due to non-normality is not significant.

Balasubramanian and Sujith (2008*a*) investigated thermoacoustic instability in a ducted diffusion flame to characterize its non-normal and nonlinear behavior. A Burke-Schumann type geometry was chosen for the ducted diffusion flame and solved in a time-domain model using the Galerkin technique. The resulting system was found to be non-normal and transient growth in the energy of fluctuations was observed. This transient growth of energy was found to be larger for system configurations when the Peclet number Pe was larger, i.e. the evolution was dominated by the convective terms in the equation. Also, sub-critical transition to instability was exhibited by this system from a small but finite amplitude initial condition. Balasubramanian and Sujith (2008*c*) also investigated transient growth in a simple model of a horizontal Rijke tube. They calculated the dependence of transient growth on the time lag and heater location. Pseudospectra of the linear operator was used to investigate pseudoresonance in the Rijke tube system. The phase between heat release rate fluctuations and the acoustic pressure was shown to evolve to 90° in the absence of damping in the system. When the phase is 90°, unsteady heat release rate does not affect the acoustic pressure evolution and the system has reached a self-sustained limit cycle oscillation. The evolution of an initially decaying system was investigated. It was observed that a shift in the dominant frequency occurred during the evolution during to nonlinear coupling between the different frequencies.

Culick (1997) performed an ordering analysis and observed that the effect of coupling between the different Galerkin modes in the linear regime is of an order smaller than necessary, to affect the eigenvalues. Based on the above result, they argued that the neglecting the coupling between different modes in the linear regime was justified. Annaswamy *et al.* (1997) advocated the importance of including the effects of

linear coupling in the investigation of thermoacoustic instabilities. They showed that the inclusion of linear coupling affects both the energy amplification and attenuation characteristics of the unsteady heat release rate. They demonstrated the consequences of assuming modal coupling in the design of a model based active controller. Kedia *et al.* (2008) investigated the consequences of ignoring linear coupling in stability analysis of thermoacoustic models. Using tools such as pseudospectra and Henrici index, they analyzed transient growth in thermoacoustic systems. They observed that when linear coupling is ignored, there is only a negligible change in the eigenfrequency of the system. However, the exclusion of linear coupling terms can alter the transient growth observed significantly. Therefore, it must be ensured that the transient behavior of the system does not change significantly due to the inclusion of linear coupling terms. Nagaraja *et al.* (2009) discussed the importance of using singular values to characterize energy growth during combustion instabilities. They argued that eigenvalues describe the asymptotic state of the system and that quantification of the transient behavior of the system can be obtained by singular value decomposition. The obtained optimal initial conditions for a simple model of a Rijke tube. They derived conditions for no energy growth and also performed a parametric analysis of the effect of system parameters on transient growth.

Tulsyan *et al.* (2009) investigated non-normal effects in a thermoacoustic system with vortex shedding. Pseudospectra was used to analyze the non-normal behavior of the system. They also showed that the vortex-based combustor reached different limit cycles for different initial conditions to the system. Mariappan and Sujith (2010*b*) performed a non-modal stability analysis of thermoacoustic instability in a solid rocket motor with homogenous propellant. Transient growth due to the non-normal nature of the system is shown to play a role in sub-critical transition to instability. Kulkarni *et al.* (2011) investigated the failure of traditional controllers based on classical linear stability. They designed a linear controller which can control the transient growth observed in non-normal system, thereby preventing transition to instability due to transient growth.

Selimefendigil *et al.* (2011) performed non-modal stability analysis for an electrically heated horizontal Rijke tube system. The response of the heater to acoustic velocity perturbations was obtained using a linear correlation based system identification

method. The obtained correlation was used to construct a low order model of the Rijke tube. Maximum growth factor and transient growth obtained from the low order model based on King's law (King, 1914) is compared with the identified model obtained from CFD. Wieczorek *et al.* (2010) investigated the non-normal nature of thermoacoustic interaction, including the mean flow effects. A one-dimensional analysis of a duct with a flame and a choked isentropic nozzle following it was considered. Eigenmodes of the system were determined using linearized Euler equations. Transient amplification due to non-normality in the system was calculated using the obtained eigenmodes. Weiczorek (2010) defined a measure for the maximum amplification of energy in this system which include the mean flow effects. The energy of fluctuations should include the contributions from the convected vorticity and entropy modes in addition to the acoustic energy.

Waugh *et al.* (2010) investigated the effect of additive stochastic noise to sub-critical bifurcation occurring in a Rijke tube model. They obtained stochastic bifurcation plots which indicate probability of the system being triggered to instability for a linearly stable configuration. Increasing amplitudes of noise in the system was observed to increase the range of the bistable region. Waugh *et al.* (2011) compared bypass transition in hydrodynamic stability to the triggering instability observed in thermoacoustic systems. They observed that initial perturbations with large amplitudes at low frequencies are more effective at triggering a system to instability. Juniper (2010) used the method of adjoint optimization to obtain the most dangerous initial condition which can trigger a Rijke tube system to instability. He draws an analogy between sub-critical transition to instability due to transient growth, which is observed in thermoacoustic systems to 'bypass transition' observed during transition to turbulence in fluid flows. Mangesius and Polifke (2010) developed a state-space model based on a frequency-domain network model of a thermoacoustic system. This model allows efficient computation of the pseudospectrum of the evolution operator and it is easily adapted to systems with complex topology.

In all the above mentioned applications of non-modal stability analysis in thermoacoustic systems, a measure or norm of the system much be chosen to quantify transient growth due to non-normality. The choice of an appropriate norm for the energy due to

fluctuations is discussed in detail in the next section.

1.5 Quantification of disturbance energy

The energy due to fluctuations in a system forms a measure or norm to characterize the transient growth in the system. Disturbance energy is the energy associated with fluctuations super-imposed over a base flow. It should account for contributions from all the constituent phenomena in the system. Kinetic energy was chosen as the natural measure to describe transient growth due to non-normality for incompressible fluid flows (Schmid and Henningson, 2001). However, there has been no such consensus on the appropriate expression for disturbance energy for compressible reacting flows.

Chu (1964) derived the energy of a small disturbance in a viscous compressible flow which included the energy due to entropy fluctuations in addition to the energy due to pressure and velocity fluctuations. Morfey (1971) derived a measure for the energy due to small fluctuations with an irrotational base flow. Myers (1991) relaxed the restrictive assumptions regarding the nature of the base flow and perturbation amplitude and derived a measure for disturbance energy in a general steady flow. In addition to the classical acoustic energy, this measure accommodates the energy associated with fluctuations in vorticity and entropy. In compressible flows, the spatial average of the rate of pressure related work or compression work does not contribute to the evolution of energy density (Mack, 1969; Chagelishvili *et al.*, 1994; Farrell and Ioannou, 2000). Myers's measure for disturbance energy can further be modified to account for this conservative nature of compression work (Bakas, 2009).

Nicoud and Poinsot (2005) argued that the Rayleigh criterion gives an incomplete description of the significant sources of fluctuating energy in a flow with combustion. They advocate that in thermoacoustic system with flames, entropy waves play a role. A new stability criterion is obtained which require that the temperature fluctuations and heat release rate fluctuations are in phase to cause instability. Giaque *et al.* (2006) extended the expression for disturbance energy from Myers to incorporate species and heat release terms in the energy of fluctuations. The energy measure chosen to study

the non-normal nature of thermoacoustic instability in solid rocket motors included the energy associated with the entropy fluctuations within the propellant in addition to the expression for the classical acoustic energy (Mariappan and Sujith, 2010*b*) following Chu (1964). Evidently, it's critical to define the energy in a disturbance depending on the system under consideration. The source of unsteady heat release rate can be an electrical heater, a premixed flame, a diffusion flame, etc. in a thermoacoustic system. A brief overview of the thermoacoustic systems analyzed in the present thesis is elaborated in the next section.

1.6 Modelling the unsteady heat release rate

In a thermoacoustic system, the source of unsteady heat release rate can add energy to the acoustic oscillations if the Rayleigh criterion is satisfied. This addition of energy to the acoustic oscillations is termed as acoustic driving. Therefore, modelling the source of unsteady heat release rate oscillations plays an important part in obtaining an accurate model for the thermoacoustic system. The prevalent approach to model the source of unsteady heat release rate is in terms of its response function to acoustic velocity fluctuations. Transfer functions are obtained for the linear response (Schuller *et al.*, 2003) and amplitude dependent transfer functions/describing functions (Dowling, 1997)) are obtained to characterize the nonlinear response. Many investigations of ducted premixed flames which were focused on describing the heat release rate characteristics in terms of a describing function in the frequency domain are discussed in Section 1.2.

The obtained response function is then used as the source in the acoustic energy equation to evaluate the stability of the thermoacoustic system. In this frequency domain analysis, the transient response of the unsteady heat release rate to acoustic velocity perturbations is not captured. However, the inclusion of the transient response of unsteady heat release rate can change the prediction of system dynamics significantly. Therefore, the model of a thermoacoustic system must be capable of capturing transient effects. Time-domain models for the unsteady heat release rate are capable of capturing transient effects and are used in the present thesis. Time domain approaches model the heat release rate as delayed responses to acoustic perturbations or using a partial

differential equation to describe the evolution of the source of unsteady heat release rate.

1.6.1 Delay model for the unsteady heat release rate

Delay is defined as the time elapsed between a change in the input to the system and its initial response. True delays arise in a system when the input is introduced (transportation lag) or when the output is measured (measurement lag) at a distance away from the system. Apparent delays are caused due to higher-order dynamics whose effects appear as slow or delayed response of the system to inputs (Astrom and Hagglund, 1995). An example is the transfer lag which is present when two or more systems are connected in series (Coughanowr, 1991). Lag in a system is characteristic of the system and is different from its inertia (Tangirala, 2011). In order to completely define a system with delay, an initial time history is also required in addition to an initial condition. The use of a delay model in thermoacoustic systems was pioneered by Crocco and Cheng (1956). They used a time lag model to study combustion instability in a liquid propellant rocket motor. Lieuwen (1998) performed a characteristic time analysis to consider the evolution of a fluctuation in pressure within a combustor. Schuermans *et al.* (2004) included transport lag to rewrite the fuel mass flow fluctuations just upstream of the flame as a function of fuel mass flow fluctuations at the fuel injector at a previous time instant.

Heckl (1990) used a modified form of King's Law (King, 1914) to arrive at a correlation between the heat release rate and acoustic velocity fluctuation in a horizontal Rijke tube. This correlation relates the unsteady heat release rate at time t to the acoustic velocity fluctuations at the heater location at time $(t-\tau)$. Thus, the correlation contains an explicit time delay which accounts for thermal inertia in the system. The delay was determined using the formula given by Lighthill (1954). Heckl's correlation was used to construct a model for a horizontal Rijke tube by Balasubramanian and Sujith (2008*c*). They investigated the non-normal nature of thermoacoustic interaction in a horizontal Rijke tube. Nonlinear effects observed in experiments such as sub-critical transition to instability and dominant mode change during evolution were displayed by this model Balasubramanian and Sujith (2008*c*).

However, a systematic investigation into the stability of thermoacoustic systems for different configurations is necessary. Determining the stability of the system for different configurations by evolving the system from different initial conditions is expensive. The alternate method of numerical continuation (Allgower and Georg, 2003) can be employed to obtain the bifurcation plots of a thermoacoustic system efficiently. The method of numerical continuation has the advantage that once a stationary or periodic solution has been computed, the dependence of the solution on the variation of a parameter is obtained efficiently as compared with the directly obtaining the bifurcation plots from multiple time evolutions.

Sub-critical transition to instability which are observed in experiments, are demonstrated to occur in the model of a thermoacoustic system. Using this model, we can determine the regions of stability and the asymptotic state of the system at different configurations. As the evolution equations for the Rijke tube model contain an explicit delay term, numerical continuation methods employed for this model must be capable of handling delay differential equations (Engelborghs and Roose, 1999).

1.6.2 Modelling the evolution of unsteady heat release rate

Time domain models for thermoacoustic systems can include an evolution equation for the heat release rate dynamics in addition to the acoustic equations for momentum and energy. Modelling the evolution of heat release rate fluctuations with a separate evolution equation for the flame front has been employed in the study of ducted premixed flame. Annaswamy *et al.* (1997) derived a lumped parameter model for the ducted premixed flame in terms of an evolution equation for the net unsteady heat release rate. This model includes a single equation for the evolution of heat release rate in addition to the evolution of acoustic variables and is valid in the linear regime. As the initial value of the unsteady heat release rate can be supplied as part of the initial condition, this model can accommodate a non-zero value for the unsteady heat release rate at time $t = 0$. This implies that the model is capable of tracking the evolution of an initially perturbed flame shape. However, the initial condition for the unsteady heat release rate $\dot{q}'_0$ at time $t = 0$ can be obtained from a number of different perturbed flame fronts.

This model cannot distinguish between the different perturbed flame fronts which can subsequently have different evolutions.

Dowling (1999) used the front-tracking equation to model the evolution of a premixed flame in the investigation of the thermoacoustic instability in a ducted premixed flame. The equations for the acoustic field are evolved together with the front tracking equation for the flame. The use of an evolution equation to describe the premixed flame provides for specification of the flame shape and also includes the transient effects. Therefore in the present investigation, Dowling's approach is adopted to model a ducted premixed flame.

Given a periodic solution, the behavior of the system for the variation of system parameters can be obtained efficiently using the method of numerical continuation. The next section introduces the method of numerical continuation along with a brief survey of previous literature on tools from dynamical systems' theory which can be used to identify different asymptotic states of a system.

1.7 Determination of the asymptotic state

Numerical continuation (Allgower and Georg, 2003; Ananthkrishnan *et al.*, 2005) is an alternate approach to obtain bifurcation diagram from a numerical model. This method aims to solve a set of parameterized nonlinear equations iteratively, given an initial guess for the state of the system. Solutions which satisfy the set of equations and which are additionally connected to a given state of the system are tracked for a given smooth variation of one or more parameters. Bifurcations are identified by including multiple test functions which change sign at the critical value of the parameter. This method has the advantage that once a stationary or periodic solution has been computed, the dependence of the solution on the variation of a parameter is obtained very efficiently as compared with the other methods described earlier. It can also be used to compute unstable limit cycles.

Jahnke and Culick (1994) used the continuation method to obtain the amplitudes of longitudinal acoustic modes in a combustion chamber. They obtained bifurcation plots

for different number of normal modes of the combustion chamber. Pitchfork bifurcations of the limit cycles leading to new branches of limit cycles and torus bifurcation leading to quasiperiodic motions were observed in this analysis. Burnley (1996) investigated the stability of a combustion chamber using numerical continuation and investigated the effect of combustion noise on the stability of the system. Perturbation analyses were used to investigate the effects of the nonlinear terms in determining the limit cycle behavior. Reduced order models for the combustion chambers have been solved by the framework of expanding the pressure and velocity fields in terms of modal or basis functions. Ananthkrishnan *et al.* (2005), examined the issue of modal truncation and established the number of modes required to accurately capture the dynamics of the system.

In numerical continuation, the different types of equations encountered in models of physical systems require special attention during the analysis stage. As an example, delay differential equation must be analyzed using numerical continuation methods that are capable of handling time delay systems. During bifurcations, evolutions of dynamical systems can reach asymptotic states other than a steady state or a limit cycle. Some of the other asymptotic states that the system could evolve to are: quasiperiodic, period-2, period-4 and chaotic states.

Culick (1976) derived a model for the nonlinear behavior of acoustic waves in a combustion chamber which included second-order nonlinearities in gas dynamics. Yang *et al.* (1990) extended this model to include third order nonlinearities in acoustic wave propagation. This model for thermoacoustic instability was used by Lei and Turan (2009) who investigated the asymptotic states obtained from a one-mode analysis of the model. Lei and Turan (2009) identified the occurrence of period-2, period-3 and chaotic oscillations in this system using Poincare sections. Different asymptotic states were also observed in experiments. Sterling and Zukowski (1991) conducted experiments in a laboratory combustor for the variation of equivalence ratio and mean flow rate. They obtained asymptotic states in which the amplitude varied from cycle to cycle. However, they do not identify the nature of the asymptotic state. Fichera *et al.* (2001) performed experiments in a methane-fuelled laboratory combustor. They calculated Lyapunov exponents and embedding dimensions to prove the existence of chaos.

Kabiraj *et al.* (2010) gradually varied the location of the flame in a ducted premixed flame system and observed different asymptotic states. Quasiperiodic, period-2, mode-locked and chaotic oscillations were obtained for different locations of the flame along the duct. Kabiraj *et al.* (2010) identified the sequence of different asymptotic states occurring for the variation of the flame location to identify the Ruelle-Taken's route to chaos in a ducted premixed flame system.

Two significant issues arise due to the presence of these different asymptotic states. The first issue is that, the frequency content of the oscillations during the different asymptotic states can vary significantly from well defined harmonics to a spectrum with broadband frequency peaks. Therefore special care must be taken to ensure that the frequencies encountered during these asymptotic states does not interfere with resonant frequencies of associated structures in the thermoacoustic system. Secondly, instabilities with the above mentioned asymptotic states impose repetitive uneven stresses and thermal loads upon the structure. These uneven loads can significantly lower the operating life of the system and can even make control of instabilities difficult (Suresh, 1998). Considering the above mentioned reasons, it is important to characterize the different asymptotic states encountered during instabilities in thermoacoustic systems. Tools such as frequency analysis using fast Fourier transform (FFT), phase portraits, Poincare sections and Lyapunov exponents (Strogatz, 2000) can be used to differentiate between the different states and to characterize them. These tools from dynamical systems' theory are introduced in detail in Chapter 2.

The next section lists the outstanding issues raised in the previous sections, states the objective of the present thesis and gives an overview of the different chapters of the thesis.

1.8 Objectives and overview of the thesis

The primary objective of the present thesis is to use tools from the dynamical systems' theory to characterize the linear and nonlinear behavior of thermoacoustic systems. In order to include the effect of transients in the analysis, time domain approaches to mod-

elling the heat release rate fluctuations are employed. Two models for thermoacoustic systems are chosen. One where the unsteady heat release rate is modelled in terms of a time delay model and the other where an evolution equation is written to describe the heat release rate dynamics. A horizontal Rijke tube model is chosen as an example of a system with explicit delay. A ducted premixed flame is chosen as an example of a system with an evolution equation for the heat release rate.

As discussed in Section 1.4, the presence of a source of unsteady heat release rate causes thermoacoustic systems to be non-normal. It has previously been observed that evolutions of a horizontal Rijke tube Balasubramanian and Sujith (2008*c*), a ducted diffusion flame (Balasubramanian and Sujith, 2008*a*), a vortex-based combustor (Tulsyan *et al.*, 2009) and solid rocket motor (Mariappan and Sujith, 2010*b*) are governed by non-normal linear operators. However, many practical thermoacoustic systems contain a premixed flame as the source of unsteady heat release rate. Therefore, it is important to examine the effects of non-normality such as transient growth in ducted premixed flames and to determine the extent to which these effects are significant in determining the stability of the system. The dependence of transient growth due to non-normality on different system parameters must be characterized.

In the case of a Rijke tube model, as defined in Section 1.6.1 the heat release rate fluctuations are re-written in terms of acoustic velocity fluctuations. Therefore, the state variables consist of only the acoustic variables. Acoustic energy can therefore be used to quantify transient growth in the Rijke tube system. However as defined in Section 1.6.2 the model of a ducted premixed flame consists of a premixed flame front which is discretised into a number of flame elements. As the unsteady heat addition from the premixed flame acts as a volumetric source, the flame front is modelled as a distribution of acoustic monopole sources. The state variables of the resulting set of equations for the ducted premixed flame system consist of variables corresponding to the strength of monopoles along the flame front in addition to the acoustic variables. The measure chosen to quantify transient growth in the ducted premixed flame system must include contributions from the heat release rate fluctuations in addition to the acoustic energy. In the present thesis, the flame front is modelled as a distribution of monopole sources. The energy due to monopole sources is added to the acoustic energy, as shown in Section

4.5.2 to obtain the appropriate measure of disturbance energy for a ducted premixed flame.

Transition to instability can occur when the linear system becomes unstable or when a linearly stable system is triggered to instability. Sub-critical transition to instability or triggering has been traditionally thought to occur due to a finite amplitude perturbation to the system. A large amplitude initial condition can make the nonlinear effects to become significant causing the system to become unstable. However, triggering can occur from a small but finite amplitude initial condition (Zinn and Lieuwen, 2006). The role of transient growth in the occurrence of sub-critical transition from a small but finite amplitude initial condition is emphasized by Mariappan *et al.* (2010). They perform a non-modal stability analysis of a Rijke tube model and show that smaller amplitudes of the optimal initial perturbations are sufficient to cause instability than a purely acoustic initial perturbation. Thermoacoustic interaction in a ducted premixed flame must also be investigated to determine the role of non-normality in triggering a system to instability from a small amplitude initial condition.

Safe ranges of operation in gas turbines and rocket motors must be identified in order to avoid instabilities. Bifurcation plots of the system must be obtained to identify the safe ranges of operation. Obtaining bifurcation plots from time evolutions of the system is time consuming and expensive. Therefore the alternate method of numerical continuation is adopted to systematically obtain stability boundaries and bifurcation plots. The feasibility of numerical continuation method to obtain the bifurcation plots in thermoacoustic systems is demonstrated in this thesis. The method of numerical continuation is applied to two models of thermoacoustic systems; a model for a horizontal Rijke tube and a model for a ducted premixed flame. Thermoacoustic systems can also evolve to asymptotic states other than a limit cycle. The nature of the asymptotic state of evolutions in a Rijke tube and ducted premixed flame are investigated using tools from dynamical systems' theory.

The overview of the thesis is as follows. Chapter 2 explains the background on tools from dynamical systems' theory. Pseudospectra and Kreiss constant can be used to identify bounds for transient growth in a non-normal system. The method of singular value decomposition is applied to isolate the most dangerous initial condition or the

optimal initial condition. Identification of primary and secondary bifurcations en route to chaos in a dynamical system are explained. The method of numerical continuation as applied to a system of ordinary and delay differential equations is detailed. Methods of analysis such as phase plane method, Lyapunov exponent and Poincare maps are introduced.

Chapter 3 investigates the nonlinear behavior of a horizontal Rijke tube. The method of numerical continuation is applied to a Rijke tube model described by delay differential equations. Linear stability bounds and bifurcation plots are obtained. Analytical methods such as linear stability analysis, the method of multiple scales and the method of harmonic balance are used to estimate critical points of the bifurcation plot. Comparison of numerical results with analytical estimates and experimental results are performed.

The non-normal nature of thermoacoustic interaction in a ducted premixed flame is analyzed in Chapter 4. Transient growth due to non-normality is quantified with an appropriate measure of the energy due to fluctuations. The role of transient growth in the occurrence of triggering from a small but finite amplitude initial condition is explored. The equation describing the evolution of the premixed flame front, together with the acoustic equations for momentum and energy reduces the thermoacoustic system to a set of ordinary differential equations. The method of numerical continuation is employed to these ordinary differential equations to obtain bifurcation plots for the system.

In both the Chapters 3 and 4, tools from dynamical systems' theory such as phase plane analysis, Lyapunov exponents and Poincare maps are employed to ascertain the asymptotic nature of system evolutions. Conclusions of the investigations and scope of future work are listed in Chapter 5.

CHAPTER 2

BACKGROUND ON TOOLS FROM DYNAMICAL SYSTEMS' THEORY

Time evolutions of a system give information about the stability of the system and the resulting asymptotic state. However, this information is specific to the chosen system parameters and the applied initial condition. Thus, individually obtaining evolutions in time to characterize the behavior of the system for a range of parameter values and initial conditions is expensive. A systematic and efficient investigation of both the linear (Trefethen and Embree, 2005) and nonlinear (Burnley, 1996) behavior of the system can be performed using tools from dynamical systems' theory. Dynamical systems approach aims to model the time evolving dynamics of physical systems. In many applications, the evolution of the system is independent of time and the system is modeled as an autonomous dynamical system. These models in general consist of a set of parameterized nonlinear partial differential equations. These nonlinear partial differential equations can be converted into a set of ordinary differential equations by the method of modal expansion (Zinn and Lores, 1971) or by discretising the system in space (Schmid and Henningson, 2001). The stability of the system and the nature of the asymptotic state for different configurations can be obtained by investigating the set of ordinary differential equations.

If χ is the vector of state variables and μ is the vector of system parameters, then the set of nonlinear ordinary differential equations can be written of the form

$$\frac{d\chi}{dt} = F(\chi, \mu)\,, \tag{2.1}$$

where F is the nonlinear matrix which is a function of both χ and μ. When the nonlinear effects in the system are neglected, the set of equations governing the linear evolution of the system can be written as

$$\frac{d\chi}{dt} = F_{Linear}(\mu)\chi\,. \tag{2.2}$$

Here, the linear matrix F_{Linear} is purely a function of the system parameters and governs the evolution of the system only to small perturbations as enforced by the assumption of linearity. In the present thesis, the operator which governs the linear evolution of the system is denoted as B such that $F_{Linear} = B$ as given in Eqn. 1.2 of Chapter 1. Information on the behavior of the system can now be systematically obtained by investigating the nature of the linear operator B and the nonlinear evolution operator F.

2.1 Linear analysis

The asymptotic stability of a system can be determined using classical linear stability analysis. In classical linear stability analysis, the eigenvalues λ_i of the linear operator B are obtained. If the real part of all λ_i are negative, it indicates that any perturbation to the system will decay asymptotically and the system returns to the unperturbed state. If an eigenvalue λ_i has a positive real part z, then any perturbation given to the system will grow exponentially as e^z. In this case, the system does not return to its unperturbed state and is linearly unstable. Eigenvalues thus indicate the asymptotic stability of the system, i.e. the stability of the system as $t \rightarrow \infty$. However, non-normal systems can exhibit transient growth even in a linearly stable system (Schmid and Henningson, 2001). If this transient growth is large enough to cause nonlinear terms to become significant, the system could become unstable even when all the eigenvalues indicate stability. Thus, classical linear stability analysis is insufficient to characterize the behavior of non-normal systems.

The main reason for the classical linear stability analysis to fail is the assumption that the eigenvectors e_i associated with the eigenvalues λ_i of the system are orthogonal (normal) to each other. Two consequences of non-normal eigenvectors are explored in this paragraph. The first effect is the transient growth possible in the magnitude of resultant even when all the eigenvectors e_i are decaying as shown in Fig. 1.4. Secondly, when a normal system is forced with an input frequency ω, response of the system occurs. The amount of this resonant amplification is equal to the inverse of the distance between ω and the nearest eigenvalue of the system in the complex plane. However, in a non-normal system resonant amplification at a frequency ω can be orders of magnitude

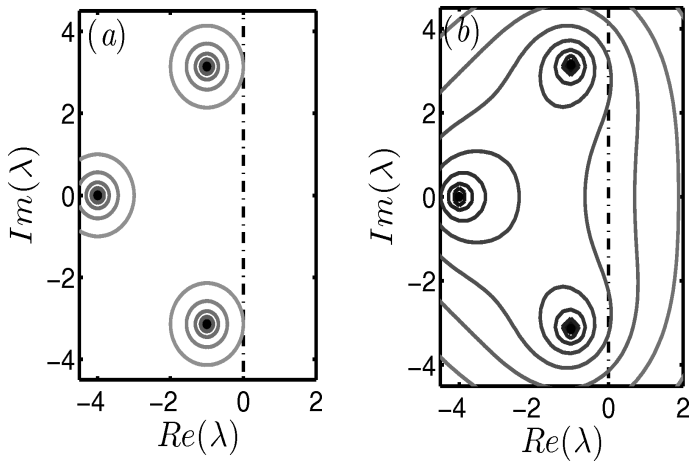

Figure 2.1: Pseudospectra for (a) normal system given by B_{normal} and (b) non-normal system given by $B_{non-normal}$. Different contours indicate different levels of perturbation ϵ.

larger than the inverse of the distance between ω and the nearest eigenvalue (Trefethen *et al.*, 1993). This implies that resonances in non-normal systems are not determined by eigenvalues alone (Trefethen and Embree, 2005). Therefore, eigenvalues and classical linear stability analysis are robust estimators of asymptotic behavior of linear systems only if the associated eigenvectors are normal to each other.

Resonant amplification of forcing occurs at the frequencies ω which are close to frequencies corresponding to the eigenvalues in normal systems. Thus the eigenvalues or spectra λ_i describe the frequencies at which a system governed by the linear operator B gives maximal resonant response. As mentioned in the previous paragraph, large amplitude resonant amplification can occur even when the forcing frequency is far away from the eigenvalues in non-normal systems. This phenomenon is called pseudoresonance (Kato, 2005). Pseudospectra give information on the resonant response of a non-normal system. The ϵ-pseudospectrum is defined as the eigenvalues of some perturbed matrix, $B + T$. where the perturbed matrix T satisfies the constraint $\|T\| < \epsilon$ (Trefethen *et al.*, 1993). Contours of the ϵ-pseudospectrum for different values of perturbation ϵ together are termed pseudospectra.

Pseudospectra of a normal and non-normal system are shown in Fig. 2.1 which are obtained using the software 'eigtool' (Wright, 2002). The matrices used in the two

examples are

$$B_{normal} = \begin{pmatrix} -4 & 0 & 0 \\ 0 & -1+i\pi & 0 \\ 0 & 0 & -1-i\pi \end{pmatrix}, \tag{2.3}$$

$$B_{non-normal} = \begin{pmatrix} -4 & 0 & 0 \\ 200 & -1+i\pi & 0 \\ 180 & 0 & -1-i\pi \end{pmatrix}. \tag{2.4}$$

It can be seen from Fig. 2.1 (a) that random perturbations of magnitude ϵ to the normal operator results in concentric circles around each eigenvalue. In contrast, the pseudospectra of the non-normal operator in Fig. 2.1 (b) are highly skewed, even with the eigenvalues being identical to normal system shown in Fig. 2.1 (a). Skewed contours in the pseudospectra are produced due to the large sensitivity of the eigenvalues to perturbations in B. The matrix composed of the eigenvectors e_i as its columns is defined as EV. The sensitivity of the eigenvalues indicate that the condition number of EV is large. The matrix EV satisfies the relation

$$\|EV\| \, \|EV^{-1}\| >> 1 \, . \tag{2.5}$$

This relation identifies B as a matrix which is 'far from normal' (Trefethen and Embree, 2005).

When B is far from being normal, the eigenvalues and singular values of B are widely disparate (Moler, 2008). Singular values of B can have large positive values even when all eigenvalues have negative real parts. Singular values give the amount by which an input state χ_n to the system governed by B is amplified to obtain the output state χ_{n+1}. The action of singular values on perturbations to a linear system is explained in detail in the next section. The input perturbations which are aligned along the directions of the first right singular vector V_1 undergo maximum amplification. Thus, the amplification of a disturbance in linear non-normal systems depends on the distribution of perturbation among the different state variables. Therefore in linear non-

normal systems, optimal distributions of perturbation in the different state variables can be identified. Optimal initial condition for a given system governed by B can be obtained using a singular value decomposition of B (Trefethen *et al.*, 1993) or using the variational technique of adjoint optimization (Bottaro *et al.*, 2003).

In the next section, we introduce tools such as singular value decomposition (SVD), Pseudospectra, Pseudospectral abscissa and the Kriess constant (Kreiss, 1971) which are used to characterize the behavior of non-normal systems, to quantify their transient growth and to identify the optimal initial condition.

2.2 Tools used in non-modal linear stability analysis

2.2.1 Singular value decomposition

Singular values of matrices play an important role when the matrix is used to transform an input between two vector spaces (Moler, 2008). Singular values Σ and singular vectors U and V for a real matrix B can be defined as

$$\begin{aligned} BV &= U\Sigma\,, \\ B^T U &= V\Sigma^T\,. \end{aligned} \tag{2.6}$$

Here, both U and V are unitary matrices whose columns are the normalized left and right singular vectors of B respectively. Σ contains the singular values along its diagonal. The above relation can be re-written as

$$B = U\Sigma V^T\,. \tag{2.7}$$

The expression given in Eqn. 2.7 can be substituted in the evolution equation for a linear system Eqn. 1.2 to give

$$\frac{d\chi}{dt} = B\chi = U\Sigma V^T\chi\,. \tag{2.8}$$

Thus the action of the matrix B on a state vector χ can be decomposed into three separate operations. If χ is the state vector at a time, then the action of V^T is to obtain

the projection of χ along the right singular vectors of B. The action of Σ on $V^T\chi$ is to scale the components of the projections by the respective singular values. Finally, the action of U is to realign the result of the scaling along the output directions.

In the case of a normal matrix, the eigenvalues and the singular values are closely related (Moler, 2008). Positive eigenvalues with $\lambda_1 > 0$ are also singular values, i.e. $\sigma_i = \lambda_i$ and the corresponding eigenvectors are equal to the singular vectors, i.e. $u_i = v_i = e_i$. In the case of a negative eigenvalue with $\lambda_i < 0$, singular value is the modulus of the eigenvalue such that $\sigma_i = |\lambda_i|$ and one of the singular vectors is the negative of the other, i.e. $u_i = -v_i = e_i$. However in non-normal systems, the eigenvalues and singular values can be widely separated with large positive singular values occurring even when all the eigenvalues have negative real parts. This large singular value is indicative of the large transient growth observed in non-normal systems (Schmid and Henningson, 2001). The normal convention is to stack the singular values σ of the matrix Σ in descending order. In this scenario, the square of the first singular value indicates the largest possible amplification in the system. This amplification will occur of the input is aligned along the first right singular vector or the first column of V. This input is therefore the most dangerous initial condition or the optimal initial condition. Thus singular value decomposition can be used to obtain the optimal initial condition V_1 and the resulting transient growth σ_1^2 in the system.

2.2.2 Quantification of transient growth

The matrix B governs the linear evolution of the system as given in Eqn. 1.2. The solution to this equation when the state of the system at time $t = 0$ as $\chi(0)$ is known can be written of the form

$$\chi(t) = e^{Bt}\chi(0)\,, \tag{2.9}$$

where the linear operator B is purely a function of the system parameters (Hirsch *et al.*, 2004). Properties of the linear operator can be used to determine the bounds on the transient growth due to non-normality. Specifically, the nature of $\|e^{Bt}\|$ and its variation with time gives information on the possible transient growth during evolution. This transient growth can be quantified using the largest singular value of B as explained

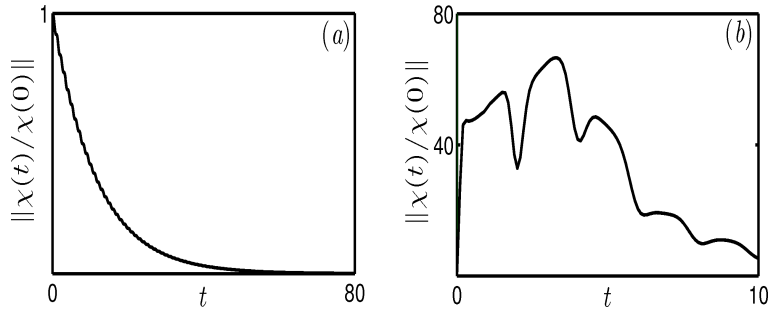

Figure 2.2: Evolution of a non-normal system from (a) an arbitrary initial condition and (b) the optimal initial condition for a given configuration.

in the previous section. Square of the largest singular value σ_1 indicates the transient amplification in the system for the optimal initial condition given by the first column of V. Amplification of energy associated with the perturbations at finite time t can be quantified by the ratio of the square of the norm of the state vector at time t to the square of the norm of the state vector at time $t = 0$ (Schmid and Henningson, 2001).

The evolution of a non-normal system depends on the distribution of perturbation among the different state variables. This is evident from the Fig. 2.2 which shows the evolution of a system from two different initial conditions. In Fig. 2.2 (a), the system displays no transient amplification for evolution from an arbitrary initial condition and is seen to monotonically decay. Evolution from the optimal initial condition shown in Fig. 2.2 (b) displays transient amplification which reaches a maximum before decaying asymptotically. Evolution from the optimal initial condition ensures that the amplification of perturbation is maximized over all possible initial conditions. Further, transient amplification of the perturbation is maximized over time by choosing the maximum value of the evolution. Transient amplification maximized over all possible initial conditions and time is termed as the maximum growth factor G_{max} and the time at which this occurs is termed as t_{max} (Schmid and Henningson, 2001).

$$G_{max} = \max_{t,\chi(0)} s \frac{\|\chi(t)\|^2}{\|\chi(0)\|^2}, . \tag{2.10}$$

Singular value decomposition can be used to identify the optimal initial condition and G_{max} as described in the previous subsection. The square of the largest singular value σ_1^2 gives the value of G_{max}. Transient amplification is a function of the linear

operator B which in turn is a function of the system parameters. Therefore, the value of G_{max} changes with system configuration. Variations of G_{max} and t_{max} with system parameters can be used to identify system configuration when the non-normal effects are pronounced. Both the time taken for maximum growth t_{max} and bounds on the values of G_{max} can be determined from the pseudospectra of B which is given in detail in the next subsection.

2.2.3 Pseudospectra and bounds for transient growth

The ϵ-pseudospectrum for the linear operator B is a set of points in the complex plane which are the eigenvalues of a perturbed matrix $(B + T)$, such that the random perturbation T to the operator satisfies the condition $\|T\| < \epsilon$ (Trefethen and Embree, 2005). Pseudospectra are calculated for different values of perturbation amplitude ϵ and are plotted along with the eigenvalues of B in a single plot to give the pseudospectra of B. A typical log plot of transient growth in the evolution operator $\|e^{tB}\|$ is shown in Fig. 2.3 adapted from Trefethen and Embree (2005). The evolution is seen to increase from its initial value transiently, reach a maximum at finite time and decay asymptotically. Behavior of the evolution at different instances of time can be obtained by different measures from the corresponding pseudospectra. Asymptotic behavior of the evolution is bound by the spectral abscissa of B which is given as

$$\lim_{t\to\infty} t^{-1} \log \|e^{tB}\| = \alpha(B)\,. \tag{2.11}$$

Spectral abscissa is given by the real part of the right most eigenvalue of B in the pseudospectra. This value determines the asymptotic growth rate of the evolution. The initial growth rate of the evolution at time $t = 0$ is given by the numerical abscissa $\omega(B)$ which is defined as

$$\lim_{t=0} t^{-1} \|e^{tB}\| = \omega(B)\,. \tag{2.12}$$

Both the spectral and numerical abscissa describe the evolution of the system at $t \to \infty$ and $t = 0$ respectively. However, it the behavior of the system at finite times that is of interest. Finite time behavior of a non-normal system can be obtained from pseudospectra.

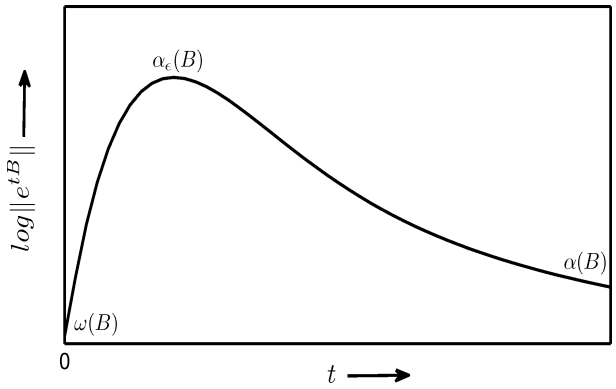

Figure 2.3: Log plot of a typical evolution of the matrix exponential $\|e^{tB}\|$ for a non-normal system with regions of applicability of numerical abscissa $\omega(B)$, pseudospectral abscissa $\alpha_\epsilon(B)$ and spectral abscissa $\alpha(B)$ which bound the evolution at different times.

An ϵ-pseudospectrum is defined as the eigenvalues of a perturbed linear matrix $B + T$ such that $\|T\| < \epsilon$. Pseudospectral abscissa α_ϵ gives the location of the point on the ϵ-pseudospectra which crosses the real axis at the largest value. If the value of α_ϵ is positive, such that $(\alpha_\epsilon(B)/\epsilon) > 1$, then transient growth can occur depending on the initial condition. The ratio of $(\alpha_\epsilon(B)/\epsilon)$ maximized over all ϵ gives the minimum value of transient growth possible. A lower bound on the magnitude of the transient growth can be given in terms of the Kreiss constant $\kappa(B)$ from the Kreiss matrix theorem as given below (Kreiss, 1971):

$$\sup_{t\geq 0} \|e^{tB}\| \geq \sup_{\epsilon>0} \frac{\alpha_\epsilon(B)}{\epsilon} = \kappa(B)\,. \tag{2.13}$$

The upper bound on transient growth $\varphi(B)$ for a matrix of dimension $(2N + P)$ is also given by the Kreiss matrix theorem in terms of $\kappa(B)$ as below:

$$\|e^{tB}\| \leq e(2N + P)\kappa(B) = \varphi(B)\,. \tag{2.14}$$

When the pseudospectral abscissa σ_ϵ is the ϵ-pseudoeigenvalue of the system with the largest real part, the system experiences a transient growth of the order of over a time span $1/\sigma_\epsilon$ (Trefethen and Embree, 2005). Thus, pseudospectra can also give an estimate of the time over which transient growth occurs t_{max}.

As explained in detail in Section 1.4, thermoacoustic systems are non-normal. The above mentioned tools such as pseudospectra, pseudospectral abscissa and Kreiss con-

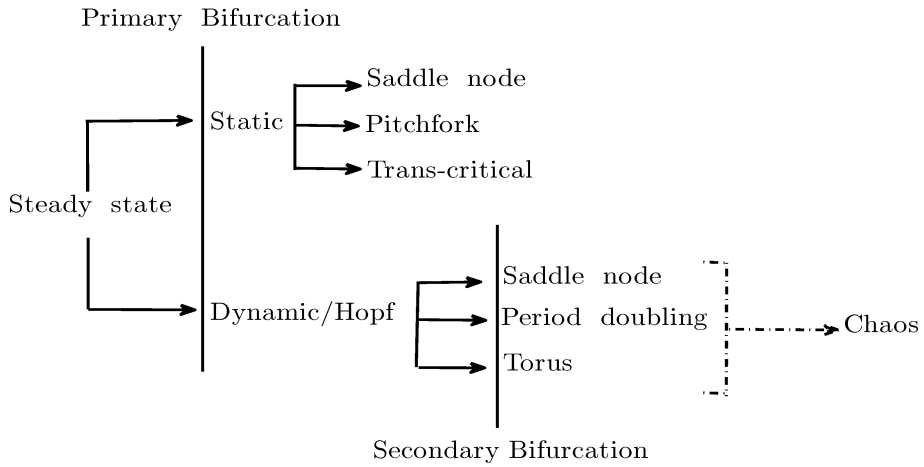

Figure 2.4: Typical route to Chaos.

stant can be used to estimate G_{max} and the time over which transient growth occurs t_{max} in a non-normal system. These tools have been used in quantify the transient growth in a ducted premixed flame system in Chapter 4. However, the equations governing the evolution of thermoacoustic systems are in general nonlinear. Therefore investigation of thermoacoustic instability must include the effects of the nonlinear terms. In the rest of this chapter, nonlinear parametric equations are considered and methods and tools used in their analysis are introduced. Using these methods and tools from dynamical systems' theory, bifurcation plots can be obtained efficiently and the asymptotic nature of evolutions can be classified.

2.3 Nonlinear analysis: a typical route map to chaos

Models of thermoacoustic systems are generally a set of nonlinear partial differential equations. The presence or absence of an explicit time delay in the model converts the partial differential equations into a set of delay differential equations (DDE's) or ordinary differential equations (ODE's) respectively. These parameterized nonlinear set of equations can have multiple solutions for a given system configuration. Small changes in a system parameter can produce qualitative changes in the solution, i.e. bifurcation. A visual representation of all possible solutions along with their stability information plotted as a function of one or more system parameters is a bifurcation plot.

Bifurcations occur as qualitative changes in the nature of the asymptotic state of

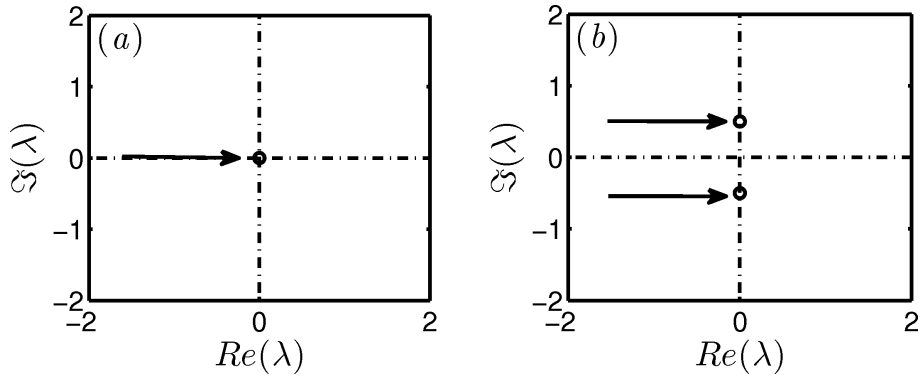

Figure 2.5: Types of primary bifurcation. (a) Static bifurcation (b) Dynamic/Hopf bifurcation.

system for smooth variations of a bifurcation parameter. This section discusses a typical scenario when the asymptotic state of a system progressively varies between a steady state when the system is stable and a chaotic orbit. A typical route map to chaos is shown in Fig. 2.4 which is adapted from Ajjarapu (2006). The simplest solution to a set of nonlinear parameterized equations is obtained when the system reaches a steady state. No oscillations occur in the asymptotic state for the chosen parameter values at the steady state. Primary bifurcation occurs when this steady state loses stability. Loss of stability at the primary bifurcation is identified by the crossing of eigenvalues from the left to the right half of the complex plane. This can occur in one of two ways as shown in Fig. 2.5.

When a real dominant eigenvalue crosses the imaginary axis through the origin as shown in Fig. 2.5 (a), no oscillations are introduced and therefore the bifurcation is called static bifurcation. A new steady state is introduced due to static bifurcation. Static bifurcation can be classified as one of three types - saddle node, pitchfork and trans-critical (Baker and Gollub, 1990). When a pair of complex conjugate eigenvalues cross the imaginary axis, as shown in Fig. 2.5 (b), a frequency component is introduced in the solution. This bifurcation is called a dynamic bifurcation or a Hopf bifurcation and the resulting state after bifurcation is a periodic solution (Baker and Gollub, 1990). If the primary bifurcation is static, it can give rise to new steady states before a dynamic/Hopf bifurcation occurs in the system.

Based on the stability of the periodic solutions, Hopf bifurcation can be classified into a sub-critical or super-critical Hopf bifurcation as shown in Fig. 2.6. If the periodic

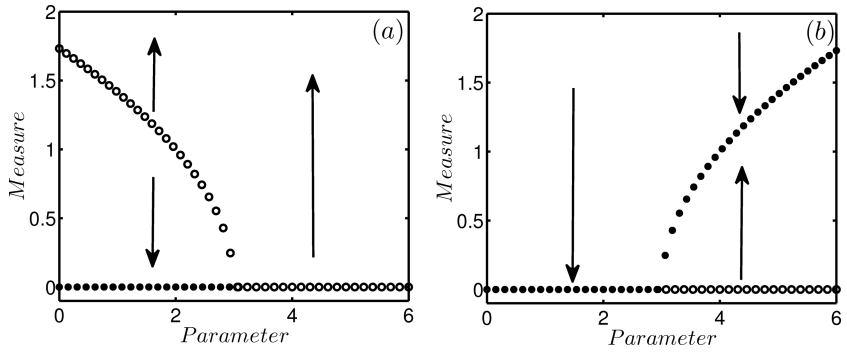

Figure 2.6: Bifurcation behavior of a $Measure$ for the variation of a $Parameter$ near a (a) Sub-critical and (b) Super-critical Hopf bifurcation. • indicate stable solutions and ∘ indicate unstable solutions.

solutions near the loss of static stability are stable, the Hopf bifurcation is super-critical. Sub-critical Hopf bifurcations are obtained when the periodic solutions near the loss of static stability are unstable. These periodic solutions of a system can be strobed at their principal period to obtain the corresponding maps. The matrix which advances the system over one period is called the monodromy matrix (Hillborn, 1994). In Fig. 2.7, the eigenvalues of the monodromy matrix, i.e. Floquet multipliers, are plotted in the complex plane. One pair of complex Floquet multipliers always lie on the unit circle corresponding to the periodicity of the solution.

When the periodic solution obtained after a Hopf bifurcation loses/gains stability, secondary bifurcation occurs. Secondary bifurcation can occur in one of three ways as shown in Fig. 2.7. The unit circle defines the bounds of stability for periodic solutions. When a real Floquet multiplier crosses the unit circle along the positive real axis, a trans-critical or saddle node bifurcation of the periodic solution occurs. At a saddle node bifurcation, the stability of the periodic solution is changed and a fold point is obtained in the bifurcation plot. Therefore, this bifurcation is also called fold bifurcation.

Period doubling bifurcations occur when a real Floquet multiplier crosses the unit circle along the negative real axis, i.e. the Floquet multiplier is -1. As the name implies, sub-harmonic frequencies are introduced in the evolution and the system is seen to alternatively oscillate between two extrema. When a pair of complex Floquet multipliers cross the unit circle, a new frequency is introduced which is incommensurate with the initial periodicity. This causes a torus bifurcation which leads to quasiperiodic behavior of the time evolution.

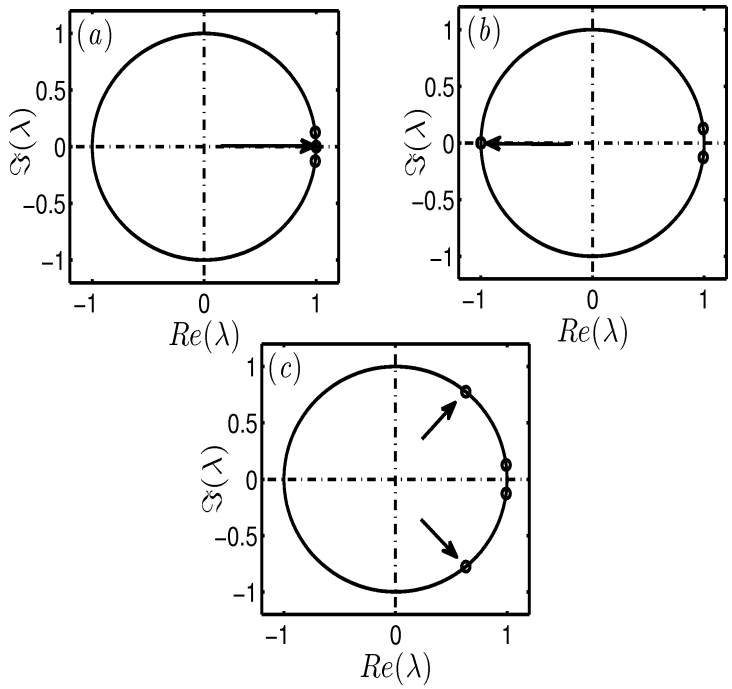

Figure 2.7: Types of secondary bifurcation. (a) Trans-critical/fold bifurcation (b) Period-doubling bifurcation (c) Torus bifurcation.

The route that a system follows to chaos after secondary bifurcation is specific to that particular system. Even in the same system, different routes to chaos such as the period doubling route, Ruelle-Taken's route and intermittency can occur for different system configurations. Thus the route between secondary bifurcation and chaos is not fixed which is indicated by the dashed lines in Fig. 2.4. The approach of obtaining bifurcation plots by systematic variation of parameter and tracking direct time integration is computationally expensive. Alternatively, the numerical continuation method (Allgower and Georg, 2003; Ananthkrishnan *et al.*, 2005) is an approach to obtain bifurcation plot of a model efficiently. The next section introduces some of the terminologies used in the method of numerical continuation.

2.4 Terminologies used in numerical continuation

An efficient method to obtain the bifurcation plot of a system and to locate the primary and secondary bifurcations is the method of numerical continuation (Allgower and Georg, 2003). This method aims to solve a set of parameterized nonlinear equations iteratively, given an initial guess for the state of the system. If χ is the vector of

state variables and μ is the vector of parameters, the deterministic autonomous dynamical system is given as

$$\frac{d\chi}{dt} = F(\chi, \mu)\,, \tag{2.15}$$

where F can be a nonlinear function of the parameters and state. Equation 2.1 defines the evolution of a continuous time system and is called the flow of the system. A discrete time equivalent of the flow is a map which describes the evolution of the system at discrete points in time as

$$\chi_{i+1} = M(\chi_i, \mu)\,. \tag{2.16}$$

Any state (χ_0, μ_0) such that it satisfies the equation of the system is called a solution of a system. The steady state is one of the possible solutions to the dynamical system. The steady state is obtained when $F(\chi_0, \mu_0) = 0$, i.e. by setting the time derivatives to zero in 2.1. A set of solutions $(\chi(s), \mu(s))$ to above mentioned dynamical system, which are connected to a solution (χ_0, μ_0) are collectively called the solution component $\Gamma(\chi_0, \mu_0)$.

The solution component is in general a branched curve and is comprised of regular and singular points. The solution component is an isolated curve near a regular point on it. The Jacobian which is defined as the matrix of all the first order partial derivatives of $F(\chi, \mu)$ has full rank at regular points. The solution component is branched at the singular points which indicates a bifurcation. The Jacobian calculated at these singular points is not full rank. In addition to the equation of flow (Eqn. 2.1), periodic solutions of a system obey the constraint that $\chi(t+T) = \chi(t)$, where T is the principal time period of the oscillation and $\Phi(T)$ is the monodromy matrix (Hillborn, 1994). Eigenvalues of the monodromy matrix are the Floquet multipliers Λ_i which can be used to identify the stability of the periodic solution and to locate secondary bifurcations (Seydel, 1988).

2.5 Numerical continuation

In the method of numerical continuation, solutions which satisfy the set of equations and are additionally connected to a given state of the system are tracked for a given smooth variation of one or more parameters (Allgower and Georg, 2003). Bifurcations

are identified by including multiple test functions which change sign at the critical value of the parameter. This method has the advantage that once a stationary or periodic solution has been computed, the dependence of the solution on the variation of a parameter is obtained efficiently as compared with the direct time integration technique described earlier. It can also be used to compute unstable limit cycles. Continuation methods compute steady states and periodic solutions as a function of a free parameter. Continuation algorithms take as input the set of nonlinear equations and an initial solution to produce a set of points on the solution component (Seydel, 1988). Thus, continuation methods convert the problem of finding solutions for a set of nonlinear parameterized equations to the problem of tracking a curve $\Gamma(\chi_0, \mu_0)$ subject to the constraints given by Eqn. 2.1.

2.5.1 Steady state

Steady states are obtained by satisfying the condition that the derivative of the flow is zero as

$$\dot{\chi} = F(\chi, \mu) = 0\,. \tag{2.17}$$

For a set of nonlinear parameterized equations, many steady states can exist. It is not easy to locate all the zeros of the function $F(\chi, \mu)$. However in a thermoacoustic system, the trivial steady state indicates the unperturbed mean configuration, and hence, is always a physically realizable state. Stability of a steady state can be determined by the eigenvalues of the Jacobian matrix of the corresponding linearized system as stated by the Hartman-Groβman linearization theorem (Crawford, 1991). If $\chi = \bar{\chi} + \delta\chi$ is a state near the steady state $\bar{\chi}$, the linearized system can be written as

$$\delta\dot{\chi} = F_\chi(\bar{\chi}, \mu)\delta\chi\,. \tag{2.18}$$

Here $F_\chi(\bar{\chi}, \mu)$ is the Jacobian matrix whose eigenvalues λ_i determine the stability of the steady state $\bar{\chi}$. If the real parts of all λ_i are less than zero, then the system is linearly stable.

Given two nearby steady states (χ_0, μ_0) and $(\chi_0 + \delta\chi, \mu_0 + \delta\mu)$, the solution com-

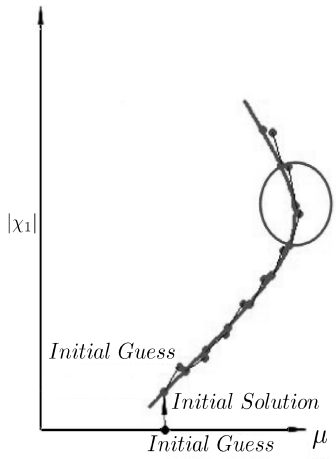

Figure 2.8: Continuation of a solution component by the arc-length continuation method.

ponent $\Gamma(\chi_0, \mu_0)$ can be obtained by numerical continuation. This method relies on the implicit function theorem which states that, for a continuously differentiable system, the steady states are continuous functions of the parameters of the system (Crawford, 1991). Distance between two solutions of the system along the solution component is called the arc-length (Rabinowitz, 1977). Keller proposed that the projection of the arclength along the tangent of the solution component, called as the pseudo-arclength s to be the ideal way to parameterize a curve (Rabinowitz, 1977). In pseudo-arclength continuation, we consider χ and μ to be functions of an unknown parameter s, which is the pseudo-arclength. The equation to be solved thus becomes

$$F(\chi(s), \mu(s)) = 0 \tag{2.19}$$

Having introduced an unknown variable s, we close the above set of equations with the additional constraint that the next point in the solution component lies within a distance specified by the arc-length s between the previous two known solutions given by the circle in Fig. 2.8. This condition takes the form

$$\left(\frac{d\chi}{dt}\right)^2 + \left(\frac{d\mu}{dt}\right)^2 = 1\,. \tag{2.20}$$

We calculate the derivatives $d\chi/ds$ and $d\mu/ds$ at every step and use it to predict a new steady state along the solution component. Iterations with Newton's method (Press, 1999) then provide a converged solution for a new steady state along the solution

component.

2.5.2 Periodic solution

Periodic solutions satisfy the constraint $\chi(t) = \chi(t+T)$ in addition to satisfying the equation for flow of the system. Strobing the periodic solution at its principal time period T can produce a discrete time series of states as

$$\chi(t+T) = F_T(\chi(t), \mu)\,. \tag{2.21}$$

The above equation for corresponding instances in a periodic solution is the same as the equation of a map given in Eqn. 2.16 and F_T is the monodromy matrix (Hillborn, 1994). The stability of the periodic solution is determined by the eigenvalues of the monodromy matrix known as Floquet multipliers (Seydel, 1988). When two nearby periodic solutions are obtained from time marching technique, the solution component of the periodic solutions can be continued by considering the periodic solutions of a flow as the steady states of the corresponding map as explained in the previous subsection.

Numerical continuation is a very efficient method to obtain bifurcation plots for reduced order models of physical systems. However it should be noted that the different types of equations encountered in models of physical systems require special attention during the analysis stage. For example, delay differential equations encountered in models with an explicit time delay must be continued with methods which can handle the time delay. The numerical continuation package used in Chapter 3 called DDE-BIFTOOL (Engelborghs *et al.*, 2002) is capable of handling delay differential equations.

2.6 Tools for nonlinear time series analysis

Evolutions of a system can be analyzed to classify the nature of their asymptotic state. This approach is very useful in two scenarios. The first scenario occurs when the system under consideration lies beyond the range of secondary bifurcation. It has been noted at

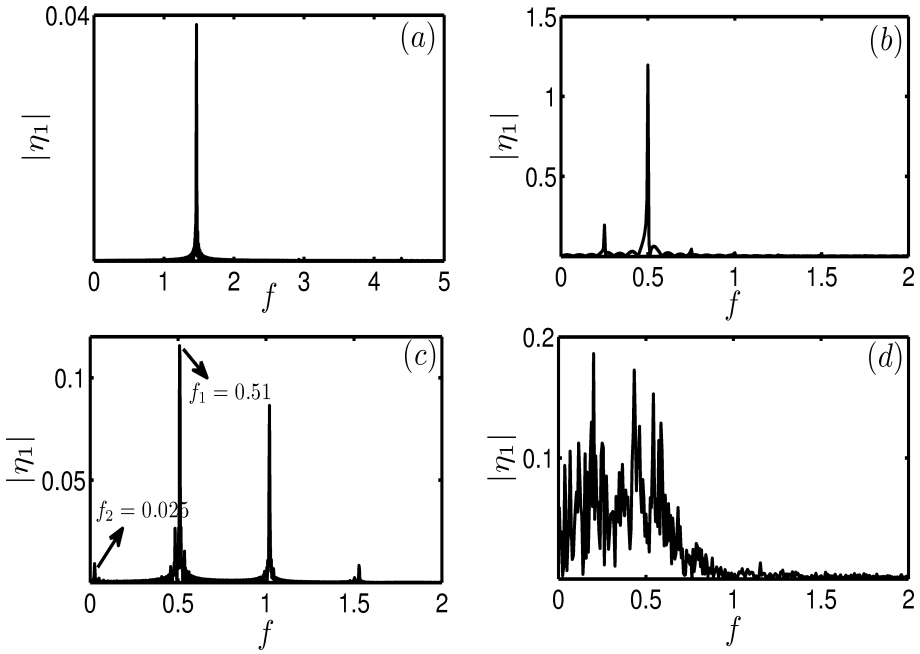

Figure 2.9: Frequency spectrum in time evolution during a (a) Limit cycle (b) Period-2 (c) Quasiperiodic and (d) Chaotic oscillation.

the end of Section 2.3 that the routes to chaos beyond secondary bifurcations are specific to the system under consideration. The particular route to chaos in a given system is identified by performing time series analysis on the asymptotic state of the evolution at different parameter values. The second scenario is the analysis of experimental data. Complete information of the state is not available in experiments and often only a few system variables can be measured. Even under these restrictions, time series analysis is capable of characterising the nature of the asymptotic state of the system (Abarbanel, 1996).

A common tool used in time series analysis to identify the asymptotic state of the system is Fast Fourier Transform (FFT). This method identifies the frequency content of a given evolution. Figure 2.9 (a) shows the frequency content during a limit cycle with a dominant peak at the frequency corresponding to the unstable eigenmode. Period 2 oscillations exhibit peak at a sub-harmonic frequency as shown in Fig. 2.9 (b). Quasiperiodic oscillations display incommensurate frequencies in Fig. 2.9 (c) while chaotic trajectories give rise to a nearly continuous spectrum in FFT as shown in Fig. 2.9 (d).

The Lyapunov exponent of a dynamical system characterizes the rate at which two

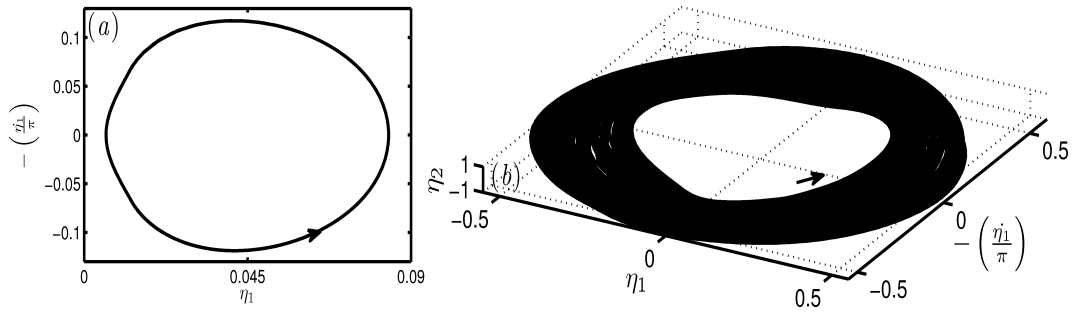

Figure 2.10: Phase portraits (a) Limit cycle (b) Quasi-periodic orbit.

nearby trajectories separate (Strogatz, 2000). Predictability of a nearby trajectory is increased if the Lyapunov exponent is negative. This indicates that the two trajectories are evolving towards a common attractor. When two trajectories evolve to the same asymptotic state, the distance between the two trajectories vanishes. This is observed when two trajectories evolve to the same limit cycle as shown in Fig. 4.15. The Lyapunov exponent asymptotically tends to the value of zero in this case. Conversely, a positive value for the Lyapunov exponent indicates that the two nearby trajectories are evolving exponentially away from one another. Therefore a positive value for the Lyapunov exponent is indicative of a chaotic system.

Given a system with N state variables, an N-dimensional phase space can be obtained where each possible state of the system is a point. A visual display of a trajectory in phase space is called as a phase portrait (Crawford, 1991; Strogatz, 2000). Phase portraits are very useful in characterizing time evolutions as the phase portrait of a limit cycle forms a closed orbit as shown in Fig. 2.10 (a). Phase portraits of quasiperiodic orbits span the surface of a torus as shown in the 3-dimensional plot in Fig. 2.10 (b). Arrows in the phase portraits indicate the direction of time.

A section of a phase portrait by a transversal plane of $N - 1$ dimensions gives a Poincare map of the trajectory (Hillborn, 1994). The transversality of the Poincaré section implies that the trajectories of the system flow perpendicular to it in the phase space. In this thesis, the two-sided Poincare map of the time evolutions are plotted in Figs. 2.11 ($a - d$). The Poincare map or the first return map of a limit cycle shows two distinct points in Fig. 2.11 (a) while that of a period-2 trajectory shows 4 points in Fig. 2.11 (b). The Poincare map of a quasiperiodic trajectory in Fig. 2.11 (c) shows that successive intersections of the trajectory with the Poincare section forms a set of points

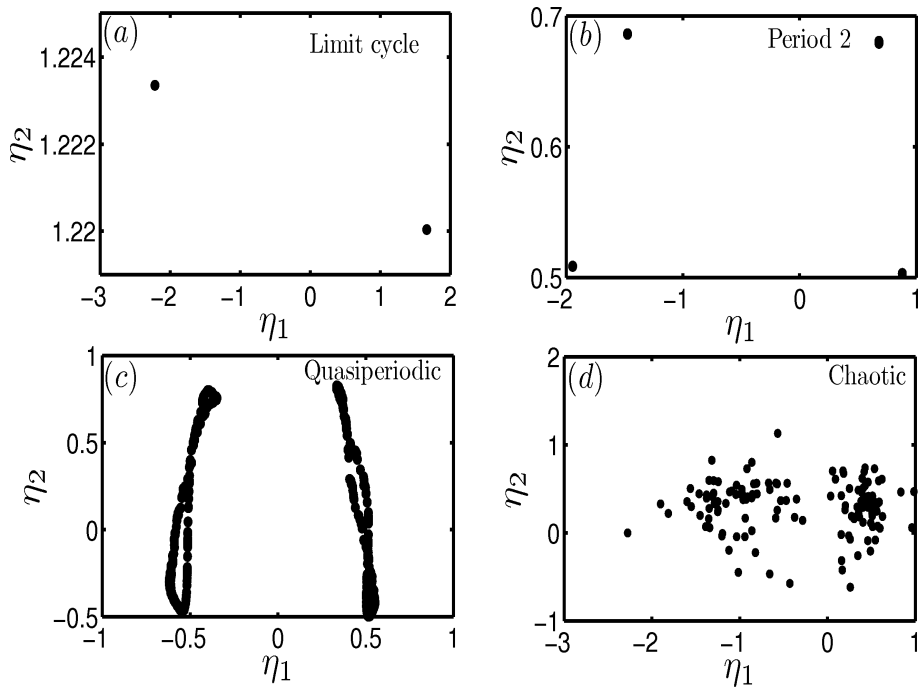

Figure 2.11: Poincare maps for different asymptotic states (a) Limit cycle (b) Period 2 (c) Quasiperiodic (d) Chaotic orbits.

on the surface of a torus. Chaotic evolutions of the system display a set of points in the Poincare map as shown in Fig. 2.11 (d). (Strogatz, 2000).

The above mentioned tools from dynamical systems' theory for nonlinear time series analysis are employed in the present thesis to characterize the asymptotic state of thermoacoustic systems. The method of numerical continuation has been applied to obtain the bifurcation plots for the variation of system parameters in a horizontal Rijke tube in Chapter 3 and a ducted premixed flame in Chapter 4. Fourier transforms and Lyapunov exponents have been calculated while phase portraits and Poincare sections have been plotted to classify the evolutions according to their asymptotic state.

CHAPTER 3

BIFURCATION ANALYSIS OF THERMOACOUSTIC INSTABILITY IN A HORIZONTAL RIJKE TUBE

3.1 Thermoacoustic instability in a Rijke tube

Rijke tube is a simple thermoacoustic device, which has the essential physics of thermoacoustic interaction. It consists of a duct which is open at both ends and a heat source (in the present case, an electrical heater) positioned at some axial location within it. Self sustained thermoacoustic oscillations are observed in a Rijke tube when the heater is positioned at certain axial locations of the tube and beyond some threshold power level (Rijke, 1859). In a vertical Rijke tube, the power level determines the temperature at the surface of the electrical heater and thereby regulates the mean flow through the tube which is set up due to natural convection. In order to side-step the difficulty of modeling natural convection in the vertical arrangement, a horizontal Rijke tube is considered. The mean flow is maintained at a desired flow rate using a blower (Katto and Sajiki, 1977; Heckl, 1990; Matveev, 2003*b*).

In a linearly unstable configuration, the oscillations grow exponentially from small amplitudes and eventually reach a limit cycle. A linearly stable system can exhibit sub-critical transition to instability, depending on the amplitude of the initial condition and is termed as triggering (Wicker *et al.*, 1996). The sub-critical transition to instability is manifested as hysteretic behavior (Matveev, 2003*b*) in experiments. Estimation of the amplitude of acoustic oscillations during limit cycle is important from the design point of view for gas turbines (Zinn and Lieuwen, 2006). As linear stability analysis cannot predict the limit cycle characteristics, nonlinear stability analysis or bifurcation analysis of thermoacoustic instability is necessary. For this, the nonlinearity in the heat release rate response of the heater has to be included (Kwon and Lee, 1985) in the analysis. The heat source was also modelled as a heated flat plate (Hantschk and Vortmeyer,

1999) or as a circular cylinder (Mariappan and Sujith, 2010*a*) using computational fluid dynamic (CFD) techniques. The transfer functions obtained from CFD simulations of flow around heated cylinders (Kwon and Lee, 1985) have been used to study the bifurcation plot of a Rijke tube (Matveev, 2003*b*).

In most cases, solving the governing equations to obtain the unsteady heat transfer from the heater is computationally expensive. For those cases, a low order model is used to simulate the nonlinear response of the heater. Heckl (1990) used a modified form of King's Law (King, 1914) to arrive at a correlation between the heat release rate and acoustic velocity fluctuation in a horizontal Rijke tube. This correlation relates the unsteady heat release rate at time t to the acoustic velocity fluctuations at the heater location at time $(t - \tau)$. The correlation contains an explicit time delay which was determined using the formula given by Lighthill (1954). Heckl's correlation was used to construct a model for a horizontal Rijke tube by Balasubramanian and Sujith (2008*c*). They observed that this low order model retained diverse dynamical behaviors such as the attainment of a limit cycle and sub-critical transition to instability. In this chapter, analytical and numerical results from the the above mentioned low order model are compared with experimental results obtained by Matveev and Culick (2003) and Song *et al.* (2006).

The approach of systematically varying a parameter and tracking the evolution of the system for different initial conditions can provide the bifurcation plot Mariappan and Sujith (2010*a*). However, this method of obtaining the bifurcation plot is computationally intensive. Moreover, the basins of attraction obtained for the limit cycle and the steady state remain specific to the type of initial condition applied, making it not suited for systems which exhibit triggered instability (Ananthkrishnan *et al.*, 2005). Therefore, alternate methods of obtaining the bifurcation plots efficiently must be identified.

Triggered instability which is exhibited as hysteresis, is an indication of sub-critical Hopf bifurcation followed by a fold bifurcation. Critical points on the hysteresis curve can be obtained by analytical methods. Classical linear stability analysis based on eigenvalues can be employed to obtain the Hopf points or the bounds of linear stability. Analytically, the method of multiple scales can provide information about the nature of the Hopf bifurcation (Nayfeh and Balachandran, 1990) and the method of har-

monic balancing (Vidyasagar, 1993) can locate the fold points in a hysteretic system. The method of multiple scales was applied to a model for feedback control system to obtain the amplitude modulation equations by Nayfeh and Balachandran (1995). It was extended to systems with explicit delay by Das and Chatterjee (2002). Saha *et al.* (2009) obtain the amplitude and stability of limit cycles near the Hopf bifurcation point from the equivalent slow-flow equations to be derived in Section 3.4.2. The method of harmonic balance converts the problem of determining a periodic solution of a system into finding the roots of an algebraic equation (Nayfeh and Balachandran, 1990, 1995). Fold points of a hysteresis curve can be determined using the method of harmonic balance.

Numerical continuation method (Allgower and Georg, 2003; Ananthkrishnan *et al.*, 2005) is an approach to obtain bifurcation plot of a model. This method aims to solve a set of parameterized nonlinear equations iteratively given an initial guess for the state of the system. Solutions which satisfy the set of equations and are additionally connected to a given state of the system are tracked for a given smooth variation of one or more parameters. Bifurcations are identified by including multiple test functions which change sign at the critical value of the parameter. This method has the advantage that once a stationary or periodic solution has been computed, the dependence of the solution on the variation of a parameter is obtained efficiently as compared with the direct time integration technique described earlier. It can also be used to compute unstable limit cycles. In numerical continuation, different types of equations encountered in models of physical systems require special attention during analysis. As an example, numerical continuation methods used for models containing delay differential equations must be capable of handling time delay systems. This is essential in the present investigation as the low order model used for the Rijke tube contains an explicit delay term.

Numerical continuation methods for delay systems have been developed by Engelborghs and Roose (1999). Their software called DDE-BIFTOOL, has been used to obtain the bifurcation results in the present chapter. The rest of this paragraph details the numerical schemes used in the continuation of delay differential equations. In DDE-BIFTOOL (Engelborghs and Roose, 1999) the steady state of the system is determined iteratively using a Newton-Raphson scheme. The obtained steady state is then used to continue the solution curve for variations of one or more chosen parameters of the

system. A system of delay differential equations has an infinite number of eigenvalues associated with the steady state which govern its stability. The dominant eigenvalues determined by a cut-off based on the value of their real part are evaluated numerically and the Hopf bifurcation points are detected. To obtain the periodic solutions of the system, periodicity of the evolution is enforced using an orthogonal collocation method (Engelborghs *et al.*, 2002). Branches of periodic solutions with variations of relevant parameters are obtained analogous to the branches of the fixed points and their stability is estimated by calculating the dominant Floquet multipliers.

In the present investigation, the following system parameters are varied; the non-dimensional heater power K, location of heater y_f, damping coefficient c_1 and the time lag τ. The rest of the chapter is organized as follows. Section 3.2 describes the low order model for the Rijke tube. Analysis of the bifurcation and stability plots are explained in Section 3.3. Section 3.4 lists the derivation used in the analytical methods. Analytical methods are used to locate the Hopf point, the nature of the Hopf bifurcation and to locate the fold point. The results of bifurcation analysis from numerical continuation for various parameters are listed in Section 3.5. Observed interesting dynamical behavior such as quasi-periodicity, period-doubling route to chaos and co-existing multiple attractors are compiled in Section 3.6. Comparison of analytical estimates for the bifurcation plot with numerical results is performed in Section 3.7. Section 3.8 deals with the comparison of numerical results with experimental data. The results of the analysis are summarized in Section 3.9.

3.2 Model for Rijke tube

The Rijke tube model used in the present chapter closely follows Balasubramanian and Sujith (2008*c*) and is for the geometry shown in Fig. 3.1. This model is governed by the non-dimensional linearized momentum and energy equations for the acoustic field as given below in Eqns. (3.1) and (3.2). The scales for non-dimensionalisation are as given in expression (3.3).

$$\gamma M \frac{\partial u'}{\partial t} + \frac{\partial p'}{\partial y} = 0\,, \tag{3.1}$$

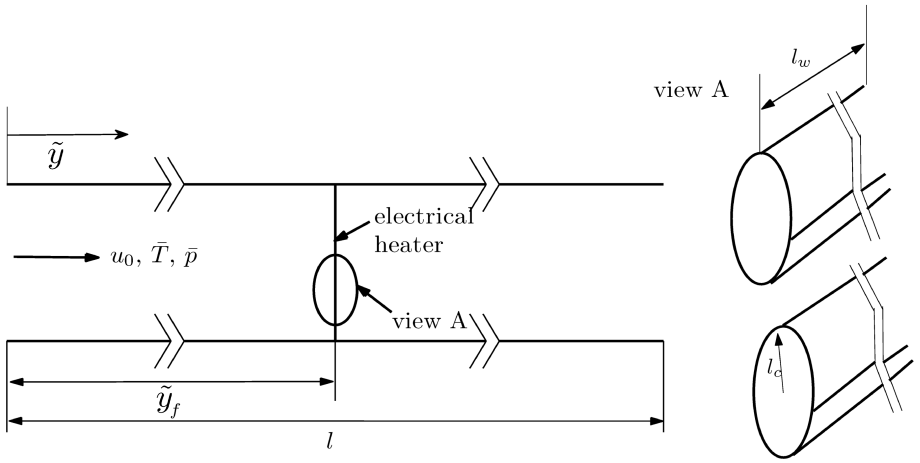

Figure 3.1: Configuration of a horizontal Rijke tube with an electric heater as source.

$$\frac{\partial p'}{\partial t} + \gamma M \frac{\partial u'}{\partial y} + \zeta p' = (\gamma - 1)\dot{Q}'(t)\delta(y - y_f)\,. \tag{3.2}$$

$$y = \frac{\tilde{y}}{l};\; t = \frac{c_0}{l}\tilde{t};\; u' = \frac{\tilde{u}'}{u_0};\; p' = \frac{\tilde{p}'}{\bar{p}};\; M = \frac{u_0}{c_0}\,. \tag{3.3}$$

In this model, y is the distance along the axial direction, l is the length of the duct and t is time. The flow has a steady state velocity u_0, pressure $\bar{p}$ and temperature $\bar{T}$ as shown in the Fig. 3.1, with u' as acoustic velocity and p' as acoustic pressure. Here, γ is the ratio of specific heats of the medium, c_0 is the speed of sound and M is the Mach number of the mean flow. Additionally, ζ is the damping coefficient and $\dot{Q}'$ is the heat release rate fluctuations per unit area due to the electrical heater. Quantities with tilde are dimensional and those without tilde are non-dimensional.

The response of the heat transfer from the wire filament to acoustic velocity fluctuations is quantified using the correlation given by Heckl (1990). This correlation quantifies the quasi-steady heat transfer from a heated cylinder to the flow around it (King, 1914). King's law predicts nonlinear relation between the unsteady heat release rate and the acoustic velocity perturbations u' only for $|u'|$ greater than the mean flow velocity $\bar{u}$. However, experiments performed by Heckl (1990) indicated that nonlinear effects become significant when $|u'| > \bar{u}/3$ which is included in the heat release rate correlation as a factor $1/3$. A time lag is introduced in the correlation in order to include for the thermal inertia of the heat transfer (Heckl, 1990). The heat release rate fluctuations can then be rewritten in terms of the acoustic velocity fluctuations as given

in Eqn. (3.4).

$$\dot{Q}'(t) = \frac{2L_w(T_w - \bar{T})}{S\sqrt{3}c_0\bar{p}}\sqrt{\pi\lambda C_V u_0 \bar{\rho} l_c}\left[\sqrt{\left|\frac{1}{3} + u'_f(t-\tau)\right|} - \sqrt{\frac{1}{3}}\right] . \tag{3.4}$$

The energy equation can be modified as given below by including the correlation for heat release rate fluctuations:

$$\begin{aligned}\frac{\partial p'}{\partial t} + \gamma M\frac{\partial u'}{\partial y} + \zeta p' &= (\gamma - 1)\left(\frac{2L_w(T_w - \bar{T})}{S\sqrt{3}c_0\bar{p}}\right) \\ &\quad \sqrt{\pi\lambda C_V u_0 \bar{\rho} l_c}\left[\sqrt{\left|\frac{1}{3} + u'_f(t-\tau)\right|} - \sqrt{\frac{1}{3}}\right]\delta(y - y_f)\,,\end{aligned} \tag{3.5}$$

where $l_c,\ L_w$ and T_w are the radius, length and temperature of the wire respectively, S is the cross sectional area, $\bar{\rho}$ is the mean density, λ is the thermal conductivity and C_V is the specific heat at constant volume of the medium within the duct.

The non-dimensional partial differential equations Eqn. (3.1) and Eqn. (3.5) can be reduced to a set of ordinary differential equations by expanding the acoustic variables in terms of basis functions using the Galerkin technique (Zinn and Lores, 1971). The Galerkin basis functions chosen here are the natural acoustic modes of the duct in the absence of a heater. The duct modes in the absence of the heater have non-dimensional frequencies $f = 0.5j$ and time periods $T = 2/j$ for $j = 1$ to N. In the following expressions $k_j = j\pi$ refers to the non-dimensional wave number and $\omega_j = j\pi$ refers to the non-dimensional angular frequency of the j^{th} duct mode. It should be noted that with the present scales of non-dimensionalisation, the non-dimensional wave number k_j and the non-dimensional angular frequency ω_j have identical values.

$$u' = \sum_{j=1}^{N}\cos(k_j y)\,\eta_j(t)\,, \tag{3.6}$$

$$p' = \gamma M\sum_{j=1}^{N}\sin(k_j y)\left(\frac{-\dot{\eta}_j(t)}{j\pi}\right). \tag{3.7}$$

$$\frac{d\eta_j}{dt} + k_j \left(\frac{-\dot{\eta}_j}{j\pi} \right) = 0 \,, \tag{3.8}$$

$$\frac{d}{dt}\left(\frac{-\dot{\eta}_j}{j\pi} \right) + 2\zeta_j \omega_j \left(\frac{-\dot{\eta}_j}{j\pi} \right) - k_j \eta_j = K \left[\sqrt{\left| \frac{1}{3} + u'_f(t-\tau) \right|} - \sqrt{\frac{1}{3}} \right] \sin(k_j y_f) \,. \tag{3.9}$$

Here, $\zeta = 2\omega_j \zeta_j$ is the expression for frequency dependent damping where ζ_j is given by Sterling and Zukowski (1991); Matveev (2003a) as shown in Eqn. (3.10) and c_1 and c_2 are the damping coefficients which can be varied and which control the amount of damping in the system.

$$\zeta_j = \frac{1}{2\pi} \left(c_1 \frac{\omega_j}{\omega_1} + c_2 \sqrt{\frac{\omega_1}{\omega_j}} \right) \,, \tag{3.10}$$

The resulting set of equations as given in Eqns. (3.8) and (3.9) are evolved in time. Here, the expression for the non-dimensional heater power (K) is given by,

$$K = \frac{4(\gamma - 1) L_w}{\gamma M c_0 \bar{p} S \sqrt{3}} (T_w - \bar{T}) \sqrt{\pi \lambda C_V u_0 \bar{\rho} l_c} \,. \tag{3.11}$$

The equations can be simplified by expanding the term under the square root in Eqn. (3.9) under the assumptions of small acoustic velocity at the flame $\left(u'_f\right)$ and small time lag (τ). The resulting equation, valid in the limit of small time lag, is written as given below in Eqn. (3.12).

$$\begin{aligned} \frac{d}{dt}\left(\frac{-\dot{\eta}_j}{j\pi} \right) &+ 2\zeta_j \omega_j \left(\frac{-\dot{\eta}_j}{j\pi} \right) - k_j \eta_j \\ &= K \frac{\sqrt{3}}{2} \sin(k_j y_f) \sum_{i=1}^{N} \cos\left(k_i y_f\right) \left[\eta_i + \tau \left(\frac{-\dot{\eta}_i}{i\pi} \right) \right] . \end{aligned} \tag{3.12}$$

Considering a single mode analysis, the Eqns. (3.8) and (3.9) can be further modified as given below where η and $(-\dot{\eta}/\pi)$ are the temporal coefficients of the first acoustic velocity and acoustic pressure mode respectively.

$$\frac{d}{dt}\eta + \pi \left(\frac{-\dot{\eta}}{\pi} \right) = 0 \,, \tag{3.13}$$

$$\frac{d}{dt}\left(\frac{-\dot{\eta}}{\pi}\right) + 2\zeta_1\pi\left(\frac{-\dot{\eta}}{\pi}\right) - \pi\eta = K\left[\sqrt{\left|\frac{1}{3} + cos(\pi y_f)\eta(t-\tau)\right|} - \sqrt{\frac{1}{3}}\right] sin(\pi y_f)\,. \tag{3.14}$$

Substituting Eqn. (3.13) in Eqn. (3.14), a second order delay differential equation is obtained as,

$$\ddot{\eta} + 2\zeta_1\pi\dot{\eta} + \pi^2\eta + \Delta\left[\eta(t-\tau) - \frac{3}{4}cos(\pi y_f)\eta(t-\tau)^2 + \frac{9}{8}cos(\pi y_f)^2\eta(t-\tau)^3\right] = 0\,. \tag{3.15}$$

where $\Delta = \sqrt{3}K\pi sin(2\pi y_f)/4$.

Equations (3.13), (3.14) and (3.15) will be used to analytically determine the linear and nonlinear stability boundaries and also to characterize the limit cycle behavior of the system near the loss of linear stability in Section 3.4.

3.3 Analysis

3.3.1 Steady-state equilibrium and linear stability analysis

The effect of infinitesimal perturbations on the evolution of the system about a steady state is investigated in linear stability analysis. If the evolution moves away from the steady state, the system is unstable and if the evolution approaches the steady state, then the system is stable. This refers to the local analysis of the stability of the system near a steady state. On the other hand, nonlinear stability analysis follows the effect of a finite amplitude perturbation to the system and is used to characterize the resulting asymptotic state.

As an initial step in performing the stability analysis of a steady-state equilibrium solution for given parameter values, the steady state of the system for the given set of parameters has to be calculated. Next linear (local) stability of the obtained equilibrium is identified by examining the eigenvalues of the system linearized around the equilibrium. This calculation is performed analytically by the linear stability analysis or numerically by DDE-BIFTOOL using the Newton's method.

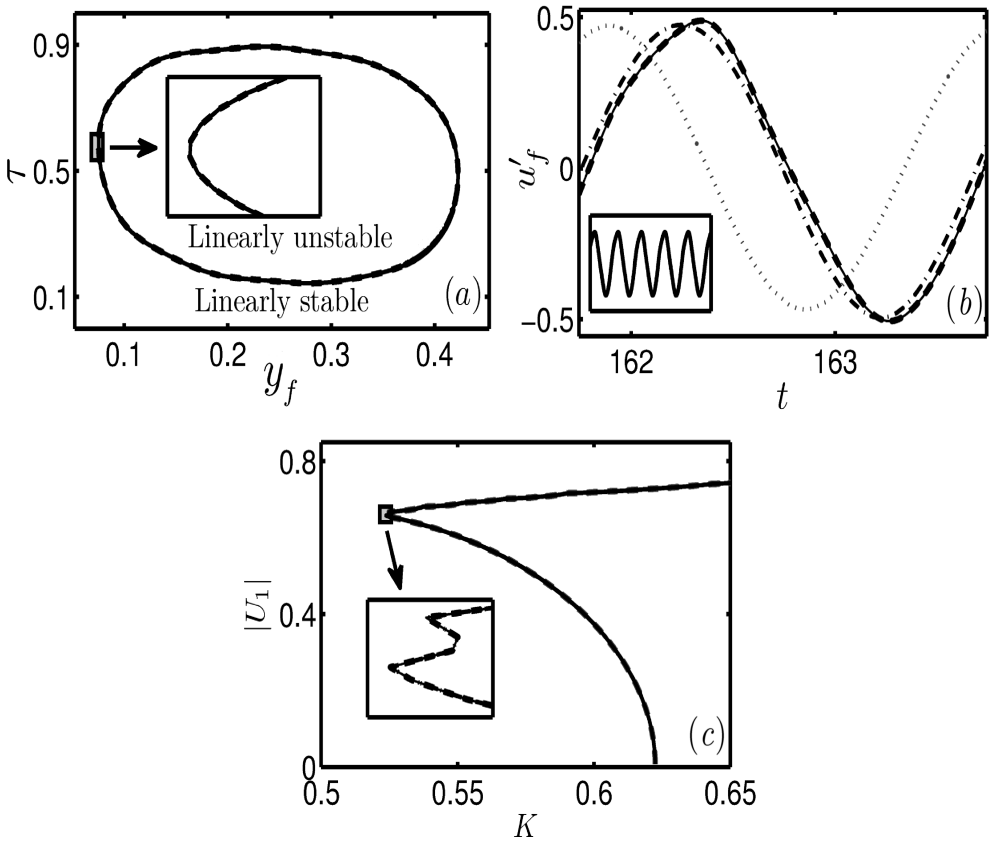

Figure 3.2: Modal convergence of linear stability boundary between y_f and τ with (a) $c_1 = 0.1$, $c_2 = 0.06$ and $K = 0.8$. In this Figure, $\cdots\cdots$ N = 1, $\cdot-\cdot-\cdot$ N = 2, $- - -$ N = 9 and —— N = 10. (b) Comparison of limit cycle amplitude from time evolutions with different number of acoustic Galerkin modes N with $y_f = 0.3$ and $\tau = 0.2$ for case shown in 3.2 (a). (c) Comparison of bifurcation plots for variation of non-dimensional heater power K with different number of acoustic Galerkin modes N for system in 3.2 (a). Grey areas are enlarged in inset figures to show convergence with increase in number of modes.

If all the eigenvalues lie on the left half plane, the equilibrium is linearly stable to small perturbations. When one or more eigenvalues of the linearized system lie on the right half plane, the system is said to be linearly unstable. Stability properties of the equilibrium is therefore changed when the real part of the most dominant eigenvalue crosses zero as some relevant parameter of the system is varied. The value of the parameter at which the real part of the most dominant eigenvalue is zero is called the bifurcation point.

The behavior of the system changes as this value of the parameter is crossed since the equilibrium solution loses stability. New steady states emerge from the bifurcation point depending on the type and nature of the bifurcation to be discussed in the next

section. Once a bifurcation point is located with respect of one parameter, the bifurcation point itself is continued with a variation in a second relevant parameter of the system. The resulting branch of bifurcation points gives us the linear stability boundary which separates regions in the relevant parameter space with linearly stable and unstable equilibrium. This stability boundary is a manifold (Hillborn, 1994) in the space of all the free parameters of the system, but is most conveniently represented by a curve in several appropriate two-dimensional projections.

A typical stability boundary for free variation of the heater location and the time lag of the system is shown in Fig. 3.2 (a). Figure 3.2 shows that for the chosen set of fixed parameter values for the damping and the heater power, the system is linearly unstable for a chosen range of heater locations y_f depending on the time lag τ of the system and vice versa. For very low and reasonably large values of τ such as $\tau < 0.15$ and $\tau > 0.85$ in Fig. 3.2(a), the system is linearly stable for any heater location. Only in the range $0.15 < \tau < 0.85$, the equilibrium solution can become unstable depending on the heater location. The stability boundary is obtained for different number of acoustic Galerkin modes and the results are plotted in Fig. 3.2(a). In this figure, it is seen that the stability boundary for different number of acoustic Galerkin modes from 1 mode to 10 modes show little variation. Therefore a single mode analysis of the Rijke tube system can accurately reproduce the stability boundary of a system with higher number of modes. Determination of the number of Galerkin modes required to accurately capture the linear and nonlinear behavior of the system is termed as modal convergence in the caption of Fig. 3.2.

3.3.2 Numerical simulation, limit cycles and nonlinear analysis

The bifurcation points at the linear stability boundaries obtained in the previous section are associated with a pair of complex conjugate eigenvalues crossing the imaginary axis and accordingly there is a Hopf bifurcation. At the Hopf bifurcation point, the steady state looses stability and becomes unstable, and isolated periodic solutions called limit cycles emerge. The stability of the emerging branch of limit cycles decides the type or nature of the Hopf bifurcation. The two types of Hopf bifurcation are sub-critical and

super-critical Hopf bifurcations as explained in Chapter 2. In a sub-critical Hopf bifurcation, the branch of unstable limit cycles forms a region of bistability where the steady solution is stable to small perturbations but is unstable to large perturbations. However this branch of unstable limit cycle might undergo a fold bifurcation and stabilize. For values below the fold point the steady solution is stable to perturbations of any magnitude and hence are globally stable. Therefore in the case of a sub-critical bifurcation, the linear (local) and nonlinear (global) stability boundaries are different. If however the limit cycles are stable the system smoothly evolves from a stable steady solution to an unstable steady solution with progressively increasing limit cycle amplitudes. This type of bifurcation is called a super-critical Hopf bifurcation.

We first check the existence of limit cycles in our model and the convergence of the number of acoustic Galerkin modes. For this, the time evolutions of the system with different number of acoustic modes for system parameters in the linearly unstable region are compared in Figs. 3.2 (b). It can be seen from Figs. 3.2 (b) that there is a limit cycle and also that the amplitude of the limit cycle shows very little variation with an increase in the number of acoustic Galerkin modes. The variation in the phase of the various solutions can be attributed to initial conditions. In fact, the difference in the solutions with different numbers of acoustic modes is not visible when the phase difference is compensated. This feature can be seen more easily from Figure 3.2(c) wherein we have plotted the variation of the amplitudes of the first Galerkin mode with a variation in the heater power K. In fact the measure used to quantify the asymptotic state ($t \rightarrow \infty$) of the system in Figure 3.2(c) is the difference between the maximum and minimum value ($|\eta_1|$) of the non-dimensional first acoustic velocity mode.

In Fig. 3.2, it is seen that when the damping coefficient c_1 is greater than 0.1, a single mode analysis is sufficient to obtain the bifurcation plot of the system. Large damping coefficients imply that the higher modes are damped more effectively. Therefore, systems with large damping values can be analyzed using a single mode analysis. In the following section, analytical methods are employed in a single mode analysis to obtain the bifurcation plot of the Rijke tube system. Throughout this chapter, numerical results obtained for a system with $N = 10$ using DDE-BIFTOOL (Engelborghs and Roose, 1999) which are compared with the analytical and experimental results.

3.4 Analytical methods for bifurcation analysis

3.4.1 Linear stability analysis

The reduced order model for the Rijke tube consists of a single mode approximation and is given by Eqns. (3.13) and (3.14). They can be rewritten as a set of delay differential equations in the form

$$\dot{\chi}(t) = [B]\chi(t) + [R]\chi(t-\tau)\,, \tag{3.16}$$

with $\chi = [\eta\,(-\dot{\eta}/\pi)]^T$, $B = \begin{bmatrix} 0 & -\pi \\ \pi & -2\pi\zeta_1 \end{bmatrix}$ and $R = \begin{bmatrix} 0 & 0 \\ \frac{\sqrt{3}K}{4}\sin(2\pi y_f)e^{-\lambda\tau} & 0 \end{bmatrix}$.
The characteristic equation of this set of delay differential equations is

$$det([B] + [R]e^{-\lambda\tau} - \lambda I) = 0\,. \tag{3.17}$$

into which the substitution of $[B]$ and $[R]$ leads to the following equation with the constants $a_0 = 2\pi\zeta_1$; $a_1 = \pi^2$; $a_2 = \frac{\sqrt{3}K\pi}{4}sin(2\pi y_f)$.

$$\triangle(\lambda,\tau) = \lambda^2 + a_0\lambda + a_1 + a_2e^{-\lambda\tau} = 0\,. \tag{3.18}$$

As the consequence of the time delay which gives rise to the $e^{-\lambda\tau}$ term, Eqn. (3.18) is a transcendental equation which indicates that the set of delay differential equation has infinite number of eigenvalues (Engelborghs and Roose, 1999).

This Rijke tube model undergoes loss of stability from its steady state through a Hopf bifurcation. This can be illustrated from the linear stability analysis as given in Appendix A. Hopf bifurcation is characterized by a pair of purely imaginary eigenvalues crossing the imaginary axis. Thus, the eigenvalues of the system have purely imaginary values at the Hopf bifurcation point. Including this constraint as $\lambda = \pm i\omega$ in Eqn. (3.18) and equating the real and imaginary parts of the equation separately to zero, we obtain two equations relating the system parameters and the eigenfrequency ω as given in Eqns. (3.19) and (3.20).

$$a_1 - \omega^2 + a_2cos(\omega\tau) = 0\,, \tag{3.19}$$

$$a_0\omega - a_2sin(\omega\tau) = 0\,. \tag{3.20}$$

Obtaining expressions for $\sin(\omega\tau)$ and $\cos(\omega\tau)$ from the above equations and using the relation $\sin^2(\omega\tau)+\cos^2(\omega\tau) = 1$, the transcendental equation in (3.18) can be rewritten in terms of as a fourth order equation of the eigenfrequency ω as below:

$$\omega^4 + (a_0^2 - 2a_1)\omega^2 + (a_1^2 - a_2^2) = 0\,. \tag{3.21}$$

Real roots of equation (3.21) give the ω values at the Hopf bifurcation points and therefore can be used to estimate the Hopf bifurcation point for a given system configuration. The linear stability boundary is obtained as the locus of all the Hopf bifurcation points when two system parameters are simultaneously varied.

Simultaneous variations of the non-dimensional heater power K with the time lag τ, damping coefficient c_1 with the time lag τ and the heater location y_f with the time lag τ are examined. Equations (3.19), (3.20) and (3.21) are re-written such that the parameters which are varying are functions of the frequency ω and the other fixed parameters. For example, the non-dimensional power K and time lag τ can be re-written in terms of the frequency ω and other fixed parameters as

$$K = \left[(\omega^4 + (a_0^2 - 2a_1) + \omega^2 + a_1^2)\frac{16}{3\pi^2\sin^2(2\pi y_f)}\right]^{1/2}\,, \tag{3.22}$$

$$\tau = \frac{1}{\omega}\arctan\left(\frac{a_0\omega}{\omega^2 - \pi^2}\right)\,. \tag{3.23}$$

The frequency ω is then varied to obtain the analytical linear stability boundary.

3.4.2 Nonlinear analysis near Hopf point

We noted in Fig. 3.2(c) that a sub-critical Hopf bifurcation occurred when the non-dimensional heater power is varied. This behavior is obtained for the variation of other parameters of the system as it is an inherent property of the nonlinearity present in the system. To justify this claim, we argue first with a qualitative analysis which is then substantiated with a more rigorous analysis using the method of multiple scales along the lines of Saha *et al.* (2009).

The nature of the bifurcation associated with a source term nonlinearity of the form $(1 \pm X)^{\alpha}$, where X is the state variable and α is a real number which can be identified by expanding the nonlinearity in a series about small X and dropping higher order terms. A binomial expansion of the above expression results in the following equation.

$$1 \pm \alpha X + \frac{\alpha(\alpha-1)}{2!}X^2 \pm \frac{\alpha(\alpha-1)(\alpha-2)}{3!}X^3 + ... \tag{3.24}$$

In the above expression, the signs of the first and the third order terms are seen to be same when $0 < |\alpha| < 1$ and $|\alpha| > 2$. The signs will be different when the value of α lies between $1 < |\alpha| < 2$. The relative signs of the first and the third order term identifies the normal form and dictates the nature of the bifurcation. Whenever these terms have the same sign, the bifurcation is sub-critical while it is supercritical when these terms have different signs. This result has been obtained in the context of machine tool vibrations by Kalmar-Nagy *et al.* (2001) and Wahi and Chatterjee (2005) for $\alpha = 3/4$. In the model for the heat release rate fluctuations in a Rijke tube, $\alpha = 1/2$, which implies that this model will exhibit sub-critical Hopf bifurcation.

The determination of the normal form distinguishes between super- and sub-critical Hopf bifurcations. The method of multiple scales can be used to systematically identify the normal form of a system generated by a differential equation. This method transforms a set of evolution equations into a lower order approximation of amplitude modulation equations (Nayfeh and Balachandran, 1995). The amplitude modulation equations are sufficient to describe the periodic solutions and their stability. The second order equation describing the evolution of the reduced order model of the Rijke tube is given in Eqn. (3.15).

To derive the amplitude modulation equation, the state variables of Eqn. (3.15) are re-scaled as $\eta(t) = \epsilon y(t)$ and expanded about the Hopf bifurcation point in terms of a small parameter $\epsilon << 1$, where ϵ is the difference between the current value of the parameter and its critical value. This scaling is performed in order to separate the terms according to their power in ϵ. Modification of Eqn. (3.15) with the above scaling, written

to $O(\epsilon^2)$ is given below:

$$\begin{aligned} y'' + 2\zeta_1\pi y' + \pi^2 y &+ \Delta\Big[y(t-\tau) - \frac{3}{4}\epsilon\cos(\pi y_f)y(t-\tau)^2 \\ &+ \frac{9}{8}\epsilon^2\cos(\pi y_f)^2 y(t-\tau)^3\Big] + O(\epsilon^3)... = 0\,. \end{aligned} \tag{3.25}$$

When the bifurcation parameter is at the critical value at the Hopf point, e.g. when non-dimensional power is the bifurcation parameter, we set $\Delta = \Delta_c$ to obtain

$$\begin{aligned} y'' + 2\zeta_1\pi y' + \pi^2 y &+ \Delta_c\Big[y(t-\tau) - \frac{3}{4}\epsilon\cos(\pi y_f)y(t-\tau)^2 \\ &+ \frac{9}{8}\epsilon^2\cos(\pi y_f)^2 y(t-\tau)^3\Big] = 0\,. \end{aligned} \tag{3.26}$$

At another point close to the Hopf point with $\Delta_2 = \Delta_c + \epsilon^2\delta$, we have

$$\begin{aligned} y'' + 2\zeta_1\pi y' + \pi^2 y + (\Delta_c &+ \epsilon^2\delta)\Big[y(t-\tau) - \frac{3}{4}\epsilon\cos(\pi y_f)y(t-\tau)^2 \\ &+ \frac{9}{8}\epsilon^2\cos(\pi y_f)^2 y(t-\tau)^3\Big] = 0\,. \end{aligned} \tag{3.27}$$

The underlying idea of the method of multiple scales (MMS) is to consider that the system contains multiple relevant and independent time scales, instead of a single time variable (Nayfeh and Balachandran, 1995). In the present case, we define multiple time scales which include the original time scale $t_0(t) = t$ and the slow time scales of $t_1(t) = \epsilon t$ and $t_2(t) = \epsilon^2 t$. The evolution of the system can now be written in terms of these different time scales as given in Eqn. (3.28) and the time delayed term can be expanded as given in Eqn. (3.29).

$$y(t) = Y(t_0, t_1, t_2) = Y_0(t_0, t_1, t_2) + \epsilon Y_1(t_0, t_1, t_2) + \epsilon^2 Y_2(t_0, t_1, t_2) + ...\,, \tag{3.28}$$

$$\begin{aligned} y(t-\tau) &= Y(t_0 - \tau, t_1 - \epsilon\tau, t_2 - \epsilon^2\tau) \\ &= Y_0(t_0 - \tau, t_1 - \epsilon\tau, t_2 - \epsilon^2\tau) + \epsilon Y_1(t_0 - \tau, t_1 - \epsilon\tau, t_2 - \epsilon^2\tau) + ... \end{aligned} \tag{3.29}$$

The expression in Eqn. (3.29) is further Taylor expanded about $\epsilon = 0$ and the resulting expressions are substituted into Eqn. (3.27). Collecting the zeroth order terms in ϵ

recovers the linear equation as given below:

$$\frac{d^2Y_0(t_0,t_1,t_2)}{dt_0^2}+\zeta_1\frac{dY_0(t_0,t_1,t_2)}{dt_0}+\pi^2Y_0(t_0,t_1,t_2)+\Delta_cY_0(t_0-\tau,t_1,t_2)=0\,, \quad (3.30)$$

whose steady state solution is

$$Y_0(t_0,t_1,t_2)=C_1(t_1,t_2)\sin(\omega t_0)+C_2(t_1,t_2)\cos(\omega t_0)\,. \quad (3.31)$$

The above solution is accurate only until $t < O(1/\epsilon)$. When the system evolves beyond time $t > O(1/\epsilon)$, terms with $O(\epsilon) = 1$ and higher orders also contribute to the solution. The equation for $O(\epsilon) = 1$ after substituting for the solution of Y_0 is given as:

$$\begin{aligned}\frac{\partial^2}{\partial {t_0}^2}Y_1\left(t_0,t_1,t_2\right) &+ \zeta_1\frac{\partial}{\partial t_0}Y_1\left(t_0,t_1,t_2\right)+\pi^2Y_1\left(t_0,t_1,t_2\right)+i_cY_1\left(t_0-\tau,t_1,t_2\right)\\ &+ Q_1\sin\left(\omega\, t_0\right)+Q_2\cos\left(\omega\, t_0\right)\\ &+ Q_3\sin\left(2\omega t_0\right)+Q_4\cos\left(2\omega t_0\right)+Q_5=0\,, \quad (3.32)\end{aligned}$$

where

$$Q_1=\left[\zeta_1-\tau\Delta_c\cos\left(\omega\tau\right)\right]\frac{\partial C_1\left(t_1,t_2\right)}{\partial t_1}-\left[2\,\omega+\tau\,\Delta_c\sin\left(\omega\,\tau\right)\right]\frac{\partial C_2\left(t_1,t_2\right)}{\partial t_1}\,, \quad (3.33a)$$

$$Q_2=\left[2\,\omega+\tau\,\Delta_c\sin\left(\omega\,\tau\right)\right]\frac{\partial C_1\left(t_1,t_2\right)}{\partial t_1}+\left[\zeta_1-\tau\,\Delta_c\cos\left(\omega\,\tau\right)\right]\frac{\partial C_2\left(t_1,t_2\right)}{\partial t_1}\,, \quad (3.33b)$$

$$\begin{aligned}Q_3=\,&3/8\,\Delta_c\cos\left(\pi\,y_f\right)\sin\left(2\omega\,\tau\right)\left[C_1^2\left(t_1,t_2\right)-C_2^2\left(t_1,t_2\right)\right]\\ &+3/4\,\Delta_c\cos\left(\pi\,yf\right)C_1\left(t_1,t_2\right)C_2\left(t_1,t_2\right)\cos\left(2\omega\,\tau\right)\,, \quad (3.33c)\end{aligned}$$

$$\begin{aligned}Q_4=\,&3/8\Delta_c\cos\left(\pi y_f\right)\cos\left(2\omega\tau\right)\left[C_1^2\left(t_1,t_2\right)-C_2^2\left(t_1,t_2\right)\right]\\ &+3/4\,\Delta_c\cos\left(\pi y_f\right)C_1\left(t_1,t_2\right)C_2\left(t_1,t_2\right)\sin\left(2\omega\tau\right)\,, \quad (3.33d)\end{aligned}$$

$$Q_5=-3/8\,\Delta_c\cos\left(\pi\,y_f\right)\left[C_1^2\left(t_1,t_2\right)+C_2^2\left(t_1,t_2\right)\right]\,. \quad (3.33e)$$

As the effects of the original time scale $t_0(t) = t$ have already been included in the solution of Y_0, they must not be included in the solution for Y_1. However, the contributions of the terms $\sin(\omega t_0)$ and $\cos(\omega t_0)$ become non-negligible in the expression for Y_1 when the system evolves past the slow time scale of $t > t_1$. Therefore, in order to avoid the effect of these secular terms (Nayfeh and Balachandran, 1995), the

coefficients of $\sin(\omega t_0)$ and $\cos(\omega t_0)$ are explicitly set to zero. This leads to the conditions that $\partial C_1/\partial t_1$ and $\partial C_2/\partial t_1$ are zero. Equation (3.32) can then be solved for the particular solution of Y_1 as

$$Y_1(t_0, t_1, t_2) = C_3(t_1, t_2) + C_4(t_1, t_2)\sin(2\omega t_0) + C_5(t_1, t_2)\cos(2\omega t_0)\,. \tag{3.34}$$

Substituting the expressions for Y_0 and Y_1 and also using the conditions $\partial C_1/\partial t_1 = 0$ and $\partial C_2/\partial t_1 = 0$ we obtain the equation for $O(\epsilon) = 2$. This equation also has coefficients for sine and cosine components of the original time scale and these secular terms must be set to zero to obtain $\partial C_1/\partial t_2$ and $\partial C_2/\partial t_2$. The rate of change of C_1 and C_2, correct up to the second order, are given by the following expressions:

$$\frac{\partial C_1}{\partial t} = \epsilon\frac{\partial C_1}{\partial t_1} + \epsilon^2\frac{\partial C_1}{\partial t_2} + O(\epsilon^3)\,, \tag{3.35}$$

$$\frac{\partial C_2}{\partial t} = \epsilon\frac{\partial C_2}{\partial t_1} + \epsilon^2\frac{\partial C_2}{\partial t_2} + O(\epsilon^3)\,. \tag{3.36}$$

A co-ordinate transformation to polar co-ordinates is performed as $C_1 = R_1(t)\cos(\phi_1(t))$ and $C_2 = R_1(t)\sin(\phi_1(t))$ such that the original variable can be written as given below.

$$U(t) = \epsilon y(t) = \epsilon R_1(t)\sin\left(t + \phi_1(t)\right)\,. \tag{3.37}$$

If $A_1(t) = \epsilon R_1(t)$ then the equations governing the evolution of the system over the slow time scales are given of the form given in Eqns. (3.38) and (3.39).

$$\frac{dA_1}{dt} = B_1 A_1 + B_2 A_1^3\,, \tag{3.38}$$

$$\frac{d\phi_1}{dt} = B_3 + B_4 A_1^2\,. \tag{3.39}$$

The expressions for B_1 and B_2 are as given in Appendix B. The constant amplitude

at limit cycle is calculated from Eqn. (3.38) as given below.

$$A_1 = \sqrt{\frac{-B_1}{B_2}}\,. \tag{3.40}$$

The stability analysis of the fixed point of the slow flow amplitude Eqn. (3.38) gives the stability of the limit cycle. Information of the stability of the fixed point of the system together with the stability of the limit cycle at the same parameters can be used to identify the type of Hopf bifurcation.

Culick (2006) employed the method of time averaging in a single mode analysis of thermoacoustic instability. The method of time averaging assumes that the Mach number M of the flow is small. It also assumes that the changes in amplitudes and phase takes place much slower than the oscillation frequency. Using these assumptions, equations for the amplitude and phase of the evolution during limit cycle were derived. By setting the rate of change of the amplitude to be zero, the amplitude of the limit cycle at asymptotic time was determined in this analysis. Averaging methods applied to systems with delays assume that the time delay is small (Chatterjee, 2007). However, the method of multiple scales does not require that the delay term to be small and is hence are better suited to the analysis of instabilities in systems with time delay (Saha *et al.*, 2009).

3.4.3 Nonlinear stability analysis

Change in linear stability occurs at the Hopf point and the locus of the Hopf points gives the linear stability boundary of the system. In case of sub-critical Hopf bifurcations, the limit cycles near the Hopf point are themselves unstable and this branch of unstable limit cycles can undergo a fold bifurcation at some finite amplitude of the measure. Thus, for systems exhibiting sub-critical Hopf bifurcations, the stability boundary of the system to finite amplitude disturbances is different from the linear stability boundary defined by the Hopf points. The locus of all these fold points is called the nonlinear stability boundary. Determination of the fold points can be done with the method of harmonic balance. Rewriting equation (3.15) with $a_0 = 2\pi\zeta_1$, $a_1 = \pi^2$ and $a_{2p} =$

$\left(K\pi\sin(\pi y_f)/\sqrt{3}\right)$ we obtain the following equation.

$$\ddot{U} + a_0\dot{U} + a_1 U + a_{2p}\left[\sqrt{|1+3\cos(\pi y_f)U(t-\tau)|} - 1\right] = 0\,. \tag{3.41}$$

In the method of harmonic balance, we assume that the limit cycle is purely a function of a single frequency. Therefore we use the expression $U(t) = A_1 cos(\omega t) + A_2$ in the previous equation. Here, A_1 is the amplitude of the limit cycle and A_2 is the offset of the limit from the mean value.

$$\begin{aligned}(a_1-\omega^2)A_1\cos(\omega t) &+ a_0 A_1\omega\sin(\omega t) + a_1 A_2 \\ &+ a_{2p}\left[\sqrt{|1+3\cos(\pi y_f)(A_1\cos(\omega(t-\tau))+A_2)|} - 1\right] = 0\,.\end{aligned} \tag{3.42}$$

Due to the term under the square root, the above equation can still not be simplified to give different harmonics. Therefore, we expand the term under the square root as given below which is correct till the fundamental frequency. The effect of higher harmonics is collected in the term HH and is assumed to be negligible.

$$\begin{aligned}\sqrt{|1+3\cos(\pi y_f)(A_1\cos(\omega(t-\tau))+A_2)|} &= C_0(y_f,\omega,\tau,A_1,A_2) \\ &+ C_1(y_f,\omega,\tau,A_1,A_2)\cos(\omega t) \\ &+ C_2(y_f,\omega,\tau,A_1,A_2)\sin(\omega t) + HH\,.\end{aligned} \tag{3.43}$$

Here, the Fourier coefficients C_0, C_1 and C_2 are defined as given below in Eqns. (3.44) to (3.46). Substituting these constants in equation (3.42), we obtain equation (3.47) where the effect of different harmonics can be separated.

$$C_0 = \frac{2\pi}{\omega}\int_0^{\frac{2\pi}{\omega}} \sqrt{(1+3\cos(\pi y_f)U(t-\tau))}dt\,, \tag{3.44}$$

$$C_1 = \frac{\omega}{\pi}\int_0^{\frac{2\pi}{\omega}} \sqrt{(1+3\cos(\pi y_f)U(t-\tau))}\cos(\omega t)dt\,, \tag{3.45}$$

$$C_2 = \frac{\omega}{\pi}\int_0^{\frac{2\pi}{\omega}} \sqrt{(1+3\cos(\pi y_f)U(t-\tau))}\sin(\omega t)dt\,. \tag{3.46}$$

$$[(a_1 - \omega^2)A_1 + a_{2p}C_1]\cos(\omega t) + [a_{2p}C_2 - a_0\omega A_1]\sin(\omega t) + [a_1 A_2 + a_{2p}(C_0 - 1)] = 0\,. \tag{3.47}$$

Equating the harmonics separately to zero, we obtain the following three equations for the cosine, sine and constant components as given below. This set of three equations can be solved for the three unknowns A_1, A_2 and ω.

$$(a_1 - \omega^2)A_1 + a_{2p}C_1 = 0\,, \tag{3.48}$$

$$a_{2p}C_2 - a_0\omega A_1 = 0\,, \tag{3.49}$$

$$a_1 A_2 + a_{2p}(C_0 - 1) = 0\,. \tag{3.50}$$

In addition, we assume that the frequency of the periodic solutions of interest is a constant and is equal to the frequency at the loss of linear stability. The validity of this assumption has been verified to hold from numerical analysis using DDE-BIFTOOL. Therefore, one of the above equations becomes redundant. In this paper, we consider Eqn. (3.49) to be redundant. Once a system has been specified, the above Eqns. (3.48) and (3.50) can be used to solve for the amplitude of the limit cycle and the offset of the limit cycle from the mean. However, the inverse problem of identifying a single parameter value given all other parameters and the limit cycle amplitude is easier to solve as the Fourier coefficients can be numerically evaluated.

In order to obtain the parameter value at the fold point, we make use of the fact that at the fold point, the term $\sqrt{1 + 3\cos(\pi y_f)(A_1\cos(\omega(t-\tau)) + A_2)}$ vanishes. This condition serves to relate A_1 and A_2 thus leaving only Eqn. (3.50) to be solved to obtain the unknown parameter value at the fold point. We simplify the expression within the square root as given below:

$$1 + 3\cos(\pi y_f)(A_1\cos(\omega(t-\tau)) + A_2) = 0\,. \tag{3.51}$$

$$A_1\cos(\omega(t-\tau)) = \left[\frac{1 + 3\cos(\pi y_f)A_2}{-3\cos(\pi y_f)}\right]\,. \tag{3.52}$$

As A_1 is the amplitude of the limit cycle, the cosine function is substituted with its maximum value of one, to give the following equation.

$$A_1 = \left[\frac{1 + 3\cos(\pi y_f)A_2}{-3\cos(\pi y_f)}\right] . \tag{3.53}$$

Substituting Eqn. (3.53) in (3.51) and rewriting, the following simplification can be done.

$$\begin{aligned} 1 \quad + \quad & 3\cos(\pi y_f)(A_1\cos(\omega(t-\tau)) + A_2) \\ & = 1 + 3\cos(\pi y_f)\left(\left[\frac{1 + 3\cos(\pi y_f)A_2}{-3\cos(\pi y_f)}\right]\cos(\omega(t-\tau)) + A_2\right) \\ & = (1 + 3\cos(\pi y_f)A_2)(1 - \cos(\omega(t-\tau))) . \end{aligned} \tag{3.54}$$

Further, substituting the result of Eqn. (3.54) in the expression for the coefficients given in Eqns. (3.44) to (3.46), the coefficients can be evaluated numerically as given below.

$$C_0 = \frac{2\sqrt{2}}{\pi}\left[1 + 3\cos(\pi y_f)A_2\right]^{1/2}\cos\left(\frac{\omega\tau}{2}\right) , \tag{3.55}$$

$$C_1 = -\frac{4\sqrt{2}}{3\pi}\left[1 + 3\cos(\pi y_f)A_2\right]^{1/2}\cos\left(\frac{\omega\tau}{2}\right) , \tag{3.56}$$

$$C_2 = -\frac{8\sqrt{2}}{3\pi}\left[1 + 3\cos(\pi y_f)A_2\right]^{1/2}\sin\left(\frac{\omega\tau}{2}\right) . \tag{3.57}$$

Equation (3.50) can then be rewritten as given in (3.58), which can further be modified into a second order equation for the unknown as given in (3.59).

$$a_1A_2 + \frac{2\sqrt{2}a_{2p}}{\pi}\Big(1 + 3cos(\pi y_f)A_2\Big)^{1/2}\cos\left(\frac{\omega\tau}{2}\right) - a_{2p} = 0 . \tag{3.58}$$

$$A_2^2 - \left[\frac{2a_{2p}}{a_1} + \frac{24a_{2p}^2\cos(\pi y_f)\cos^2(\frac{\omega\tau}{2})}{\pi^2a_1^2}\right]A_2 + \left[\frac{a_{2p}^2}{a_1^2} - \frac{8\cos^2(\frac{\omega\tau}{2})a_{2p}^2}{\pi^2a_1^2}\right] = 0 . \tag{3.59}$$

Equation (3.59) can be solved to obtain A_2 which can be used to identify the value of the unknown parameter at the fold point. The fold points identified for the simultaneous variation of two system parameters can be plotted as the nonlinear stability boundary. Comparison of the analytically obtained nonlinear stability boundaries with numerical results are shown in Fig. 3.16.

A simplification of the above derivation can be performed by assuming that the offset $A_2 = 0$. The asymptotic state of the periodic solution is then described by only the amplitude A_1 which is simplified from Eqn. 3.53 as given below:

$$A_1 = \frac{1}{-3\cos(\pi y_f)}\,. \tag{3.60}$$

This expression shows that the amplitude at the fold point is independent of the heater power K, damping coefficient c_1 and time lag τ. This result is visible in Figs. 3.4 (b) and 3.5 (b), where the amplitude of limit cycles at the fold points are independent of time lag τ. The amplitude at the fold point is only proportional inversely to the location of the heater y_f.

3.5 Results from numerical continuation

3.5.1 On the effect of the small time lag assumption

The delay differential equations governing the Rijke tube system are linearized about $\tau = 0$ to get ordinary differential equations which are valid for small time lags. The corresponding set of equations in the matrix form $d\chi/dt = B\chi$ is given in Balasubramanian and Sujith (2008*c*). This matrix B can be used to calculate the eigenvalues of the system with small time lag assumption and the value of the parameters when the system becomes unstable can be noted as the stability boundary. This approximate stability boundary is compared with the exact stability boundary predicted by the system of delay differential equations given by Eqns (3.8) and (3.9) in Fig. 3.3.

The linear stability boundaries showing the variation of the critical nondimensional heater power K, damping coefficient c_1 and the heater location y_f with the time lag in the system τ are shown in Figures 3.3(a) to 3.3(c). It can be seen clearly that for all the three cases, the stability boundary predicted with the small time lag assumption does not match very well with the exact stability boundary of the delayed system. The curves approximately match when the time lag τ is very small.

However, the match deteriorates very fast with an increase in the time lag τ. Note

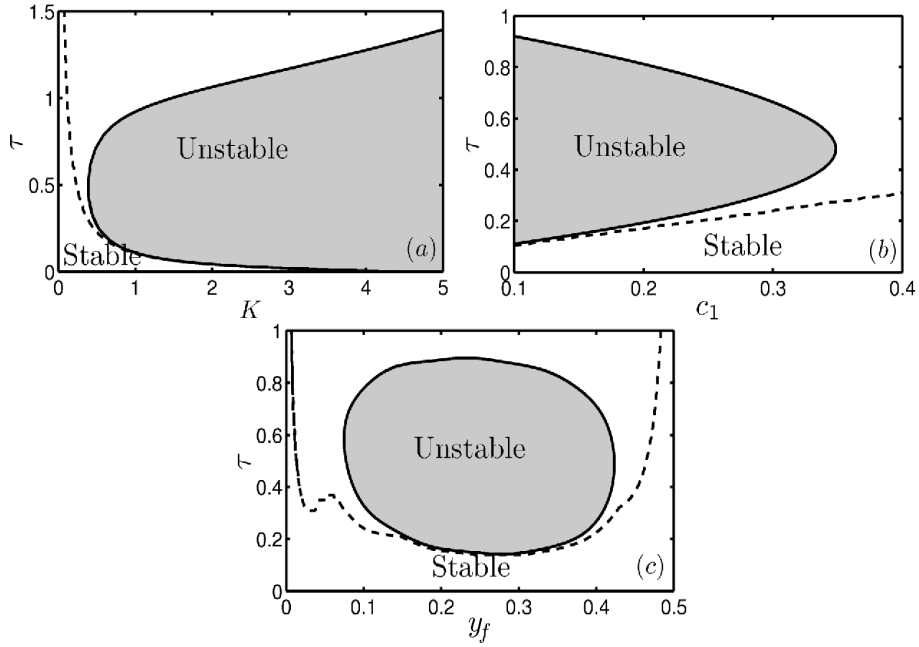

Figure 3.3: Comparison of stability boundary obtained with $- - -$ and without —— the small time lag assumption between (a) non-dimensional heater power K and time lag τ with the other system parameters being $c_1 = 0.1$, $c_2 = 0.06$ and $y_f = 0.3$. (b) damping coefficient c_1 and time lag τ for $c_2 = 0.06$, $K = 1$ and $y_f = 0.3$ (c) location of heater (y_f) and time lag τ with the other system parameters being $c_1 = 0.1$, $c_2 = 0.06$ and $K = 0.8$.

from Fig. 3.3 (b) that the small time lag assumption breaks down even at values of time lag like $\tau = 0.2$. Mass flow rates occuring in experiments can be convereted to time lags using the quasi-steady approximation given by Lighthill (1954). In this relation, the time lag is related to the mass flow rate through the mean flow velocity u_0 as

$$\tau_D = \frac{0.2 d_w}{u_0}. \tag{3.61}$$

The obtained time lag can be non-dimensionalised using the factor c_0/l to obtain τ_{ND} or τ as

$$\tau = \tau_{ND} = \frac{0.2 d_w}{u_0} \left(\frac{c_0}{l} \right). \tag{3.62}$$

Typical flow velocities encountered in experiments (Matveev, 2003b) are in the range $0.05 - 0.27$ m/s, which correspond to τ values between $0.45 - 0.07$ for the experimental configuration described by Matveev (2003b). Hence, it is important to relax the small time lag assumption during the determination of stability in a Rijke tube system.

3.5.2 Effect of heater power

The effect of varying the non-dimensional heater power K on the evolution of the system is analyzed with the bifurcation diagram as shown in Fig. 3.4 (*a*). Nondimensional heater power can be increased by increasing the electrical power supplied to the heater (Matveev, 2003*a*) and it represents an increase in the driving force given to the system. Increased driving strives to destabilize the system. Therefore, for small values of K, the equilibrium is stable and all perturbations decay asymptotically to zero. Increasing K decreases the margin of stability of the flow. At a critical value of K, a pair of complex eigenvalues of the system cross over to the right half plane (Hopf bifurcation) and the system becomes linearly unstable. Linear instability of the system is observed as an oscillating flow pattern in the tube.

The variation of $|\eta_1|$ with K is shown in Fig. 3.4 (*a*). The empty circles indicate unstable solutions and filled circles indicate stable solutions. A limit cycle is first obtained by varying the parameter near the Hopf point and iterating using a Newton's scheme. As discussed earlier, the bifurcation is sub-critical and the resulting small-amplitude limit cycles close to the Hopf point are unstable. These unstable limit cycles are obtained using numerical continuation of the limit cycle and they coexist with the stable equilibrium. This unstable branch of limit cycles further undergoes a fold or turning point bifurcation and gains stability (Ajjarapu, 2006).

The bifurcation diagram for the variation of the non-dimensional heater power is obtained for various values of time lag τ in the interval $[0.2, 0.8]$ and all the results are plotted along with the stability boundary for the system as a 3-D plot in $(\tau, K, |U_1|)$ in Fig. 3.4(*b*). From this 3-D bifurcation diagram, we can also obtain the 2-D bifurcation diagram involving the limit cycle amplitude variation with the time lag τ for a given value of K.

3.5.3 Effect of damping

To study the effect of the variation of the amount of damping present in the system on the response of the system, one of the damping coefficients c_1 of the mode dependent

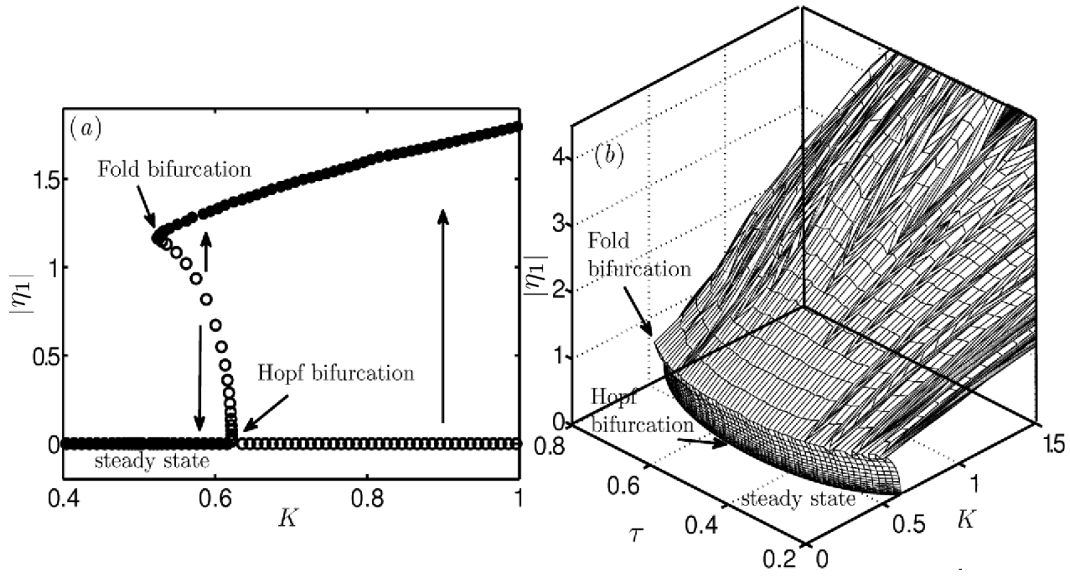

Figure 3.4: (a) Bifurcation plot for variation of non-dimensional heater power K. The other parameter values of the system are $c_1 = 0.1$, $c_2 = 0.06$, $y_f = 0.3$ and $\tau = 0.2$ (b) 3D plot of bifurcation plot of non-dimensional heater power K for varying values of time lag τ with the other parameters of the system $c_1 = 0.1$, $c_2 = 0.06$ and $y_f = 0.3$.

damping model is varied. Change in the damping of the system can be achieved in experiments by changing the end conditions of the duct. As expected, increased damping has a stabilizing effect on the dynamics of the system since the equilibrium is stable for any τ for larger damping coefficients and lowering of damping might lead to instability depending on the time lag τ as shown in Fig. 3.3(b).

For a fixed time lag, there exists a critical value of c_1 below which all perturbations grow to limit cycles and above which there exists a region wherein large amplitude perturbations grow to limit cycles and small perturbations decay to the equilibrium as shown in Fig. 3.5(a). The critical value of the damping coefficient c_1 and the bifurcation diagrams has been obtained for various values of the time lag τ again and the results are plotted as a 3-D plot in Fig. 3.5(b). A 2-D projection of this plot on the (τ, c_1) plane gives us the linear stability boundary (Hopf points also shown in Fig. 3.3(b)) as well as the nonlinear stability boundary (fold points). The region enclosed between them gives us the bistable region to be discussed in more detail in subsequent subsections.

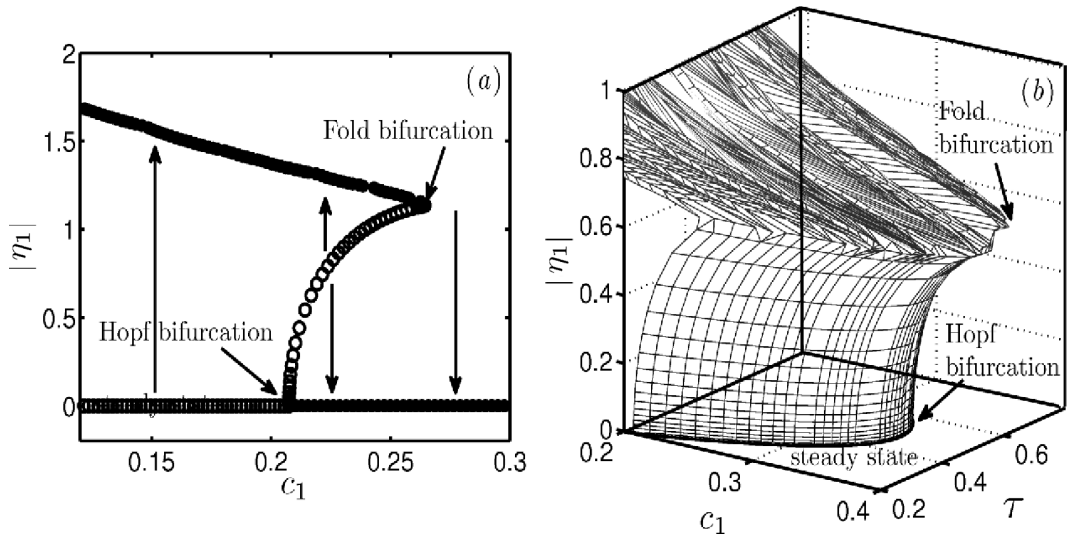

Figure 3.5: (a) Bifurcation plot for variation of damping coefficient c_1. The other parameter values of the system are $c_2 = 0.06$, $K = 1$, $y_f = 0.3$ and $\tau = 0.2$ (b) 3D plot of bifurcation plot of damping coefficient for varying values of time lag τ with the other parameters of the system $c_2 = 0.06$, $K = 1$ and $y_f = 0.3$.

3.5.4 Effect of heater location

The location of the heat source y_f also has a very significant effect on the dynamics of the system. The stability of the system does not change monotonically from stable to unstable or vice-versa with changes to the location of the heater along the duct. When the location of the heater along the duct is varied from the upstream open end, the system is initially linearly stable. At a critical value of the heater location y_{f1}, a pair of complex eigenvalues crosses over to the right half plane and the system becomes linearly unstable. When the heater is located at further locations along the duct, the thermoacoustic system remains linearly unstable till y_{f2}. When the heater is positioned at y_{f2}, the unstable pair of complex eigenvalues cross back into the left half of the complex plane. This Hopf bifurcation causes the system to regain linear stability as also shown in Fig. 3.3(c).

The bifurcation plot for the variation of heater location y_f shows that sub-critical Hopf bifurcations occur at both y_{f1} when the system loses linear stability and at y_{f2}, when the system regains linear stability as seen from Fig. 3.6. The stable branch of limit cycles arising from the turning point bifurcations of the two branches of unstable limit cycles emanating from the Hopf points merge smoothly such that the region of

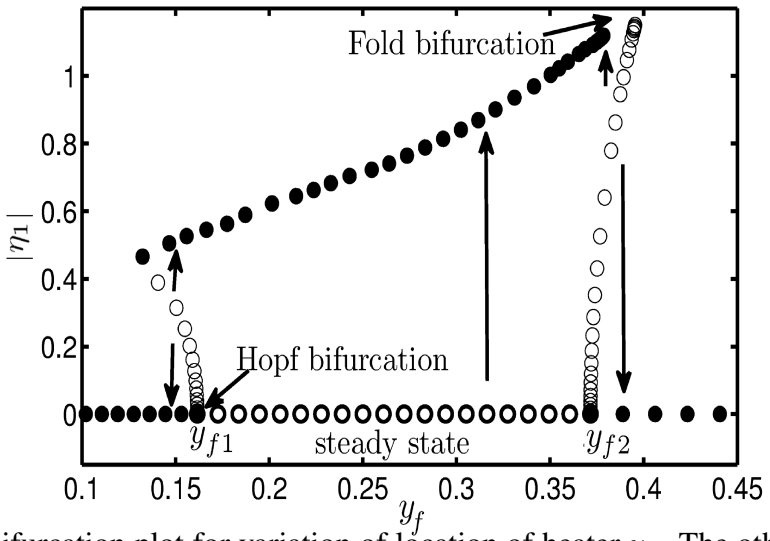

Figure 3.6: Bifurcation plot for variation of location of heater y_f. The other parameter values of the system are $c_1 = 0.1$, $c_2 = 0.06$, $K = 0.8$ and $\tau = 0.2$.

linear instability is completely bounded by a single branch of stable limit cycles. Any initial condition within the linearly unstable region will asymptotically reach the corresponding stable limit cycle. An initial condition within the sub-critical region will either decay asymptotically or reach the corresponding limit cycle based on whether it is above or below the stable manifold of the unstable limit cycles. The amplitude of limit cycle is seen to be a strong function of the location of the heater and is seen to increase with an increase in the heater location from the open upstream condition.

3.5.5 Bistable regions

It can be observed from the bifurcation plots that there are multiple co-existing solutions in the range of the free parameter values between the Hopf point and the fold point. A stable steady state and a pair of stable and unstable limit cycles are seen to co-exist which is a general feature of systems exhibiting sub-critical Hopf bifurcation followed by a fold bifurcation which gives rise to a branch of stable limit cycle solutions. Depending on the initial condition, the system will asymptotically reach a steady state or a limit cycle. This range of parameters has two possible asymptotic states and is hence called the region of bistability. The region of bistability for the variation of non-dimensional heater power and the time lag is shown in Fig. 3.7.

In this figure, the linear stability boundary is the locus of the Hopf points, i.e, points above which an infinitesimal perturbation is sufficient to destabilize the system. Simi-

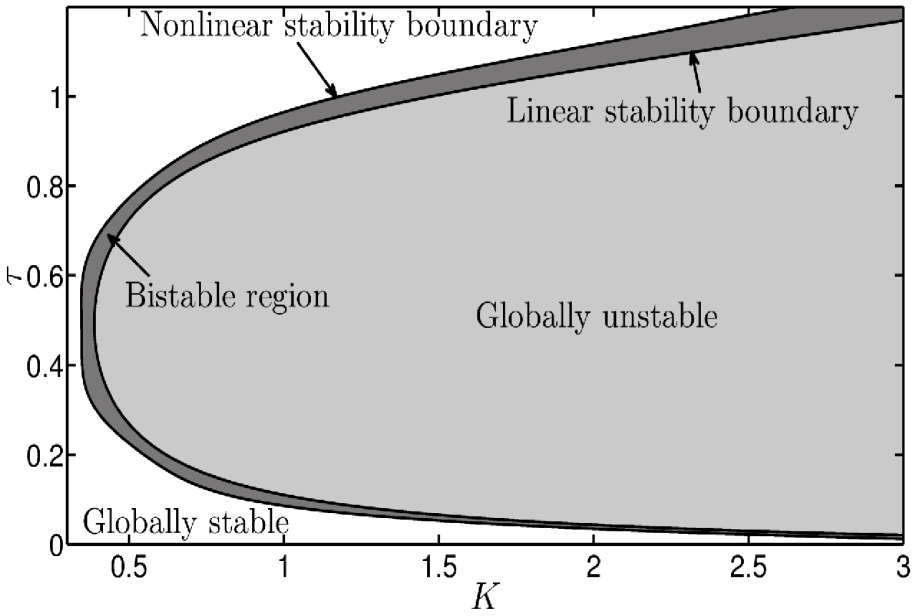

Figure 3.7: Region of bistability obtained for the bifurcation between non-dimensional heater power K and time lag τ with the other system parameters being $c_1 = 0.1$, $c_2 = 0.06$ and $y_f = 0.3$.

larly, the nonlinear stability boundary is the locus of the fold points, i.e., points outside which the steady state is stable to any finite amplitude perturbation. This region outside the nonlinear stability boundary is called the region of global stability (Strogatz, 2000). In the region between the two curves (the bistable region), a finite amplitude perturbation is required to destabilize the system from the unperturbed state. The nonlinear stability boundary can also be called as the 'triggered' or 'pulsed' instability boundary as it marks the beginning of the triggering. Thus the linear and nonlinear stability boundaries divide the parameter plane into three regions. The globally unstable region is shaded with light grey, the region filled with dark grey correspond to region of bistability and the white region represents globally stable region in Fig. 3.7.

Figure 3.8 shows the bistable regions along with the globally stable and unstable regions for variations of the damping coefficient c_1 and the heater location y_f as functions of the time lag τ. It can be seen from Fig. 3.7 that the bistability region is much smaller for small time lags and it increases with an increase in the time lag in the system. Hence, the effect of the nonlinearity introduced by the heating is more profound for larger time lags which roughly corresponds to smaller speeds of mean flow in the tube.

In Fig. 3.8 (*a*), we can observe that the bistable region in the damping coefficient

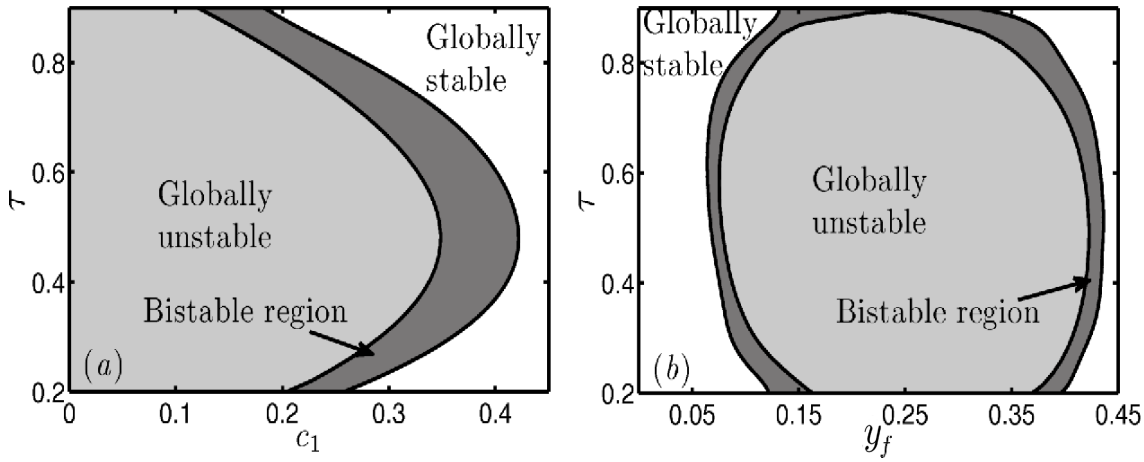

Figure 3.8: Region of bistability obtained for the bifurcation between (*a*) damping coefficient c_1 and time lag τ with the other system parameters being $c_2 = 0.06$, $K = 1$ and $y_f = 0.3$ (*b*) heater location y_f and time lag τ with the other system parameters being $c_1 = 0.1$, $c_2 = 0.06$ and $K = 0.8$.

c_1 first increases with an increase in τ, reaches a maximum value and starts decreasing thereafter. The variation of the extent of the bistable region with the variation of the parameter y_f first decreases with an increase in the time lag τ and increases after reaching a minimum value at a certain critical value of τ as shown in Fig. 3.8 (*b*). The extremum value of the bistable regime typically appears at the parameter value τ at which the other parameter value corresponding to the linear stability boundary reaches an extremum itself.

3.6 Characterizing dynamical behavior through time evolutions

The linear stability boundaries obtained for the simultaneous variation of various parameters with the time lag of the system are given in Fig. 3.3. The variation of the time lag of the system can be obtained in experiments by changing the mean flow rate of air through the duct. However, the most relevant parameters which could be varied in an experiment are the heater location along the duct y_f and the heater power (Matveev, 2003*b*) K. The stability boundary for the simultaneous variation of these two parameters is given in Fig. 3.9.

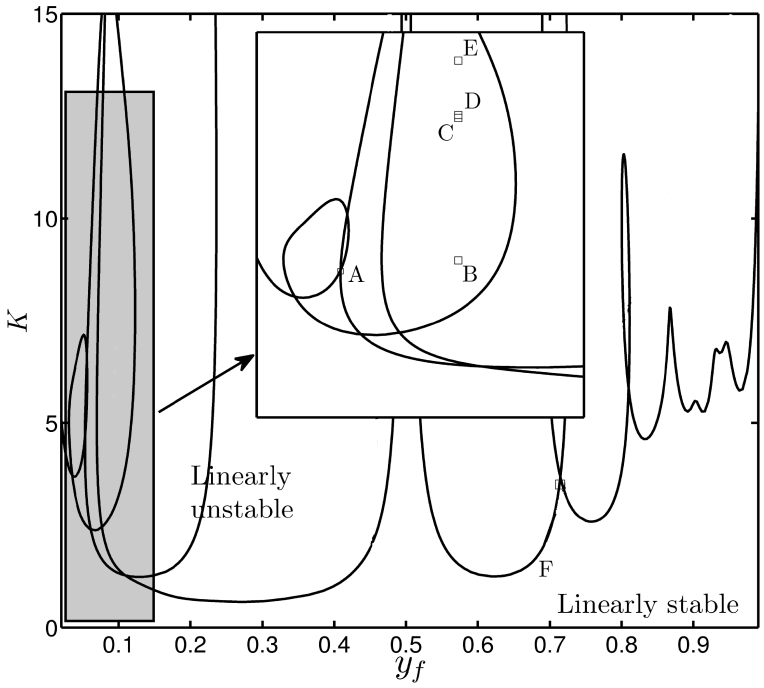

Figure 3.9: Linear stability boundary obtained for location of heater y_f and non-dimensional heater power K with the other system parameters being $c_1 = 0.1$, $c_2 = 0.06$ and $\tau = 0.2$. Time evolutions at points marked from A to F are studied to observe the asymptotic behavior of the system at these parameter values.

This figure shows that the linear stability boundary crosses itself many times to form loops. Along the direction of increasing power for a given heater location, linear stability is lost after the first crossing of the stability boundary. Further crossings lead to other pairs of eigenvalues moving to the right half plane. Accordingly the regions enclosed by the loops in the stability curves have two or more pairs of unstable eigenvalues and hence indicate the occurrence of interesting dynamical behavior in these parameter combinations e.g. points A to F. At these parameter combinations, complicated dynamical behavior such as quasiperiodicity, co-existing multiple attractors, chaos etc. may be observed.

In this subsection we will characterize the dynamical behavior of the system through time evolutions corresponding to some typical points marked A to F in the linearly unstable region of the Fig. 3.9 and its inset. These are chosen to represent more complicated solutions and situations than those already discussed in this work so far.

Shown in Fig. 3.10 (a) is the system evolution for parameters corresponding to the point A. At this point, we see that the system has an asymptotic behavior in which the

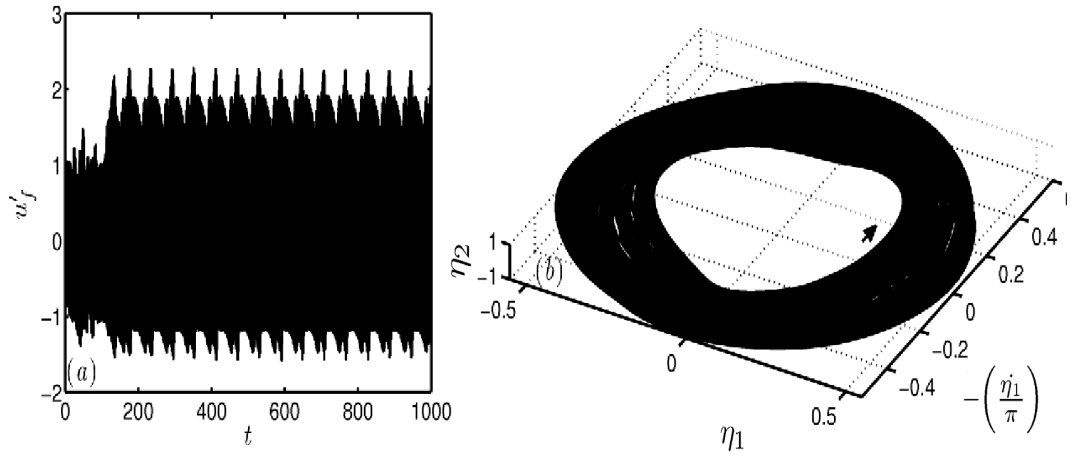

Figure 3.10: Quasiperiodic evolution is seen from the phase plots of system near point A with the system parameters being $c_1 = 0.1$, $c_2 = 0.06$, $K = 4.5$, $y_f = 0.05332$ and $\tau = 0.2$. (a) Time evolution with periodically modulated evolution and (b) Phase plot of evolution from 3.10 (a) showing a quasiperiodic orbit. Arrow indicates direction of evolution of the system.

amplitude of the limit cycle is modulated periodically. This type of regular amplitude modulation of the time series represents a quasiperiodic solution. Figure 3.10(b) shows a 3-D projection of the phase portrait corresponding to the quasiperiodic solution. It can be clearly observed from Fig. 3.10(b) that the trajectory stays on a torus and completely fills out its surface.

We also observe chaotic solutions for our system for specific choice of parameter values. One of the routes to chaos is the period-doubling route to chaos wherein periodic solutions with longer and longer time-periods are observed with a change in some typical parameter till aperiodic solutions appear (Baker and Gollub, 1990). This particular route to chaos is observed as parameters are varied from points B through E. These points are chosen such that they lie in the direction of increasing heater power at a given heater location as shown in Fig. 3.9. The phase plot of the evolution after the loss of linear stability at point B shows a limit cycle as given in Fig. 3.11(a).

Further increase in the nondimensional heater power to point C and D causes limit cycles with periods that are twice and four times the time-period corresponding to point B, respectively. The phase plots of these limit cycles are shown in Figures 3.11(b) and (c) wherein the simple closed curve corresponding to the limit cycle in Fig. 3.11(a) transforms into a closed curve which intersects itself once and twice respectively in this projection. With a sufficient increase in the heater power to point E, the system

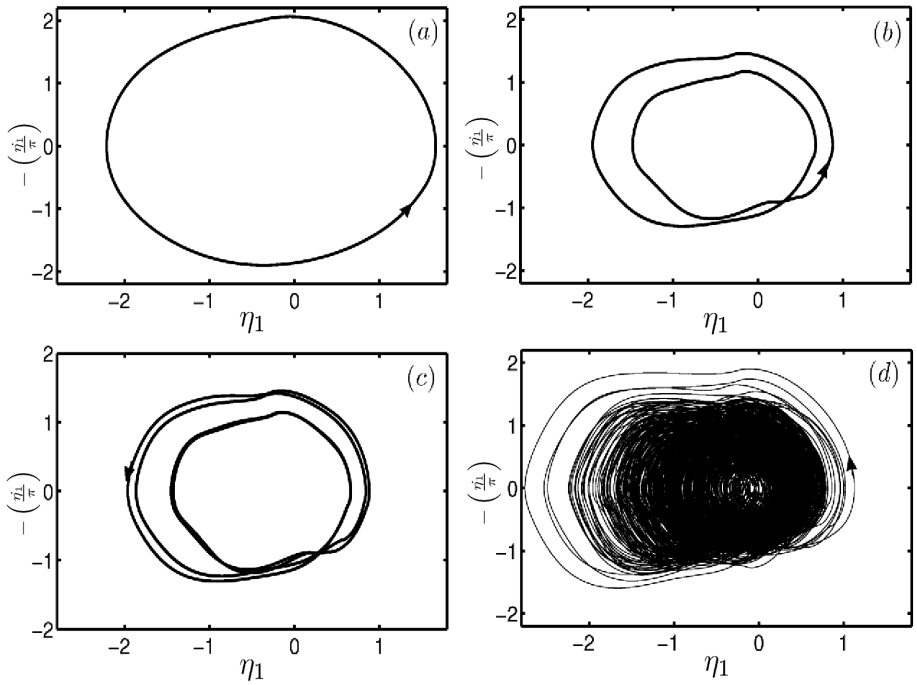

Figure 3.11: Period doubling route to chaos is seen from the phase plots of system at points B through E with the system parameters being $c_1 = 0.1$, $c_2 = 0.06$, $y_f = 0.1$ and $\tau = 0.2$. Arrow heads indicate direction of evolution of system. (*a*) Phase plot at $K = 4$. A limit cycle of period 1 is obtained, (*b*) Phase plot at $K = 10$. A limit cycle of period 2 is obtained, (c) Phase plot at $K = 10.1$. A limit cycle of period 4 is obtained and (*d*) Phase plot at $K = 12$. The phase plot shows no discernable periodic behavior and trajectory moves all over the phase plot.

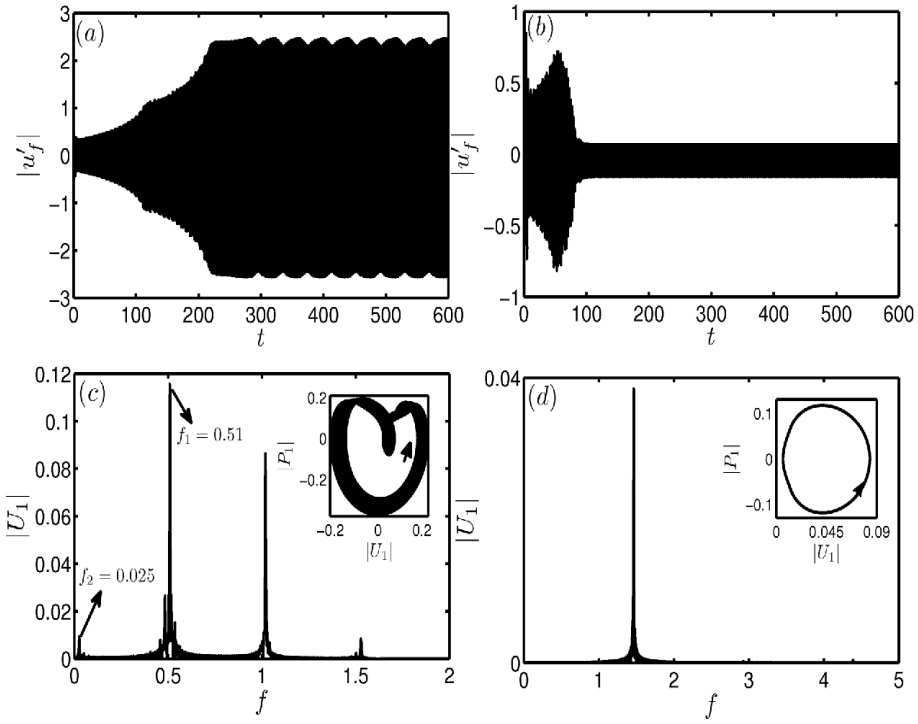

Figure 3.12: Coexisting multiple attractors obtained with different initial conditions at point F from Fig. 10 with the system parameters being $c_1 = 0.1$, $c_2 = 0.06$, $K = 3.5$, $y_f = 0.7141$ and $\tau = 0.2$. (*a*) Time evolution from initial condition $\eta_1 = 1.5$, $\eta_i = 0 \ \forall \ i \neq 1$ and $P_i = 0 \ \forall \ i = 1, ..N$, (*b*) Time evolution from initial condition $\eta_1 = 0.5$, $\eta_i = 0 \ \forall \ i \neq 1$ and $P_i = 0 \ \forall \ i = 1, ..N$, Frequency content of evolution (*c*) from Fig. 11(*a*) and (*d*) from Fig. 11(*a*) with insets showing the phase plot.

evolution becomes highly aperiodic (chaotic), and the trajectory is seen to fill almost an area in the phase space as shown in Fig. 3.11(*d*).

Figure 3.12 shows that the time evolution of the system at point F with two different initial conditions gives two different asymptotic behavior. Time evolution at F with initial condition $\eta_1 = 1.5$, $\eta_i = 0 \ \forall \ i \neq 1$ and $P_i = 0 \ \forall \ i = 1, ..N$ evolves into a complicated quasiperiodic attractor with a large magnitude of the total velocity fluctuation as shown in Fig. 3.12(*a*). The frequency content of this attractor is shown in Fig. 3.12(*c*) wherein the phase space projection of the solution on the first acoustic mode η_1 and $-\left(\frac{\dot{\eta_1}}{\pi}\right)$ is also shown in the inset. The arrow indicates the direction of evolution of the system in the phase plot. A second frequency close to zero is distinctly visible along with the major frequency at around 0.5 and its harmonics.

The time evolution with a different initial condition of $\eta_1 = 0.5$, $\eta_i = 0 \ \forall \ i \neq 1$ and $-\left(\frac{\dot{\eta_i}}{i\pi}\right) = 0 \ \forall \ i = 1, ..N$ however reaches a small amplitude limit cycle where the third

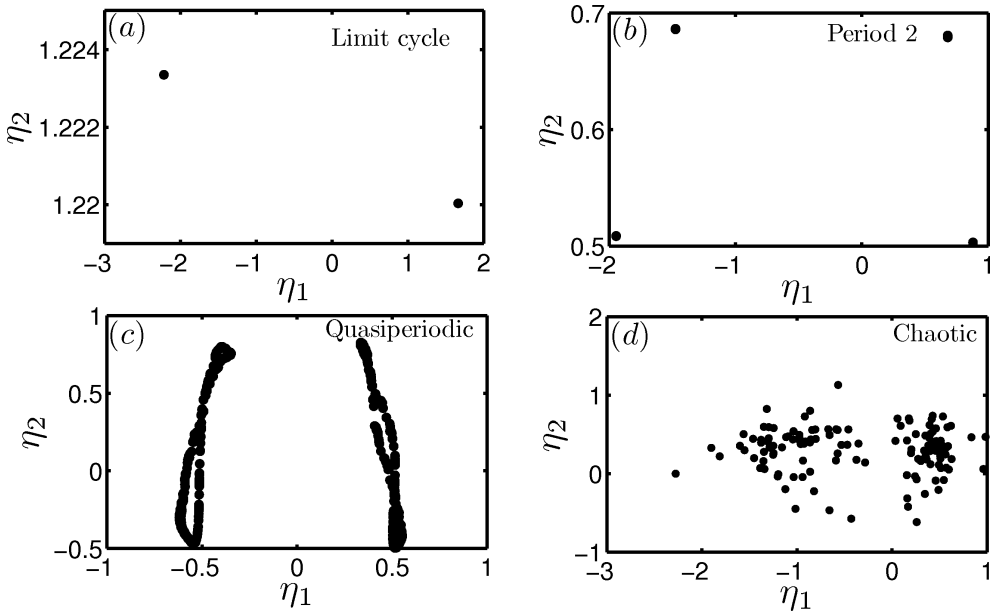

Figure 3.13: Poincare maps for different asymptotic states (a) Limit cycle shown in Fig. 3.11 (a), (b) Period 2 state shown in Fig. 3.11 (b), (c) Quasiperiodic state as shown in Fig. 3.10 and (d) Chaotic orbit as shown in Fig. 3.11 (d).

mode is primarily unstable as shown in Fig. 3.12(b). The frequency content of this limit cycle shown in Fig. 3.12(d) clarifies that the third mode with a fundamental frequency of around 1.5 is unstable. At a given heater power level and heater location, we thus observe the coexistence of two different attractors. One of them is a low amplitude limit cycle and the other is a high amplitude quasiperiodic solution. Thus, a given system can produce two qualitatively as well as quantitatively different oscillations during instability.

Thus, we have seen that for different system configurations, the dynamics of the system model can exhibit complicated dynamical behaviors such as coexisting attractors, quasiperiodicity, complicated limit cycles with increasing time-periods and chaotic solutions. Similar behavior have been observed in experiments: ducted premixed flame (Kabiraj *et al.*, 2010) and laboratory combustor (Sterling and Zukowski, 1991).

The different asymptotic states obtained in Figs. 3.10 to 3.12 were identified using tools from dynamical systems' theory such as the Fast Fourier Transform (FFT) and phase portraits. They can also be identified using Poincare maps as shown in Fig. 3.13. Poincare map of the trajectory plots the trajectory of the system in a phase plane which is perpendicular to the flow of the trajectory (Hillborn, 1994). In the present work,

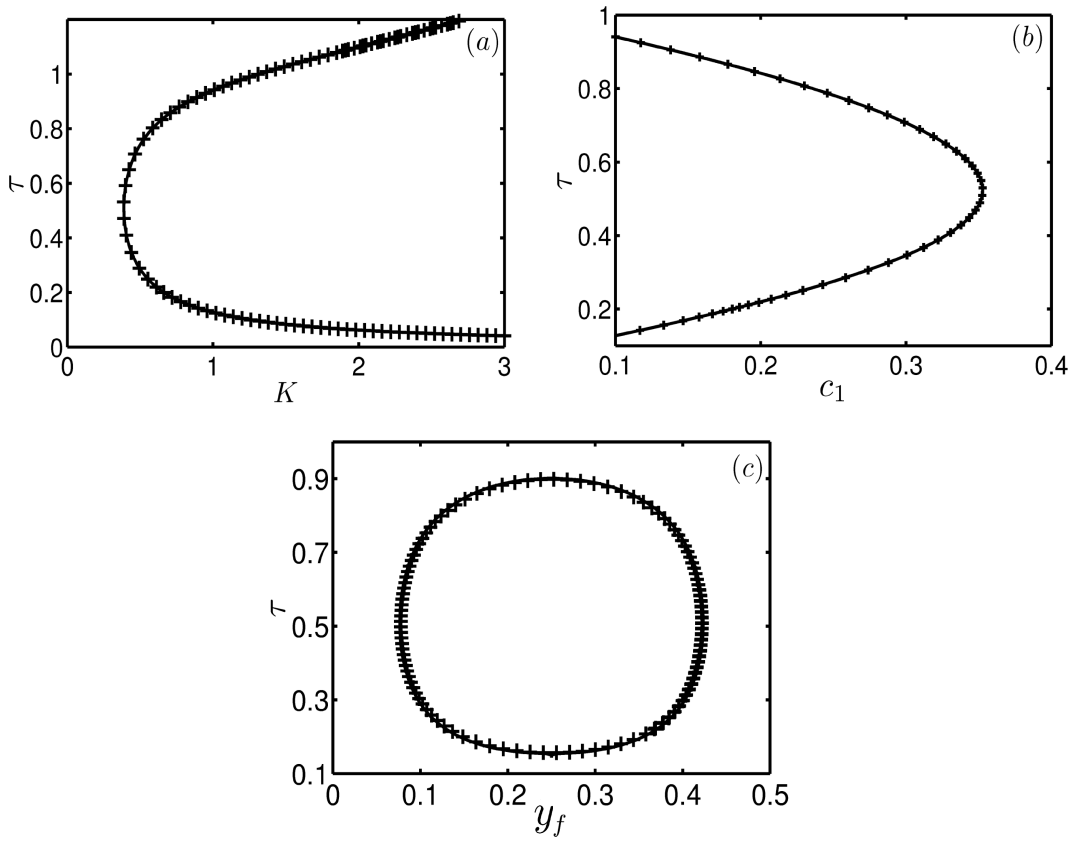

Figure 3.14: Comparison of numerical and analytical linear stability boundary for (a) variation of heater power and time lag, (b) for variation of damping coefficient and time lag and (c) for variation of heater location and time lag. Solid lines are analytical solutions and crosses are numerical solutions. Common parameters are $c_1 = 0.1$, $c_2 = 0.06$, $K = 1$, $y_f = 0.3$ and $\tau = 0.2$.

two sided Poincare sections of the asymptotic state are obtained. When the asymptotic state is a limit cycle, the Poincare section displays two points as shown in Fig. 3.13 (a) while that of a period-2 trajectory shows 4 points in Fig. 3.13 (b). The Poincare map of a quasiperiodic trajectory in Fig. 3.13 (c) shows that sucessive intersections of the trajectory with the Poincare section forms a set of points on the surface of a torus. Chaotic evolutions of the system display a set of points in the Poincare map as shown in Fig. 3.13 (d).

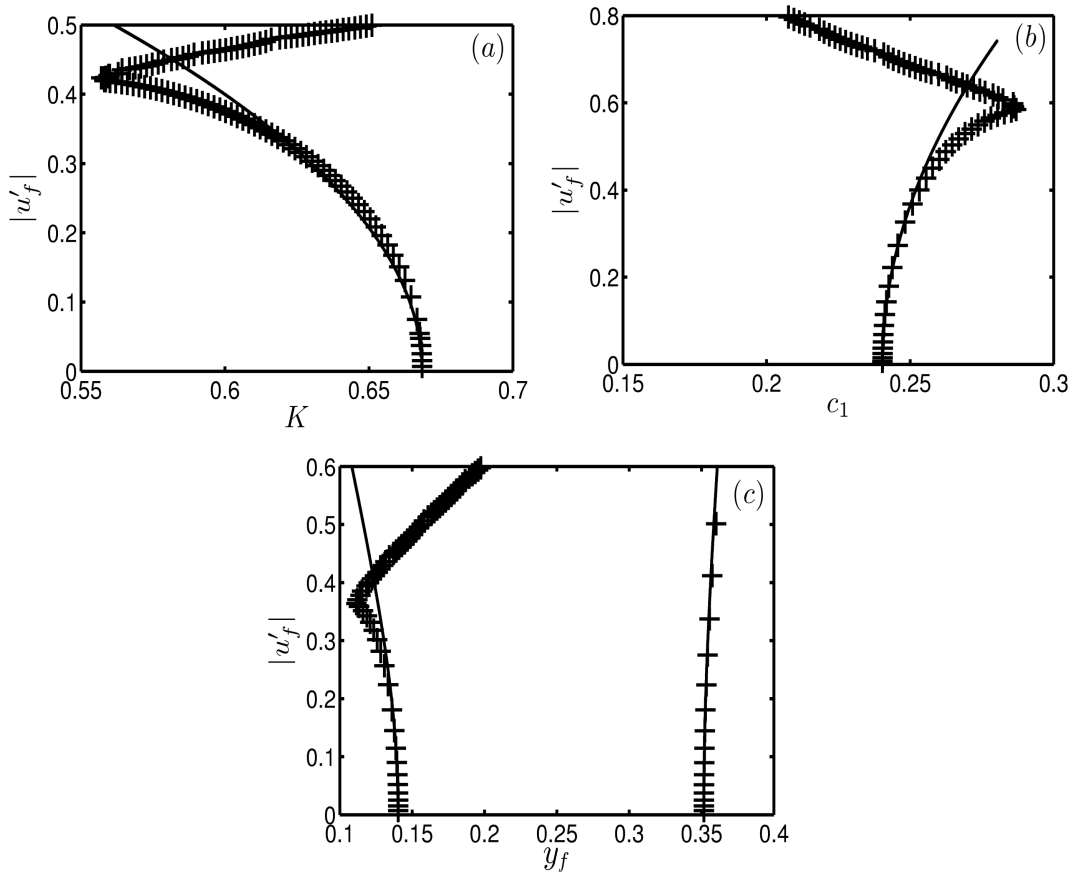

Figure 3.15: Comparison of numerically and analytically obtained limit cycle amplitudes near Hopf point for (a) variation of heater power and time lag (b) for variation of damping coefficient and time lag and (c) for variation of heater location and time lag. Solid lines are analytical solutions and crosses are numerical solutions. Common parameters are $c_1 = 0.1$, $c_2 = 0.06$, $K = 1$, $y_f = 0.3$ and $\tau = 0.2$.

3.7 Comparison with analytical estimates

The linear stability boundary can be obtained analytically as detailed in Section 3.4.1. Linear stability boundaries for the simultaneous variation of the non-dimensional heater power K, damping coefficient c_1, heater location y_f and time lag τ are determined. Figure 3.14 shows the comparison of the linear stability boundaries obtained from numerical continuation in crosses and the analytical solution in solid lines. It is seen that analytical method predicts the linear stability boundary well in all the three different cases.

The amplitude and stability of the limit cycles near the Hopf point is obtained from the slow-flow amplitude equation as derived in Section 3.4.2 using the method of mul-

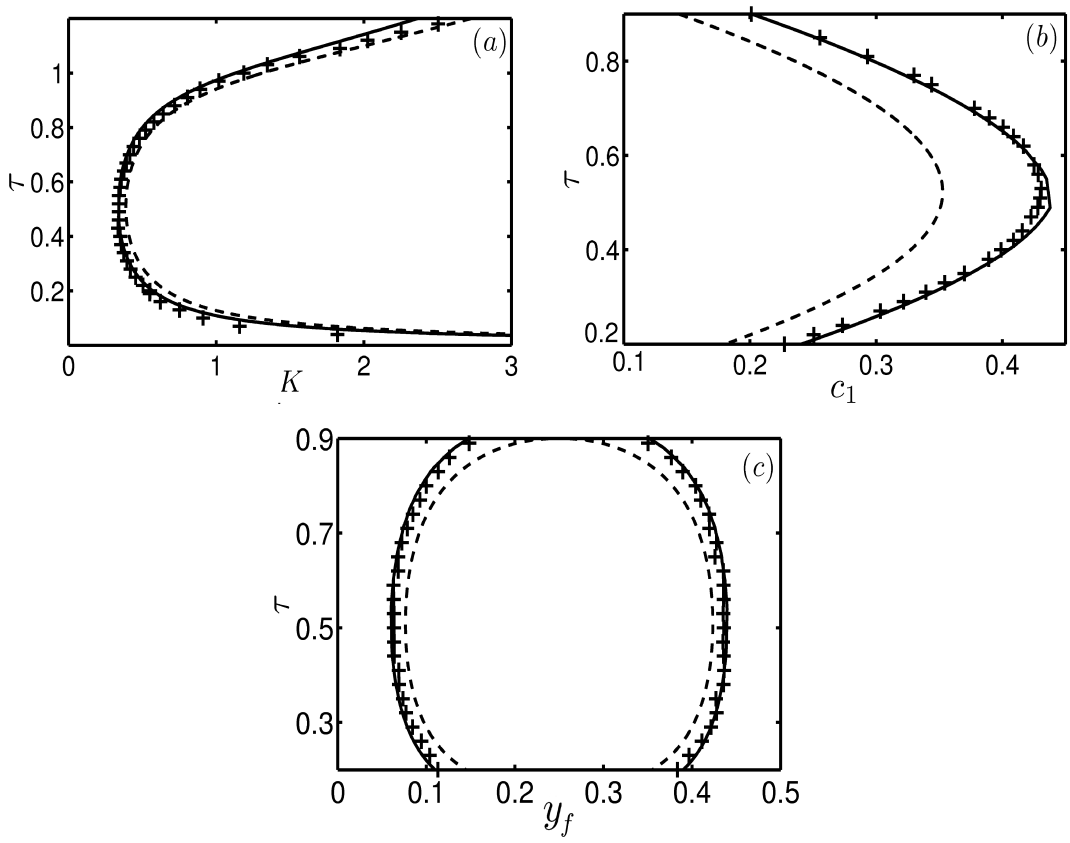

Figure 3.16: Comparison of numerical and analytical linear stability boundary for (a) variation of heater power and time lag (b) for variation of damping coefficient and time lag and (c) for variation of heater location and time lag. Solid lines are analytical solutions and crosses are numerical solutions. Common parameters are $c_1 = 0.1$, $c_2 = 0.06$, $K = 1$, $y_f = 0.3$ and $\tau = 0.2$.

tiple scales. It is seen from Fig. 3.15 that the amplitudes of the limit cycles as predicted by the method of multiple scales matches well with those calculated from numerical continuation near the Hopf point. The match in the comparison of the limit cycle amplitudes is seen to deteriorate when the system is away from the Hopf point. This deterioration is a result of the assumption given in (3.27), which states that the change in the value of the parameter from its critical value is small.

The determination of fold point by harmonic balance identifies the region of bistability analytically. Numerically, a fold point is identified from the bifurcation plot as the point where the limit cycles gain stability. Comparison of the analytically obtained fold points are plotted against numerical results in Fig. 3.16. The analytical results for the fold point match well with the numerical results. The above comparisons show that analytical approaches can be used to estimate bifurcation plots.

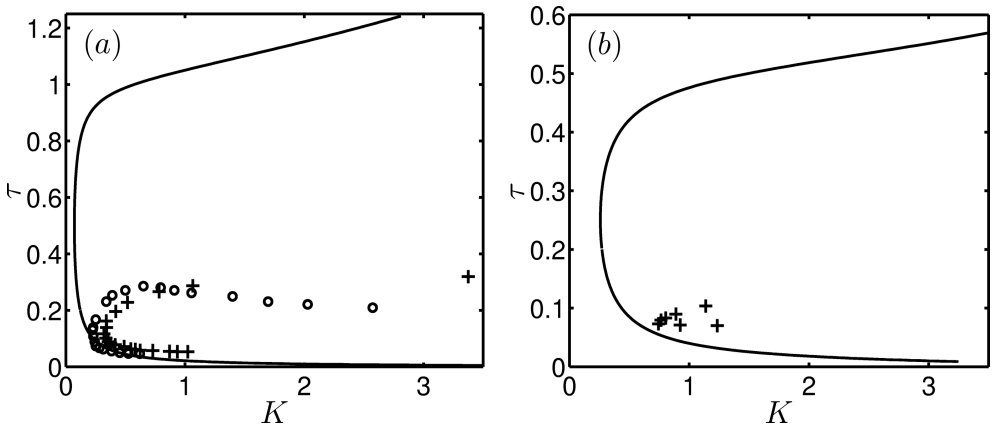

Figure 3.17: Comparison of linear stability boundary between numerical (——) and experimental data from Matveev and Culick (2003) (+++) and Song *et al.* (2006) ($\circ$ $\circ$ $\circ$) for the simultaneous variation of non-dimensional power (K) and time lag (τ) when the heater location is (a) $y_f = 1/4$ and (b) $y_f = 5/8$. The other system parameters are $c_1 = 0.028$, $c_2 = 0.0001$.

3.8 Comparison with experimental results

Matveev (2003*b*) obtained the stability boundaries for a horizontal Rijke tube and also reported hysteresis at the stability boundary. Song *et al.* (2006) also obtained linear stability boundary of a horizontal Rijke tube and matched their results with Matveev and Culick (2003). In both the papers, the linear stability boundaries were obtained for the simultaneous variation of power supplied to the heater P (in Watts) and mass flow rate $\dot{m}$ (in gm/sec) at different locations along the Rijke tube.

Changes in the power supplied to the heater P, causes variation of the temperature of the heater T_w. Increasing P increases the temperature of the wire and affects K. Changes in the mass flow rate $\dot{m}$ affect K by changing the mean flow velocity u_0 through the Rijke tube. The non-dimensional heater power K and the mean flow velocity u_0 are related as given in Eqn. 3.11. This relation can be rewritten as below by replacing the product of Mach number M and c_0 to give u_0 in the denominator.

$$K = \frac{4(\gamma-1)L_w}{\gamma u_0 \bar{p} S\sqrt{3}}(T_w - \bar{T})\sqrt{\pi\lambda C_V u_0 \bar{\rho} l_c}\,. \tag{3.63}$$

Therefore, increasing $\dot{m}$ increases u_0 and decreases K. The effect of changing mass flow rate affects both the non-dimensional power K and the time lag τ through changes in the mean velocity. Variation in K occurs according to the Eqn. (3.63) while time

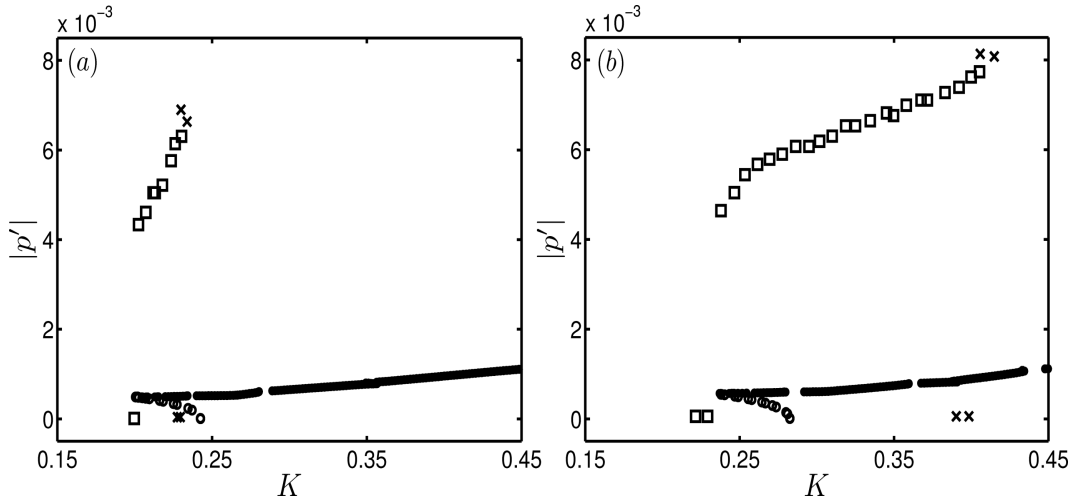

Figure 3.18: Comparison of bifurcation plot for the variation of non-dimensional heater power K between numerical models and experiment. $\circ$ are the unstable limit cycles and $\bullet$ are the stable limit cycles predicted by the current model for (a) $\tau = 0.08$ or $\dot{m} = 2.75$ gm/sec and (b) $\tau = 0.07$ or $\dot{m} = 3.15$ gm/sec. $\times$ are experimental data points obtained when power was increased and $\square$ are data points obtained when power was reduced for $c_1 = 0.028$, $c_2 = 0.0001$ and $y_f = 0.25$.

lag is related to the mean velocity through the quasi-steady approximation given by Lighthill (1954).

$$\tau_D = \frac{0.2 d_w}{u_0}. \tag{3.64}$$

The time lag obtained can be non-dimensionalised with the acoustic time scale l/c_0 to obtain the non-dimensional time lag as $\tau_{ND} = \tau$ as given below:

$$\tau_{ND} = \tau = \frac{0.2 d_w}{u_0} \left(\frac{c_0}{l} \right). \tag{3.65}$$

Damping coefficients, c_1 and c_2 are calculated using the formula given in Matveev and Culick (2003). The stability boundaries obtained at two different heater locations from Matveev's experiments are shown by the symbol '+' in Fig. 3.17. The corresponding numerical results from the present study are denoted with solid lines in the same figure. Figure 3.17 (a) is the linear stability boundary when the heater is placed at one-quarter of the duct length. At this location, the frequency close to the fundamental mode of the duct becomes unstable. Figure 3.17 (b) shows the linear stability boundary when the heater is placed at $5/8^{th}$ of the duct length where the frequency close to the second mode of the duct becomes unstable. In both the cases the linear stability boundary predicted

has the same trend as the experimental observations.

Matveev (2003*b*) also reported hysteresis at the stability boundary for different mass flow rates. Results obtained from his experiments are shown using the symbols '$\times$' and '$\square$' in Figs. 3.18 $(a-b)$. In order for comparison with experimental data, the measure chosen in the bifurcation plots is $|p'|$, the amplitude of the acoustic pressure. In the plot, '$\times$' indicate values acquired during increase of power and '$\square$' correspond to data for the decrease in power. The numerically calculated bifurcation plots for the same system parameters are compared with the experimental data for two different mass flow rates. In both the cases, the limit cycle amplitudes predicted are much lower than the observed values.

The under prediction of limit cycle amplitudes can be attributed to the following reasons. A mesh type electrical heater is used in experiments (Matveev, 2003*b*) while the present model assumes the flow over a single cylinder. However, the heat transfer characteristics of a single cylinder is significantly different from that of a mesh (Sen *et al.*, 2009). A constant speed of sound is assumed throughout the tube in the present model. However, the presence of the heater causes a higher downstream temperature. This effect could have a noticeable effect on linear stability and oscillation amplitude by modifying the eigenfrequencies and mode shapes. Also, the present model assumes significant nonlinear effects when the amplitude of the velocity fluctuations exceed one-third of the steady state velocity. However, recent results for the nonlinear system identification of pulsatile flow over a cylinder (Selimefendigil *et al.*, 2010) show that the effect of nonlinearity in the heat release rate response occurs only when the perturbation velocities exceed 1.5 times the steady state velocity. Due to the above reasons, the limit cycle amplitudes predicted by Heckl's correlation are lower than experimental results.

The numerically predicted fold points are close to the experimental results while the Hopf point is over predicted in Fig. 3.18 (a) and under predicted in Fig. 3.18 (b). This shift in the Hopf point may be due to the presence of inherent noise in actual experiments. Uncertainties in the parameters is seen to affect the bifurcation plot (Nair *et al.*) while noise in the initial perturbation can cause sub-critical transition to instability (Waugh *et al.*, 2010) in the present Rijke tube model. A factor which possibly

contributes to the mismatch is related to the uncertainties in the values of steady state parameters. The value of the damping coefficients (c_1 & c_2) used are currently calculated from the cold flow conditions (Matveev, 2003*a*). However, these values could be different when the heater is turned on. Further investigations are required to determine the variation of the damping coefficients with temperature.

Another reason for the mismatch of the present model could be the use of a single time lag to obtain the response of the heater to velocity perturbations. Other investigations of the Rijke tube model which include multiple time lags (Selimefendigil and Polifke, 2010) exhibit higher limit cycle amplitudes. It is observed that in the present study that even with simplifying assumptions, this model is seen to predict the trends in the linear stability boundaries and the bifurcation plot of a Rijke tube which are reasonably close to the experimental results.

3.9 Summary

The dynamical behavior of a model for a horizontal Rijke tube has been studied using analytical and numerical methods. Linear stability boundaries for the simultaneous variation of two parameters of the system are obtained. The nature of the Hopf bifurcation along with estimates of the stability and amplitude of periodic states near the Hopf point are obtained using the method of multiple scales. It is seen that only sub-critical Hopf bifurcations are possible for the model considered to represent the behavior of the Rijke tube. Estimates for the Fold bifurcation points are obtained by employing the method of harmonic balance while the Hopf bifurcation points are obtained via the classical eigenvalue analysis.

The nonlinear stability boundary and the regions of bistability where the system can reach one or two possible asymptotic states are also obtained numerically. Using the linear and nonlinear stability boundaries, regions of global stability, global instability and regions of potential instability are identified. Interesting dynamical behavior such as co-existing limit cycles, quasiperiodic behavior and period doubling route to chaos are observed. Good agreement has been obtained between the results obtained from the

analytical methods in this work with results from numerical continuation.

Linear stability boundaries and bifurcation plots obtained from numerical continuation are compared with experimental data. Trends of the numerically obtained linear stability boundaries are similar to experimental results. However, the numerical model under predicts the amplitude of the stable limit cycles observed in experiments.

In summary, reduced order models of physical systems with explicit time delays were studied in detail using analytical and numerical continuation methods to identify stability boundaries, to obtain bifurcation plots and to examine their possible dynamical behavior. This method of numerical continuation can be used in future for bifurcation analysis of practical combustors to identify safe ranges of operation.

CHAPTER 4

LINEAR & NONLINEAR ANALYSIS OF THERMOACOUSTIC INSTABILITY IN A DUCTED PREMIXED FLAME

4.1 Kinematic model of a ducted premixed flame

A model for the premixed flame can be obtained using a kinematic approach to track the evolution of the flame. In this model, fluctuations in the surface area of the flame are correlated with heat-release rate oscillations. Dowling (1999) used the front-tracking equation to model the evolution of a premixed flame in the investigation of the thermoacoustic instability in a ducted premixed flame. The use of an evolution equation to describe the premixed flame includes the transient effects; hence this approach is adopted in the present investigation. A low Mach number laminar inviscid flow is assumed and all reaction parameters are frozen by assuming a constant value for the laminar flame speed. An axi-symmetric wedge flame is modeled as a kinematic flame front which separates the unburnt mixture and the products of combustion (Kerstein *et al.*, 1988). The equations for the acoustic field are evolved together with the flame front-tracking equation to model the thermoacoustic system.

Balasubramanian and Sujith (2008*a*) demonstrated that the presence of a fluctuating heat source renders the resulting thermoacoustic system non-normal. Non-normal systems have non-orthogonal eigenvectors and can exhibit transient growth even in a linearly stable system (Schmid and Henningson, 2001). Two possible routes to triggering, have been demonstrated for thermoacoustic systems such as Rijke tube system (Balasubramanian and Sujith, 2008*a*,*c*; Mariappan and Sujith, 2010*b*). The first route is when a linearly stable system becomes unstable for a large amplitude initial condition. The other route for sub-critical transition to instability is from a small but finite amplitude which causes non-normal transient growth.

The amount of transient growth is quantified using the disturbance energy of the system. Disturbance energy is the energy associated with fluctuations that are superimposed over a base flow. Therefore, it should account for contributions from all the constituent phenomena in the system. Kinetic energy was chosen as the natural measure to describe transient growth due to non-normality for incompressible fluid flows (Schmid and Henningson, 2001). However, there has been no such consensus on the appropriate expression for disturbance energy for compressible reacting flows. Previously, many expressions for the energy of a small disturbance in a viscous compressible flow have been derived which include the energy due to entropy fluctuations (Chu, 1964) or the energy due to fluctuations in species concentrations (Giaque *et al.*, 2006) as discussed in detail in Chapter 1. There is a need therefore to identify a measure which quantifies the disturbance energy in premixed flame-acoustic interaction.

The premixed flame front is modeled as a distribution of acoustic monopole sources (Morse and Ingard, 1968; Dowling and Williams, 1983) and the dilatation due to unsteady heat release rate is added to the acoustic energy to obtain the energy due to fluctuations. This total energy is used to quantify the transient growth due to non-normality. We investigate the effect of system parameters such as flame location and flame angle on transient growth. We also examine the possibility of sub-critical transition to instability from a small yet finite amplitude initial condition.

The evolution equations for a ducted premixed flame, form a set of parameterized nonlinear ordinary differential equations. In this chapter, the parameters chosen to investigate stability boundaries and bifurcation plots of the system are the damping coefficient c_1, the heater location y_f, the angle of the flame α, the burner to duct ratio b/a and the equivalence ratio ϕ. Bounds of linear stability are obtained for the simultaneous variation of two system parameters using classical linear stability analysis. Bifurcation plots for the variation of system parameters such as damping coefficient c_1 and the mean flow velocity $\bar{u}$ are obtained by the method of numerical continuation.

The organization of the rest of the chapter is as follows. In Section 4.2 the *G*-equation governing the premixed flame model is discussed. Section 4.3 explains the governing equations for the acoustic field within the duct. Section 4.4 explains the modeling of the flame front in terms of a distribution of acoustic monopole sources. An

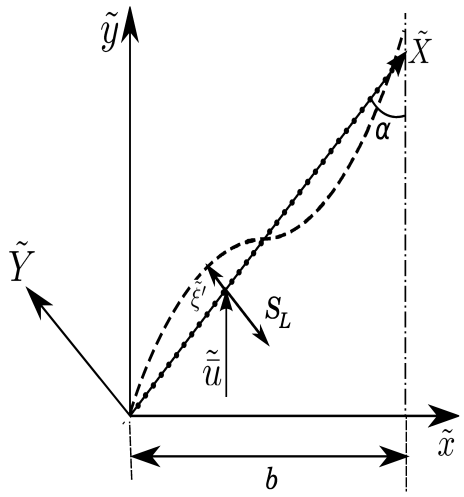

Figure 4.1: Geometry of an axi-symmetric wedge flame stabilized on a wire. Here $\tilde{\xi}'$ is the displacement of the instantaneous flame shape from the unperturbed flame shape, α is the flame angle, S_L is the laminar flame speed and $\tilde{\bar{u}}$ is the mean flow.

expression for the total energy due to fluctuations in a premixed flame-acoustic system is derived in Section 1.5. The equations governing the linear and nonlinear evolutions are derived in Section 4.6. Sections 4.7 through 4.10 discuss the significant results while Section 4.14 summarizes the important conclusions.

4.2 Combustion model

The laminar premixed flame is modeled as a thin wrinkled interface which separates the unburnt mixture from the burnt products of combustion (Kerstein *et al.*, 1988). In this kinematic approach, the governing differential equation for the dynamics of premixed flame is given by the *G*-equation. The scalar variable *G* can be related to the signed distance of the flame front from its unperturbed location $\tilde{\xi}'(\tilde{X})$ along the direction Y as shown in Fig. 4.1. The flame is along the axes $(\tilde{X}, \tilde{Y})$ stabilized in a duct with purely axial velocity $\tilde{u}$ along $\tilde{y}$ in the $(\tilde{x}, \tilde{y})$ co-ordinate axes. The two co-ordinate systems are related by the following transformations where α is the angle which the unperturbed flame makes with the flow.

$$\tilde{x} = \tilde{X}\sin\alpha - \tilde{\xi}'\cos\alpha \text{ and } \tilde{y} = \tilde{X}\cos\alpha + \tilde{\xi}'\sin\alpha\,. \tag{4.1}$$

Both the co-ordinates axes are retained, since even when the acoustic field in the duct is along $(\tilde{x}, \tilde{y})$ axis, the flame front is linearized about the $(\tilde{X}, \tilde{Y})$ axis. Using the above transformations and decomposing the axial velocity into its mean and perturbed values, the *G*-equation for the flame front can be rewritten as the front-tracking equation (Fleifil *et al.*, 1996). For the geometry of an axi-symmetric wedge flame stabilized on a wire adapted from Schuller *et al.* (2003), the front tracking equation in the flame fixed co-ordinate axes is as below:

$$\frac{\partial \tilde{\xi}'}{\partial \tilde{t}} + (\tilde{\bar{u}} + \tilde{u}')\cos\alpha \frac{\partial \tilde{\xi}'}{\partial \tilde{X}} - (\tilde{\bar{u}} + \tilde{u}')\sin\alpha = -\tilde{S}_L \sqrt{1 + \left(\frac{\partial \tilde{\xi}'}{\partial \tilde{X}}\right)^2}\,. \tag{4.2}$$

Here the tildes denote dimensional values and primes indicate fluctuating quantities. Also, $(\tilde{\bar{u}} + \tilde{u}')\cos\alpha$ is the component of axial velocity parallel to the flame front, $(\tilde{\bar{u}} + \tilde{u}')\sin\alpha$ is the component of axial velocity perpendicular to the flame front and S_L is the laminar flame speed.

The effect of all reaction parameters is distilled into the laminar flame speed, which is considered to be only a function of the equivalence ratio of the unburnt mixture. A methane-air flame is considered and for a given equivalence ratio ϕ the laminar flame speed S_L is obtained using the following relation where $J = 0.6079\ m/s$ (You *et al.*, 2005):

$$S_L(\phi) = J\big(\phi^{-2.554} exp\left[-7.31(\phi - 1.23)^2\right]\big)\,. \tag{4.3}$$

Equation (4.2) is nonlinear and describes the combustion response of a premixed flame when subjected to a velocity perturbation. Linearising the equation, we obtain

$$\frac{\partial \tilde{\xi}'}{\partial \tilde{t}} = \tilde{u}'\sin\alpha - \tilde{\bar{u}}\cos\alpha \frac{\partial \tilde{\xi}'}{\partial \tilde{X}}\,. \tag{4.4}$$

The length scale used for non-dimensionalisation is the length of the flame $b/\sin\alpha$, where b is the radius of the burner. The velocity scale chosen is the mean velocity of the flow $\bar{u}$. The time scale for non-dimensionalisation is derived from the length and velocity scales as shown below in Eqn. (4.5) to derive the non-dimensional time in the

combustion scale t_c.

$$y = \tilde{y}\sin\alpha/b;\ \bar{u} = \tilde{\bar{u}}/\tilde{\bar{u}} = 1;\ t_c = \tilde{t}/(b/\bar{u}\sin\alpha)\,, \tag{4.5}$$

The non-dimensional linear (4.6) and nonlinear (4.7) front tracking equations are obtained as given below:

$$\frac{\partial \xi'}{\partial t_c} = u'\sin\alpha - \cos\alpha\left(\frac{\partial \xi'}{\partial X}\right)\,, \tag{4.6}$$

$$\frac{\partial \xi'}{\partial t_c} = (1+u')\sin\alpha - (1+u')\cos\alpha\left(\frac{\partial \xi'}{\partial X}\right) - \sin\alpha\sqrt{1+\left(\frac{\partial \xi'}{\partial X}\right)^2}\,. \tag{4.7}$$

The above equations are first order in time and space and therefore require an initial condition and a boundary condition for their solution. The flame is assumed to be anchored at the base and the other end is left free to move. The resulting system can be evolved from a prescribed initial condition using a numerical integration scheme.

The shape function $\xi'(X,t)$ is smooth for small amplitude perturbations in the linear regime. Therefore in the linear regime, the gradient term is expanded using a first order backward difference formula. However the shape function $\xi'(X,t)$ can become significantly distorted and can even display a discontinuity in slope at high perturbation amplitudes (Dowling, 1999). Therefore, it becomes necessary to calculate the spatial derivative of the shape function to high accuracy using a high resolution method. The high resolution scheme used to capture the highly oscillatory solution of the *G*-equation is the weighted essentially non-oscillatory (WENO) scheme of the third order (Schuller *et al.*, 2003; Jiang and Shu, 1996). The implementation details of the WENO scheme are given in Appendix C. The above formulation enables us to achieve fifth order accuracy in smooth regions and third order accuracy in the discontinuous regions for the spatial derivative of the flame shape.

The flame front area is calculated for the geometry of the flame front from its instantaneous position given by the nonlinear and linearized equations. For the geometry of an axi-symmetric wedge flame stabilized on a wire, as given in Fig. 4.1, the flame shape at the unperturbed state can be approximated by an inverted cone. The nonlinear and

linear expressions for total surface area of perturbed flame front are given as follows:

$$A(t_c) = 2\pi \int_{X=0}^{X=1} (X \sin\alpha - \xi' \cos\alpha)\sqrt{1 + \left(\frac{\partial \xi'}{\partial X}\right)^2}\, dX\,, \tag{4.8}$$

$$A(t_c) = 2\pi \int_{X=0}^{X=1} (X \sin\alpha - \xi' \cos\alpha) dX\,. \tag{4.9}$$

The linear relation for the change in the surface area of the flame due to change in the flame shape is obtained with the relation (4.9). Dimensionally, this relation can be written as

$$\tilde{A}(t_c) = \frac{2\pi b^2}{\sin^2\alpha} \int_{X=0}^{X=1} (X \sin\alpha - \xi' \cos\alpha) dX\,. \tag{4.10}$$

The unperturbed flame shape is obtained from the above relation when $\xi' = 0$ such that the dimensional surface area of the unperturbed flame $\tilde{\bar{A}}(t_c)$ is given by the following expression:

$$\tilde{\bar{A}}(t_c) = \frac{2\pi b^2}{\sin^2\alpha} \int_{X=0}^{X=1} X \sin\alpha dX = \frac{\pi b^2}{\sin\alpha}\,. \tag{4.11}$$

Retaining the expression with the integral and subtracting it from the expression for the total surface area of the flame given in Eqn. (4.10), we obtain the linear expression for the fluctuating surface area as

$$\tilde{A}'(t_c) = \frac{-2\pi b^2 \cos\alpha}{\sin^2\alpha} \int_{X=0}^{X=1} \xi' dX\,. \tag{4.12}$$

Following the kinematic flame model of Fleifil *et al.* (1996) with constant flame speed and no equivalence ratio fluctuations, the evolution of heat release fluctuations imitates the evolution of the area ratio such that $\dot{\tilde{q}}'/\dot{\tilde{\bar{q}}} = \tilde{A}'/\tilde{\bar{A}}$, or as given below:

$$\dot{\tilde{q}} = \dot{\tilde{\bar{q}}} + \dot{\tilde{q}}' = \rho_0 S_L \Delta q_R (\tilde{\bar{A}} + \tilde{A}')\,. \tag{4.13}$$

Here, ρ_0 is the density of the unburnt mixture in kg/m^3. At a given equivalence ratio ϕ, $S_L(\phi)$ is the laminar flame speed measured in m/s and $\triangle q_R(\phi)$ is the heat released per unit mass of the mixture measured in J/kg. The values of S_L and $\triangle q_R$ are obtained for

a methane-air mixture from You *et al.* (2005) as given below.

$$\Delta q_R(\phi) = \begin{cases} \frac{2.9125\times10^6\phi}{1+0.05825\phi}, \phi \leq 1 \\ \frac{2.9125\times10^6}{1+0.05825\phi}, \phi > 1 \end{cases} , \mathrm{J/kg}. \tag{4.14}$$

The fluctuating part of dimensional heat release rate can be calculated from the fluctuating surface area using the relation given in Eqn. (4.13) for a specified equivalence ratio. Thus,

$$\dot{\tilde{q}}' = \rho_0 S_L \Delta q_R \tilde{A}'(t) = \frac{-2\pi\cos\alpha\ \rho_0 S_L \Delta q_R b^2}{\sin^2\alpha} \int_{X=0}^{X=1} \xi' dX', . \tag{4.15}$$

4.3 Model for the coupled thermoacoustic system

The coupled thermoacoustic system considered is as given in Fig. 4.2. It consists of the acoustic field within a duct open at both ends and a compact premixed flame located within it. A laminar inviscid flow with Mach number M approaching zero is assumed (Nicoud and Wieczorek, 2009). In order to simplify the analysis, a constant density assumption is made such that the mean density ρ_0 and the speed of sound in the unburnt mixture c_0 are assumed to be constant throughout the duct. The flame is treated as a compact source and the heat release rate distribution along the duct can be represented by a Dirac-delta function. The location of the flame is the point of attachment of the flame front to the anchoring wire; i.e. at $\tilde{y} = \tilde{y}_f$.

The acoustic wave propagation on either side of the compact source within the duct can be assumed to be linear even when the nonlinear dependence of the heat release rate on velocity fluctuations is retained. This is because the amplitudes of the acoustic pressure fluctuations in the present thermoacoustic system are not significant enough to introduce nonlinear gas dynamic effects (Dowling, 1997). Below the cut-on frequency, only the axial modes of sound propagate in the duct. Therefore, the acoustic quantities are assumed to vary only axially. The non-dimensional acoustic equations for momentum and energy used in the present analysis are

$$\gamma M \frac{\partial u'}{\partial t} + \frac{\partial p'}{\partial y_a} = 0\,, \tag{4.16}$$

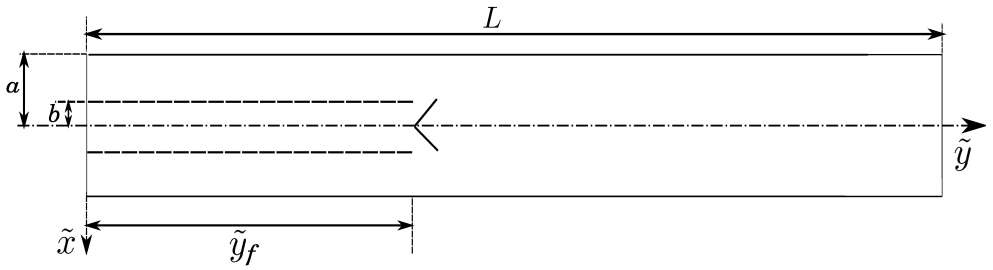

Figure 4.2: Geometry of the coupled premixed flame thermoacoustic system. Here L is the length of the duct, (b/a) is the ratio of burner to duct radius and $\tilde{y}_f$ is the flame location along the length of the duct.

$$\frac{\partial p'}{\partial t} + \gamma M \frac{\partial u'}{\partial y_a} = (\gamma - 1)\frac{\dot{\tilde{q}}'_f}{\rho_0 c_0^3}\delta(y_a - y_{fa})\,. \tag{4.17}$$

These equations have been non-dimensionalized using the scales of non-dimensionalisation given below (Balasubramanian and Sujith, 2008*a*):

$$y_a = \tilde{y}/L; u = \tilde{u}/\bar{u}; t = \tilde{t}c_0/L; p = \tilde{p}/\bar{p}; \dot{q'_f} = \dot{\tilde{q}}'_f/\rho_0 c_0^3; \delta = L\tilde{\delta}\,. \tag{4.18}$$

where γ is the ratio of specific heats, p' is the non-dimensional acoustic pressure, u' is the non-dimensional acoustic velocity, $\dot{\tilde{q}}'_f$ is the heat release rate fluctuations averaged over the cross-sectional area of the duct, L is the duct length and the compact heat source is represented as the Dirac-delta function $\delta(y_a - y_{fa})$. In this chapter, the super-script tilde denotes dimensional quantities and quantities without tilde are non-dimensional. The sub-script 'a' denotes that the variable has been non-dimensionalized with respect to the acoustic scale.

The heat release rate fluctuation averaged over the cross sectional area of the duct $(\tilde{A}_{CS} = \pi a^2)$ is given as $\dot{\tilde{q}}'_f = \dot{\tilde{q}}'/\tilde{A}_{CS}$. Therefore the expression for the fluctuating heat release rate per unit area for the linearized model can be written using (4.15) as

$$\dot{\tilde{q}}'_f = \frac{\rho_0 S_L \Delta q_R \tilde{A}'(t)}{\tilde{A}_{CS}} = -2\cot\alpha\ \rho_0 S_L \Delta q_R \left(\frac{b^2}{a^2 \sin\alpha}\right) \int_{X=0}^{X=1} \xi' dX\,. \tag{4.19}$$

Defining the constant $\Omega = -\left(L/\rho_0 c_0^3\right)\left(2\cot\alpha\rho_0 S_L \Delta q_R\right)\left(b^2/a^2\sin\alpha\right)$ the equation for the non-dimensional heat release rate fluctuations per unit area of the duct can be

written as given below:

$$\dot{q}'_f = \left(\frac{L}{\rho_0 c_0^3}\right) \dot{\tilde{q}}'_f = \Omega \int_{X=0}^{X=1} \xi' dX \,. \tag{4.20}$$

The acoustic equations for momentum and energy are partial differential equations. They can be converted into a set of ordinary differential equations by the method of Galerkin expansion (Meirovitch, 1967; Zinn and Lores, 1971). In the method of Galerkin expansion, the acoustic variables of velocity and pressure are expanded in terms of a set of basis functions which satisfy the boundary conditions for the acoustic field. In the present case, they correspond to the boundary conditions of a duct which is open at both ends as:

$$u' = \sum_{j=1}^{N} \cos\left(j\pi y_a\right) \eta_j\left(t\right) \quad \text{and} \quad p' = \gamma M \sum_{j=1}^{N} \sin\left(j\pi y_a\right) \left(\frac{-\dot{\eta}_j}{j\pi}\right)\left(t\right). \tag{4.21}$$

A mode dependent damping is introduced as given by Matveev (2003*a*) in the acoustic energy equation, where the expression for the damping coefficient ζ_j is given by

$$\zeta_j = \frac{1}{2\pi}\left(c_1 j + c_2\sqrt{\frac{1}{j}}\right) , \tag{4.22}$$

where c_1 is representative of the losses due to radiation from the open ends and c_2 represents the acoustic boundary layer losses (Sterling and Zukowski, 1991). The resulting system of ordinary differential equations which describes the evolution of the acoustic field for the system with damping is as given below:

$$\frac{d\eta_j}{dt} = -j\pi\left(\frac{-\dot{\eta}_j}{j\pi}\right) , \tag{4.23}$$

$$\frac{d}{dt}\left(\frac{-\dot{\eta}_j}{j\pi}\right) = j\pi\eta_j - 2\zeta_j j\pi\left(\frac{-\dot{\eta}_j}{j\pi}\right) + \frac{2(\gamma-1)}{\gamma M}\dot{q}'_f\left(t\right)\sin\left(j\pi y_{fa}\right) . \tag{4.24}$$

4.4 Flame front as a distribution of monopole sources

The flame front can be represented as a source of sound using the acoustic analogy (Lighthill, 1952). Unsteady heat addition from the flame at constant pressure causes a corresponding unsteady expansion of the fluid. Across a one-dimensional flame with area A_f, this dilatation term leads to a velocity jump of $\delta u'_f$ resulting in an instantaneous value of volume flow rate $A_f \delta u'_f$ (Chu and Kovasznay, 1958; Wu *et al.*, 2003). This dilatation can be represented as the sum of source strengths of a distribution of monopole sources of sound, with source strength S per unit length S along the flame front (Morse and Ingard, 1968; Dowling and Williams, 1983; Howe, 1998). Thus, the laminar flame front is represented by a distribution of monopole sources of sound (van Kampen, 2006).

The flame front is discretised into P flame elements each of equal length $\triangle\tilde{X}$, each of which represents an acoustic monopole source of strength $\tilde{S}_i \triangle\tilde{X}$. The monopole strength per unit length $\tilde{S}_i$ can be non-dimensionalised as follows:

$$S_i = \frac{1}{\gamma \bar{u} L} \tilde{S}_i \,. \tag{4.25}$$

In the rest of this section, we derive the energy due to heat release rate fluctuations of the flame front in terms of monopole strength averaged over the cross sectional area of the duct. As the initial step, Eqn. (4.19) can be rewritten to linearly relate the local flame displacement to the non-dimensional heat release rate fluctuation per unit area as given below:

$$\dot{q}'_f = \sum_{i=1}^{P} \dot{q}'_{fi} = \Omega \sum_{i=1}^{P} f_i \xi'_i \triangle X \,, \tag{4.26}$$

given that we denote Ω as defined after Eqn. (4.19) and are the weight factors corresponding to the trapezoidal integration formula as given below:

$$f_i = \begin{cases} \frac{1}{2}, i = 1 \mathrm{and} \mathrm{P}, \\ 1, i \neq 1 \mathrm{or} \mathrm{P}. \end{cases} \tag{4.27}$$

The integration of the acoustic equation for energy given by Eqn. (4.17) across the heat source relates the acoustic velocity gradient to the heat source as given below in

Eqns. (4.28) to (4.32):

$$\int_{y_f^-}^{y_f^+} \left(\frac{\partial p'}{\partial t} + \gamma M \frac{\partial u'}{\partial y_a} \right) dV_c = \int_{y_f^-}^{y_f^+} (\gamma - 1) \dot{q}'_f \delta(y_a - y_{fa}) dV_c \,. \tag{4.28}$$

Here y_f^- and y_f^+ are the locations just upstream and downstream of the flame front and the sub-script c denotes the combustion zone. The contribution from the acoustic pressure term vanishes for a compact source as $dV_c \to 0$. Applying Gauss divergence theorem to the acoustic gradient term, we can re-write the left hand side of the Eqn. (4.28) as given below:

$$\gamma M \int_{y_f^-}^{y_f^+} \left(\frac{\partial u'}{\partial y_a} \right) dV_c = \gamma M \int_{S_c} (u' \cdot \hat{n}) \, dS_c \,. \tag{4.29}$$

The surface integral is evaluated over a cylindrical area S_c, which encloses the flame and whose lateral surface coincides with that of the duct. Here, $\hat{n}$ denotes the outward normal from the surface.

As the velocity field is assumed to be one dimensional, the contribution to the integral from the lateral surface vanishes identically. Further, the acoustic velocity is assumed to be uniform across the cross-sectional area of the duct, consistent with a one-dimensional approximation. Therefore, the contribution to this surface integral from the left and right faces of the cylindrical area are $(-A_{CS} u'_{f-})$ and $(A_{CS} u'_{f+})$ respectively as given in the right hand term in (4.30),

$$(\gamma - 1) \int_{y_f^-}^{y_f^+} \dot{q}'_f \delta(y_a - y_{fa}) dV_c = \gamma M A_{CS} \left(\delta u'_f \right) \,. \tag{4.30}$$

Using the one-dimensional approximation, the volume integral in the left hand side term of (4.30) is replaced as the product of the cross-sectional area A_{CS} times an integral along the length of the duct,

$$(\gamma - 1) \int_{\delta^-}^{\delta^+} \dot{q}'_f \delta(y_a - y_{fa}) dV_c = (\gamma - 1) A_{CS} \, \dot{q}'_f|_{y_a = y_{fa}} \,. \tag{4.31}$$

Comparing the right hand sides of (4.30) and (4.31), the jump in acoustic velocity across the heat source $\delta u'_f$ can be related to the fluctuations in heat release rate as given below:

$$\delta u'_f = \frac{(\gamma - 1)}{\gamma M} \, \dot{q}'_f|_{y_a = y_{fa}} \, . \tag{4.32}$$

The jump in acoustic velocity $\delta u'_{fi}$ across the i^{th} monopole can be related in terms of the monopole strength $S_i \triangle X$ averaged over the cross sectional area of the duct as given below (Morse and Ingard, 1968; Dowling and Williams, 1983; Howe, 1998):

$$\delta u'_{fi} = \frac{S_i \triangle X}{A_{CS}} \, , \tag{4.33}$$

which we will use later in Section 4.5.2 to calculate the energy due to fluctuations in heat release rate.

4.5 Energy due to fluctuations in a premixed flame-acoustic system

4.5.1 Energy in the acoustic field

The acoustic energy can be written in terms of the acoustic velocity and pressure as given below (Reinstra and Hirschberg, 2008):

$$\tilde{E}_a(t) = \frac{1}{2} \int\limits_{\tilde{V}_a} \left[\left(\rho_0 \tilde{u}'^2 \right) + \left(\frac{\tilde{p}'^2}{\rho_0 c_0^2} \right) \right] d\tilde{V}_a = \frac{1}{2} A_{CS} L \int\limits_{y_a=0}^{y_a=1} \left[\left(\rho_0 \tilde{u}'^2 \right) + \left(\frac{\tilde{p}'^2}{\rho_0 c_0^2} \right) \right] dy_a \, . \tag{4.34}$$

Non-dimensionalizing the above expression with the kinetic energy of the steady-state flow, $\frac{1}{2} \rho_0 \bar{u}^2 A_{CS} L$, we obtain the expression for non-dimensional acoustic energy as below:

$$E_a(t) = \frac{\tilde{E}_a(t)}{\frac{1}{2} \rho_0 \bar{u}^2 A_{CS} L} = \int\limits_{y=0}^{y=1} \left[u'^2 + \left(\frac{p'}{\gamma M} \right)^2 \right] dy_a \, . \tag{4.35}$$

We expand the acoustic variables in terms of the basis functions as given in Eqn. (4.21) and integrate over the acoustic domain. Making use of their orthogonality property, the

expression for acoustic energy can be modified into the following equation:

$$E_a(t) = \frac{1}{2}\sum_{j=1}^{N}\left[\eta_j(t)^2 + \left(\frac{-\dot{\eta}_j(t)}{j\pi}\right)^2\right]. \tag{4.36}$$

4.5.2 Energy due to fluctuations in heat release rate

In Section 4.4, the unsteady heat addition at the flame front was related to unsteady expansion of the fluid across it. The energy due to dilatation at the monopole distribution $\tilde{E}_f$ (Morse and Ingard, 1968) is written in the dimensional form as given below:

$$\tilde{E}_f(t) = \frac{1}{2}\int_{\tilde{V}_a}\left[\rho_0\sum_{i=1}^{P}\left(\delta\tilde{u}'_{fi}\right)^2\right]d\tilde{V}_a = \frac{1}{2}A_{CS}L\int_{y_a=0}^{y_a=1}\left[\rho_0\sum_{i=1}^{P}\left(\delta\tilde{u}'_{fi}\right)^2\right]dy_a\,. \tag{4.37}$$

Non-dimensionalizing the above the kinetic energy of the steady-state flow $\frac{1}{2}\rho_0\bar{u}^2A_{CS}L$, we obtain the non-dimensional expression for the energy of the monopole distribution as

$$E_f(t) = \frac{\tilde{E}_f(t)}{\frac{1}{2}\rho_0\bar{u}^2A_{CS}L} = \sum_{i=1}^{P}(\delta u'_{fi})^2 \tag{4.38}$$

Using Eqn. (4.33), we can rewrite the expression for energy E_f in terms of monopole strengths to obtain,

$$E_f(t) = \sum_{i=1}^{P}\left[\frac{S_i(t)\triangle X}{A_{CS}}\right]^2. \tag{4.39}$$

The dilatation due to the presence of a flame front is modeled using a monopole distribution. The contribution to fluctuating energy due to unsteady heat release rate can now be expressed in terms of the monopole strength averaged over the cross sectional area of the duct. Note that the expression for the fluctuating energy as derived in Eqn. (4.39) is not the acoustic power of a distribution of monopole sources (Morse and Ingard, 1968).

The total energy $E(t)$ due to fluctuations in a premixed flame-acoustic system includes contributions from the acoustic energy and the energy of the monopole distribution arising from the heat release rate fluctuations. Thus $E(t)$ can be expressed as

$$E(t) = E_a(t) + E_f(t) = \sum_{j=1}^{N} \frac{1}{2} \left[\eta_j(t)^2 + \left(\frac{-\dot{\eta}_j(t)}{j\pi} \right)^2 \right] + \sum_{i=1}^{P} \left[\frac{S_i(t) \triangle X}{A_{CS}} \right]^2 . \quad (4.40)$$

4.6 Evolution equations for a ducted premixed flame

The time scale used in the non-dimensional front tracking equation is $(t_c = b/\bar{u}\sin\alpha)$ different from the time scale used for the acoustic equations for momentum and energy $(t = L/c_0)$. In order to evolve both the equations using a single time marching technique, the non-dimensional front tracking equation is non-dimentionalised with the acoustic time scale. Convertion of the one time scale to another is given as

$$\left(\frac{L}{c_0} \frac{\bar{u}\sin\alpha}{b} \right) \frac{\partial}{\partial t_c} = \frac{\partial}{\partial t} ,$$

such that the front tracking equation can be modified as given in Eqns. (4.43) and (4.48). Also, the flame front is discretised into P different flame elements along its length such that the partial differential equation that governs the flame front evolution can be converted into P ordinary differential equations.

4.6.1 Linear analysis

The coupled system of equations for the premixed flame thermoacoustic system under the linear approximation can be written as given below.

$$\frac{d\eta_j}{dt} = -j\pi \left(\frac{-\dot{\eta}_j}{j\pi} \right) , \quad (4.41)$$

$$\frac{d}{dt} \left(\frac{-\dot{\eta}_j}{j\pi} \right) = j\pi\eta_j - 2\zeta_j j\pi \left(\frac{-\dot{\eta}_j}{j\pi} \right) + \frac{2(\gamma-1)}{\gamma M} \dot{q}'_f(t) \sin(j\pi y_{fa}) , \quad (4.42)$$

$$\frac{d\xi'_i}{dt} = \left(\frac{L\bar{u}\sin^2\alpha}{c_0 b} \right) \sum_{j=1}^{N} \cos(j\pi y_{fa})\eta_j - \left(\frac{L\bar{u}\sin\alpha\cos\alpha}{c_0 b} \right) \left(\frac{\triangle\xi'}{\triangle X} \right)_i . \quad (4.43)$$

Here, the gradient term $\left(\triangle\xi'/\triangle X\right)_i$ in the front tracking equation in expanded using a first order backward difference formula as discussed in Section 4.2.

Equation (4.41) is retained as such, while (4.42) is rewritten in terms of the strength

of monopole distribution as given in Eqn. (4.44):

$$\frac{d}{dt}\left(\frac{-\dot{\eta}_j}{j\pi}\right) = j\pi\eta_j - 2\zeta_j j\pi\left(\frac{-\dot{\eta}_j}{j\pi}\right) + \sqrt{2}\sin\left(j\pi y_{fa}\right)\sum_{i=1}^{P} H_i\,. \tag{4.44}$$

With H_i representing the monopole strength averaged over the cross-sectional area of the duct and defining the constants θ_1 and θ_2,

$$\begin{aligned} H_i &= \left(\frac{S_i \triangle X\sqrt{2}}{A_{CS}}\right), \\ \theta_1 = \left(\frac{(\gamma-1)\Omega\triangle X\sqrt{2}}{\gamma M}\right)\left(\frac{L\bar{u}\sin^2\alpha}{c_0 b}\right) &\text{ and } \theta_2 = \left(\frac{L\bar{u}\sin\alpha\cos\alpha}{c_0 b\triangle X}\right). \end{aligned} \tag{4.45}$$

the flame front evolution (4.43) is converted to Eqn. (4.46) using relations (4.33) and (4.26):

$$\frac{dH_i}{dt} = \theta_1\sum_{j=1}^{N}\cos(j\pi y)\eta_j - \theta_2\left(H_i - H_{(i-1)}\right). \tag{4.46}$$

The state vector $\chi = [\eta_1\ (-\dot{\eta}_1/\pi)\ \eta_2\ (-\dot{\eta}_2/2\pi)\ \cdots\ (-\dot{\eta}_N/N\pi)\ H_1\ H_2\ \cdots\ H_P]^T$ is defined such that the square of the L^2 norm of the state vector is proportional to the energy of fluctuations $E(t)$. The ratio of the squares of the L^2 norm of the state vector at time t to that at time $t = 0$, gives the normalized energy of fluctuations as given below:

$$\frac{E(t)}{E(0)} = \frac{\left(\sum_{j=1}^{N}\left[\eta_j(t)^2 + \left(\frac{-\dot{\eta}_j(t)}{j\pi}\right)^2\right] + \sum_{i=1}^{P} H_i(t)^2\right)}{\left(\sum_{j=1}^{N}\left[\eta_j(0)^2 + \left(\frac{-\dot{\eta}_j(0)}{j\pi}\right)^2\right] + \sum_{i=1}^{P} H_i(0)^2\right)}. \tag{4.47}$$

Thus the set of linear equations which describes the evolution of a premixed flame thermoacoustic system are given by the Eqns. (4.41), (4.44) and (4.46).

4.6.2 Nonlinear analysis

The nonlinear partial differential equation which governs the evolution of the flame front expressed in the acoustic time scale is

$$\frac{\partial \xi'}{\partial t} = \left(\frac{L\bar{u}\sin^2\alpha}{c_0 b}\right)\left(1 + u'_f - \sqrt{1+\left(\frac{\partial \xi'}{\partial X}\right)^2}\right) - \left(\frac{L\bar{u}\sin\alpha\cos\alpha}{c_0 b}\right)(1+u'_f)\left(\frac{\partial \xi'}{\partial X}\right). \tag{4.48}$$

The discretised set of equations for the evolution of the flame front can be written as below for every $i = 1, 2, \ldots, P$, where P is the number of points along the flame front:

$$\frac{d\xi'_i}{dt} = \left(\frac{L\bar{u}\sin^2\alpha}{c_0 b}\right)\left(1 + u'_f - \sqrt{1+\left(\frac{\Delta \xi'_i}{\Delta X}\right)^2}\right) - \left(\frac{L\bar{u}\sin\alpha\cos\alpha}{c_0 b}\right)(1+u'_f)\left(\frac{\Delta \xi'_i}{\Delta X}\right). \tag{4.49}$$

Here $(\Delta\xi'_i/\Delta X)$ is the fifth-order accurate approximation of the spatial derivative using the WENO scheme given in Appendix C. The governing equations for the nonlinear system are the linearized acoustic equations for momentum and energy (4.41) and (4.42) and the nonlinear evolution equation for the premixed flame given in (4.49). In Eqn. (4.42), the heat release rate is substituted in terms of the flame displacement as

$$\dot{q}'_f = \frac{S_L \triangle q_R}{c_0^3}\left(\frac{2}{\sin\alpha}\int_{X=0}^{X=1}(X\sin\alpha - \xi'\cos\alpha)\sqrt{1+\left(\frac{\partial \xi'}{\partial X}\right)^2}\,dX - 1\right). \tag{4.50}$$

Two measures are chosen to check for the convergence with increasing number of acoustic modes and number of flame elements. The number of acoustic modes is varied in steps of one and the number of flame elements is varied in steps of 25 and the following two relative changes are calculated. The relative changes due to variation of the number of acoustic modes N are given as below. The relative change in maximum transient growth Φ_1 and the relative change in the average acoustic velocity at the flame for the optimal initial condition Φ_2 are

$$\Phi_1 = \frac{G_{max(N)} - G_{max(N-1)}}{G_{max(N)}} \text{ and } \Phi_2 = \frac{u'_{f(N)} - u'_{f(N-1)}}{u'_{f(N)}}.$$

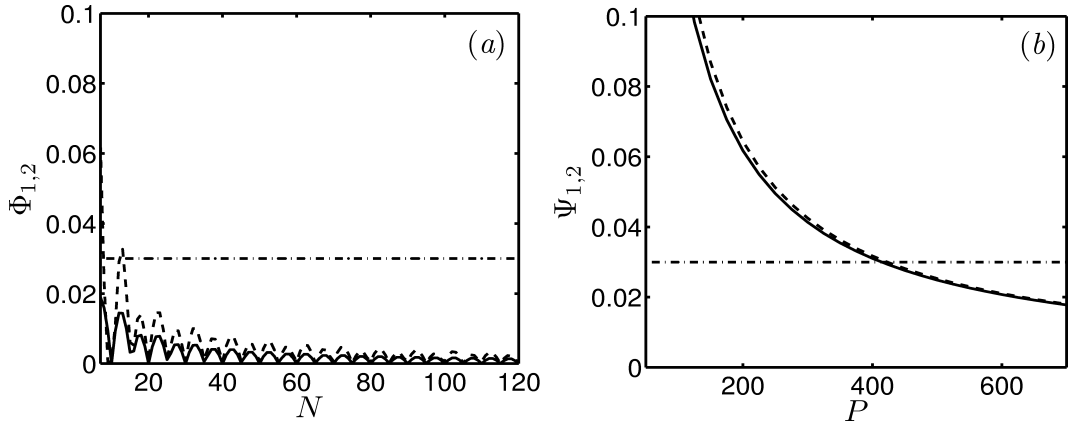

Figure 4.3: (a) Relative change in the average value of acoustic velocity at the flame for the optimal initial condition u'_f as Φ_1 '$-\ -\ -$' and relative change in maximum transient growth G_{max} as Φ'_2'———' with the number of acoustic modes N and 500 flame elements, (b) Relative change in u'_f as Ψ_1 '$-\ -\ -$' and relative change in G_{max} as Ψ_2 '———' with the number of flame elements P and 100 acoustic modes at $\alpha = 10^0$, $y_f = 0.1$, $c_1 = 1.5 \times 10^{-2}$, $c_2 = 1.5 \times 10^{-3}$, $b/a = 0.5$, $\phi = 1$, $S_L = 0.4129$ m/s and $\triangle q_R = 2.7522 \times 10^6$ J/Kg. In both the figures, '$-\cdot-\cdot-\cdot-$' is the level indicating a relative change of 3%.

Relative changes due to variation in the number of flame elements P are as given below. The relative change in maximum transient growth Ψ_1 and the relative change in the average acoustic velocity at the flame for the optimal initial condition Ψ_2 are

$$\Psi_1 = \frac{G_{max(P)} - G_{max(P-25)}}{G_{max(P)}} \text{ and } \Psi_2 = \frac{u'_{f(P)} - u'_{f(P-25)}}{u'_{f(P)}}.$$

Figure 3 (a) plots the variation of Φ_1 and Φ_2 with change in the number of acoustic modes N for the case with system parameters $\alpha = 10^0$, $y_f = 0.1$, $c_1 = 1.5 \times 10^{-2}$, $c_1 = 1.5 \times 10^{-3}$, $b/a = 0.5$, $\phi = 1$, $S_L = 0.4129$ m/s and $\triangle q_R = 2.7522 \times 10^6$ J/Kg. Figure 3 (b) plots the relative changes Ψ_1 and Ψ_2 for variation in the number of flame elements P for the same case. It is seen that the relative changes in both the maximum transient growth and the acoustic velocity at the flame location for the optimal initial condition are less than 3% for $N = 100$ acoustic modes and $P = 500$ flame elements.

Further, with 100 Galerkin modes retained in the expansion of acoustic variables, the jump in acoustic velocity across the heat source is sufficiently well resolved as shown in Fig. 7 (a). With these choices, the set of ordinary differential equations given by (4.41), (4.44) and (4.46) are evolved in time using the matrix exponential of the linear operator

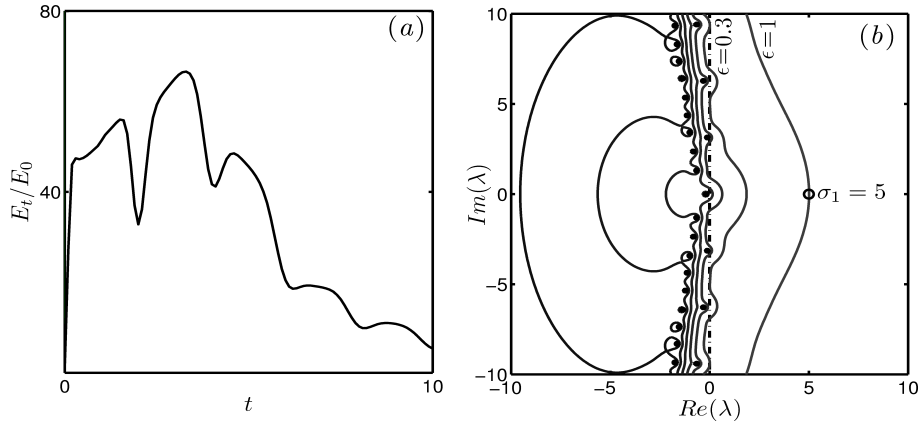

Figure 4.4: (a) Evolution of the ratio of energy at an instant $E(t)$ to the initial energy $E(0)$ in the acoustic time scale t, for the optimal initial condition and (b) Pseudospectra of the linearized matrix of a linearly stable system with $\alpha = 10^0$, $y_f = 0.08$, $c_1 = 0.135$, $c_2 = 1.5 \times 10^{-2}$, $b/a = 0.5$, $\phi = 1$, $S_L = 0.4129$ m/s and $\triangle q_R = 2.7522 \times 10^6$ J/Kg.

(Hirsch *et al.*, 2004) for linear analysis. In the nonlinear analysis, the set of equations given by (4.41), (4.42) and (4.49) are evolved with a time marching technique using Runge-Kutta third order scheme with TVD property (Jiang and Shu, 1996) with a CFL number of 0.01.

4.7 Quantification of transient growth

In addition to the variables for acoustic velocity and pressure, the state vector of the self evolving system consists of variables for the strengths of the monopole sources associated with the flame elements. The measure chosen in this chapter to quantify transient growth contains contributions from the dilatation resulting from the fluctuating heat release rate in addition to the classical acoustic energy. The square of the L^2 norm of the state vector at time t gives the net energy of fluctuations $E(t)$. The fluctuation energy is normalized with its value at time $t = 0$ as given in Eqn. (4.47).

This normalized energy when maximized over all possible initial conditions and over all times is called maximum growth factor G_{max} and it represents the maximum possible amplification for the fluctuating energy of a given system. The optimal initial condition for maximum transient growth in a linear system can be obtained by singular value decomposition of the operator governing the linearized system. Evolution of

the normalized energy for a linearly stable case from the corresponding optimal initial condition is shown in Fig. 4.4 (a). The system configuration chosen is the same as for Fig. 4.3. The optimal initial condition, maximized over all time, is observed to undergo a transient amplification of 66.7 times the initial energy and attain this maximum amplification at $t_{max} = 3.3$.

For a non-normal system, the evolution of the system at finite time cannot be adequately characterized by the eigenvalues of the linearized system. In such cases, if B is the linear operator of the system, the eigenvalues enforce a bound on the growth factor $\| \exp(tB)\|$ only for $t \to \infty$. The normalized net energy of fluctuations is given by the square of the growth factor. Pseudospectra of the linearized operator can be analyzed to obtain the magnitude of transient amplification of energy of the fluctuations. The time scale over which transient growth occurs can also be estimated from the pseudospectra of the linearized matrix.

The ϵ-pseudospectrum for the linear operator B is a set of points in the complex plane which are the eigenvalues of a perturbed matrix $(B + T)$, such that the random perturbation T to the operator satisfies the condition $\|T\| < \epsilon$. On a given ϵ-pseudospectrum, the pseudospectral abscissa σ_ϵ gives the location of the point on the real axis with the largest value. If the value of σ_ϵ is positive, such that $(\sigma_\epsilon(B)/\epsilon) > 1$, then transient growth is indicated. The ratio of $(\sigma_\epsilon(B)/\epsilon)$ maximized over all ϵ gives the minimum value of transient growth possible. A lower bound on the magnitude of the transient growth can be given in terms of the Kreiss constant $\kappa(B)$ from the Kreiss matrix theorem as given below (Trefethen and Embree, 2005):

$$\sup_{t \geq 0} \|e^{tB}\| \geq \sup_{\epsilon > 0} \frac{\sigma_\epsilon(B)}{\epsilon} = \kappa(B)\,. \tag{4.51}$$

The upper bound on transient growth $\varphi(B)$ for a matrix of dimension $(2N + P)$ is also given by the Kreiss matrix theorem in terms of $\kappa(B)$ as below:

$$\|e^{tB}\| \leq e(2N + P)\kappa(B) = \varphi(B)\,. \tag{4.52}$$

In the case of a linearly unstable system, when z' is the location of the eigenvalue with the largest positive real part, exponential growth occurs within a time span of $1/Re(z')$.

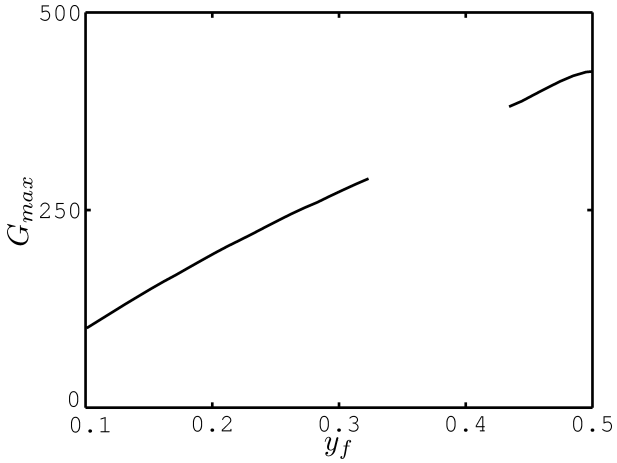

Figure 4.5: Variation of G_{max} with y_f for the system with $\alpha = 10^0$, $c_1 = 1.5 \times 10^{-2}$, $c_2 = 1.5 \times 10^{-3}$, $b/a = 0.5$, $\phi = 1$, $S_L = 0.4129$ m/s and $\triangle q_R = 2.7522 \times 10^6$ J/Kg. Blank spaces indicate configurations for which the system is linearly unstable.

In the case of a linearly stable system, the ϵ-pseudoeigenvalue of the system with the largest value determines the time span over which transient growth occurs. When the pseudospectral abscissa σ_ϵ is the ϵ-pseudoeigenvalue of the system with the largest real part, the system experiences a transient growth of the order of over a time span $1/\sigma_\epsilon$ (Trefethen and Embree, 2005).

Thus, the pseudospectra of the linear matrix give us bounds for the evolution of normalized energy (E_t/E_0) at finite time. For the case of a premixed flame with $\phi = 1$ and flame angle of $\alpha = 10^0$, which is stabilized at $y_f = 0.08$, the pseudospectra of the system are given in Fig. 4.4 (b). We see that the pseudospectra spill onto the right half plane. The perturbation amplitude $\epsilon = 1$ gives a ratio of $\epsilon/||L|| = 7.04 \times 10^{-4}$, which implies that the perturbations are very small compared to the norm of the linear operator. The pseudospectrum corresponding to $\epsilon = 1$ is seen to protrude by $\sigma_1 = 5$ units into the right half plane. The ratio of the protrusion of the pseudospectra to the corresponding perturbation amplitude is greater than one, indicative of transient growth. This ratio when maximized over all perturbation amplitudes gives the Kreiss constant for this case as $\kappa(B) = 6.4$, with $\sigma = 0.64$ and $\epsilon/||L|| = 7.04 \times 10^{-5}$ for $\epsilon = 0.1$. The Kreiss constant sets the lower bound for transient amplification of energy to be $\kappa^2(B) = 41$ from pseudospectra. The upper bound for transient growth is given as $\varphi(B) = 7.7 \times 10^4$. The maximum value of normalized energy amplification is 66.7, as shown in Fig. 4.4 (a), which falls within the bounds estimated from pseudospectra. The

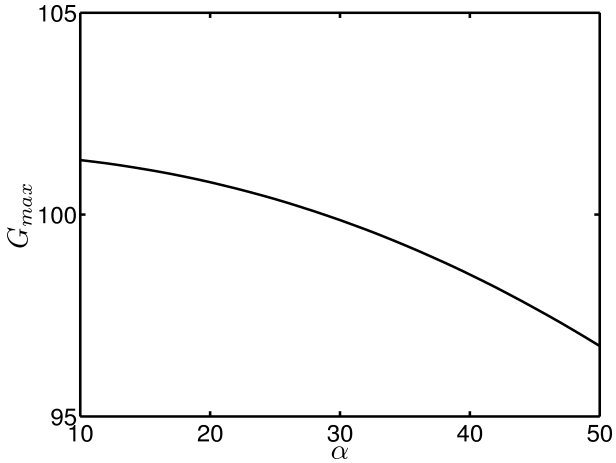

Figure 4.6: Variation of G_{max} with α for the system with $y_f = 0.1$, $c_1 = 1.5 \times 10^{-2}$, $c_2 = 1.5 \times 10^{-3}$, $b/a = 0.5$, $\phi = 1$, $S_L = 0.4129$ m/s and $\triangle q_R = 2.7522 \times 10^6$ J/Kg.

estimated time scale for transient growth from pseudospectra is $t_{max} = 1.6$, which is of the same order as the computed time for maximum growth, $t_{max} = 3.3$.

Variation of G_{max} with system parameters is obtained to quantify the effect of system parameters on the non-normality of the system. Significant system parameters considered are flame location y_f and flame angle α. The variation of G_{max} with the location of the flame is shown in Fig. 4.5 for a flame angle of $\alpha = 10^0$. It is seen that G_{max} increases with increase in y_f till the half duct length. The blank spaces in the distributions in Fig. 4.5 are configurations for which the system is linearly unstable. The system is linearly unstable for locations of the flame beyond the half duct length. The dependence of the growth factor on the flame angle is as shown in Fig. 4.6 for $y_f = 0.1$. The transient growth observed is stronger for elongated flames than for flatter flames. When α is small, i.e. for elongated flames, the convective term dominates the linear evolution of the flame front as given in Eqn. (4.4). Increased non-normality was observed with increased advection in the context of ducted diffusion flames by Balasubramanian and Sujith (2008*a*), who reported that the maximum growth factor was seen to increase with an increase in the Peclet number.

4.8 Influence of internal flame dynamics on the linear evolution of the ducted premixed flame

In addition to the acoustic equations for momentum and energy, the dynamical system described in Section 4.6.1 includes the evolution equation for the flame front in terms of the monopole strength averaged over the cross-sectional area of the duct. If the flame front is thought of as consisting of a number of small flame elements, the flame displacements at these points represent a large number of additional degrees of freedom which we refer to as the internal degrees of freedom of the flame front or internal flame dynamics. The linearized system of equations from (4.41), (4.44) and (4.46) can be written in matrix form as

$$\frac{d\chi}{dt} = B\chi = \underbrace{\begin{pmatrix} C_{2N\times 2N} & D_{2N\times P} \\ E_{P\times 2N} & F_{P\times P} \end{pmatrix}}_{(2N+P)\times(2N+P)} \chi_{(2N+P)\times 1}\,. \tag{4.53}$$

Here, χ is the state vector and B is the operator governing the linearized thermoacoustic system as expanded in Appendix D. The size of the linearized operator B is $(2N+P)\times(2N+P)$ for N number of acoustic modes and P number of points along the flame. The sub-matrix C is the linearized operator which governs the evolution of acoustic modes in the absence of a heat source and has the size $(2N \times 2N)$. Thus the self evolving thermoacoustic system has more degrees of freedom than just the number of acoustic modes. The sub-matrix D contains the effect of flame dynamics on the acoustic modes and E represents the acoustic driving term in the evolution for the monopole sources. The sub-matrix F represents the interaction between the monopole sources that represent the flame front.

The optimal initial condition can be obtained using singular value decomposition (SVD) of the linear operator of the system (Schmid and Henningson, 2001). The optimal initial condition was obtained for the case examined in Figs. 4.3 and 4.4. In the kinematic model considered, the heat release rate fluctuations are correlated to the monopole strength distribution along the flame. The optimal initial condition has significant projections onto the monopole strength distribution. The evolution from the optimum initial condition at different instances of time as seen through the projections

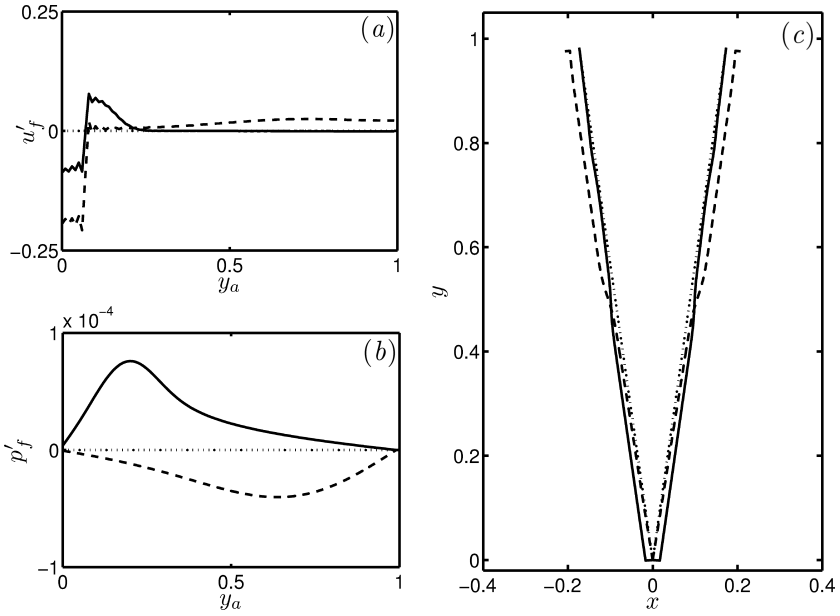

Figure 4.7: (a) Acoustic velocity field, (b) Acoustic pressure field and (c) Flame shape for evolution of optimal initial condition maximized over all time, with $E_t(0) = 1 \times 10^{-4}$ for $\alpha = 10^0$, $y_f = 0.08$, $c_1 = 0.135$, $c_2 = 1.5 \times 10^{-2}$, $b/a = 0.5$, $\phi = 1$, $S_L = 0.4129$ m/s and $\triangle q_R = 2.7522 \times 10^6$ J/Kg where $\cdots\cdots$ is the unperturbed state; ——— is distribution for the optimal initial condition and $- - --$ is distribution at $t = t_{max} = 3.3$.

on acoustic velocity, pressure and the displacement of the flame shape are shown in Fig. 4.7. The acoustic velocity and pressure distributions along the duct and the displacement of the flame shape for the optimal initial condition at time instances $t = 0$ and at time $t = t_{max} = 3.3$ are shown in Fig. 4.7 (a) to Fig. 4.7 (c). The acoustic velocity distribution in Fig. 4.7 (a) shows a jump while the pressure distribution in Fig. 4.7 (b) is continuous across the flame location.

Inclusion of the monopole strengths in the state space increases the number of degrees of freedom in the system from $(2N \times 2N)$ to $(2N + P) \times (2N + P)$. Traditionally, thermoacoustic instability has been analyzed in terms of an acoustic model which is driven by combustion. In this traditional approach, a time lag model (Schuermans *et al.*, 2004; Noiray *et al.*, 2006) or a lumped model (Annaswamy *et al.*, 1997) has been used to model the heat release rate fluctuations. When the flame front is modeled with a time lag model or as lumped model, it is not possible to prescribe an initial condition for the flame shape (monopole source strength distribution).

However, the coupled system can have initial perturbations both in the acoustic vari-

ables as well as the position of the flame front. Therefore, in order to include the possibility of an initially perturbed flame shape (i.e., an initial non-zero monopole strength distribution), the variables corresponding to the monopole source strengths must be included in the state variables of the system. Inclusion of the monopole source strength variables in the state space retains the internal degrees of freedom of the flame front. This is particularly significant as the ability to predict transient growth in a non-normal system is affected by the degrees of freedom of the model (Trefethen and Embree, 2005).

4.9 Sub-critical transition to instability

A system that is predicted to be stable by classical linear stability theory can become nonlinearly unstable for large amplitudes of initial perturbation and reach a limit cycle oscillation. This type of stability transition depending upon the amplitude of the initial perturbation is called sub-critical transition to instability. The evolutions of acoustic velocity for the linearized and nonlinear systems are compared in Fig. 4.8 ($a\&b$) for the system configuration with $\alpha = 10^0$, $y_f = 0.2$, $c_1 = 2 \times 10^{-3}$, $c_2 = 2 \times 10^{-4}$, $\phi = 0.8$, $S_L = 0.2782$ m/s and $\triangle q_R = 2.2263 \times 10^6$ J/Kg. An initial condition purely in the acoustic variables with $\eta_1(0) = 0.002$, $\eta_i(0) = 0 \; \forall \; i \neq 1$ and $\dot{\eta}_i(0) = 0 \; \forall \; i = 1 \; to \; N$ is given with an initial acoustic velocity of $u'_f(0) = 1.6 \times 10^{-3}$, and the initial energy due to fluctuations being $E(0) = 4 \times 10^{-6}$. The system is linearly stable and the linear evolution decays asymptotically without any transient growth. The nonlinear evolution also decays asymptotically.

In a non-normal system, the transient growth obtained is dependent on the initial condition applied to the system. The initial condition which maximizes the transient amplification of energy is called the optimal initial condition. Figure 4.9 shows the evolution of the linear and nonlinear system from the optimal initial condition for the same linearly stable case as shown in Fig. 4.8. The energy due to fluctuations is retained at the same value of $E(0) = 4 \times 10^{-6}$ as Fig. 4.8. However, in this case the linear and nonlinear evolutions diverge within a short period of time. The linear evolution exhibits a transient growth of a factor of 197 in the energy due to fluctuations until

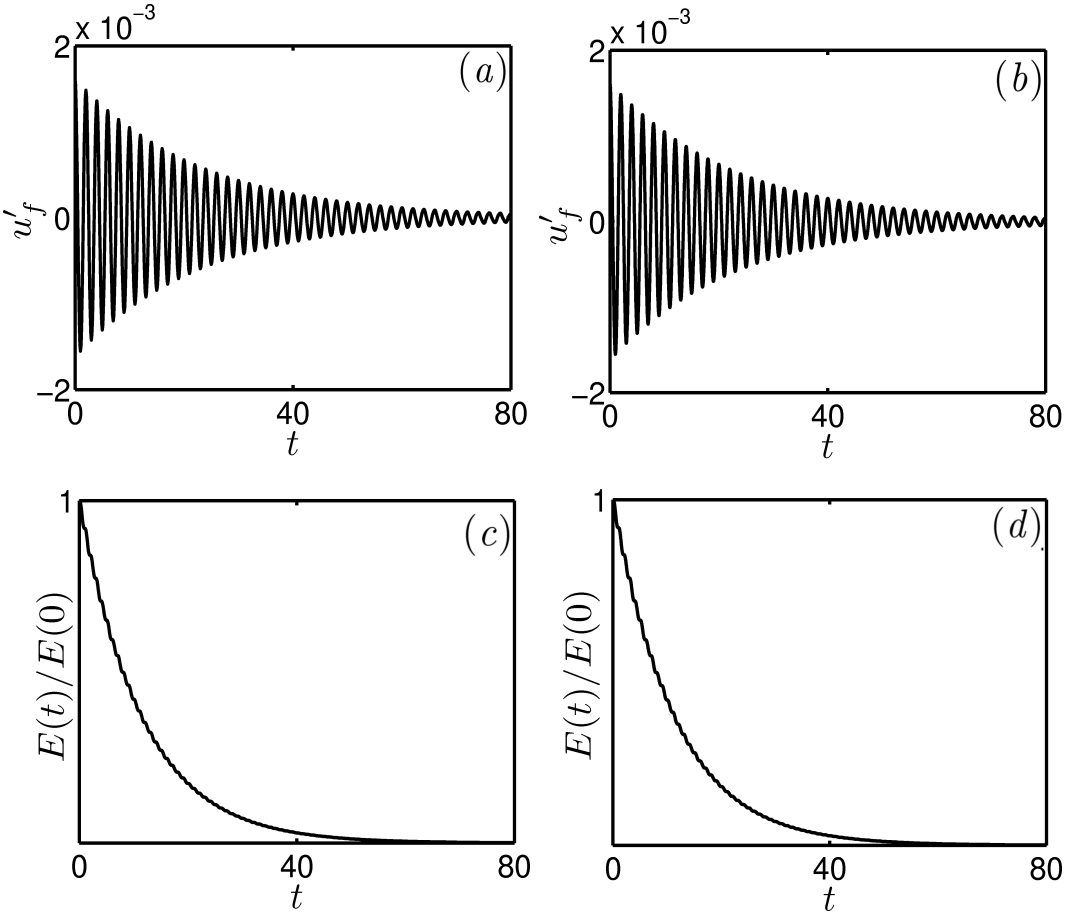

Figure 4.8: Evolution of acoustic velocity at the flame for (a) linearized system and (b) nonlinear system. Evolution of the normalized energy due to fluctuations $E(t)/E(0)$ for (c) linearized system and (d) nonlinear system. All evolutions are plotted along the acoustic time scale t. A purely acoustic initial condition with $u'_f(0) = 1.6 \times 10^{-3}$ and $E(0) = 4 \times 10^{-6}$ is seen to decay monotonically in both linear and nonlinear evolutions. The other system parameters are $\alpha = 10^0$, $y_f = 0.2$, $c_1 = 2 \times 10^{-3}$, $c_2 = 2 \times 10^{-4}$, $b/a = 0.5$, $\phi = 0.8$, $S_L = 0.2782$ m/s and $\triangle q_R = 2.2263 \times 10^6$ J/Kg.

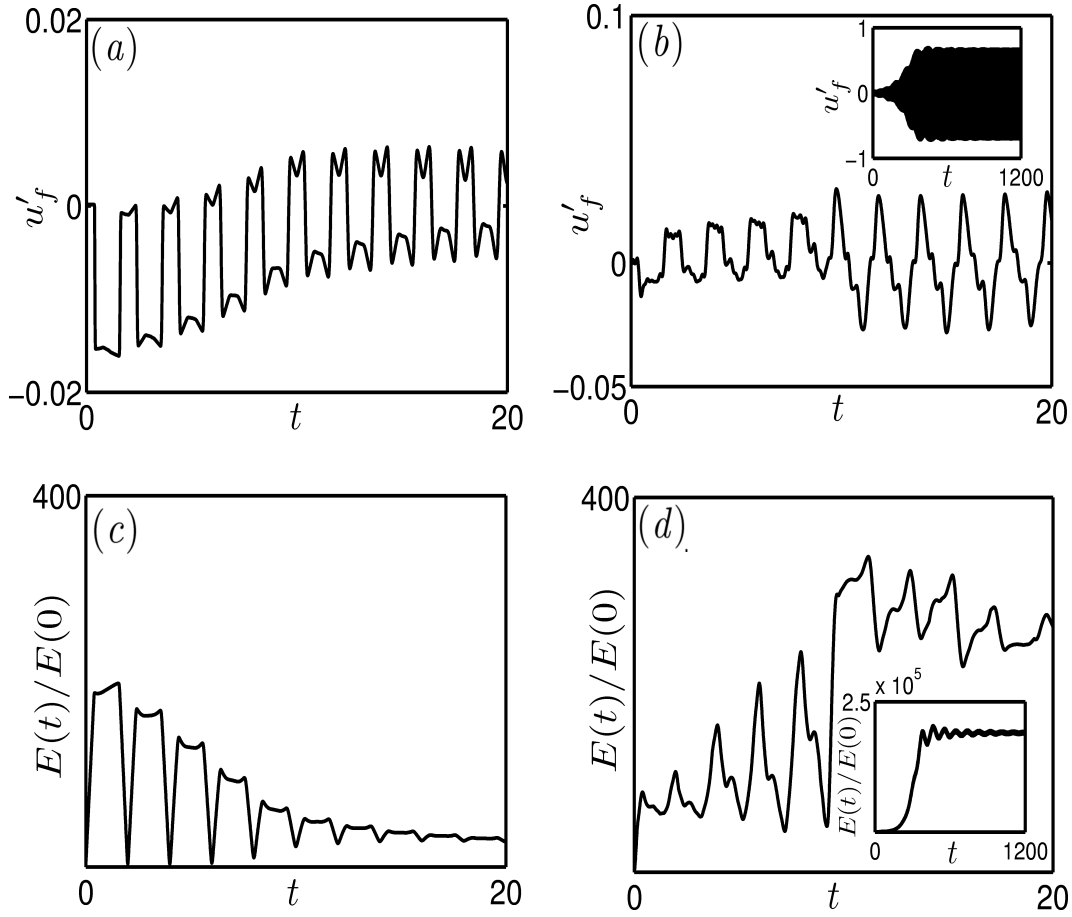

Figure 4.9: Evolution of acoustic velocity at the flame for (a) linearized system and (b) nonlinear system. Evolution of the energy due to fluctuations $E(t)/E(0)$ for (c) linearized system and (d) nonlinear system. All evolutions are plotted along the acoustic time scale t. The optimal initial condition with $u'_f(0) = 7.8 \times 10^{-5}$ and $E(0) = 4 \times 10^{-6}$ is seen to grow transiently and decay in the linear evolution. The nonlinear evolution reaches a limit cycle of amplitude $|u'_f|_{LC} = 0.67$. The other system parameters are $\alpha = 10^0$, $y_f = 0.2$, $c_1 = 2 \times 10^{-3}$, $c_2 = 2 \times 10^{-4}$, $b/a = 0.5$, $\phi = 0.8$, $S_L = 0.2782$ m/s and $\triangle q_R = 2.2263 \times 10^6$ J/Kg.

$t_{max} = 1.5$ and then asymptotically decays. Initially, the nonlinear evolution undergoes lesser transient growth than the linear evolution but asymptotically reaches a limit cycle with $|u'_f|_{LC} = 0.67$. This is seen from the insets in Figs. 4.9 (b & d).

From this example, it is evident that an initial condition with very small initial amplitude, if applied in an optimal manner, can cause transient growth in the energy of the system. If this transient growth is high enough for nonlinear effects to become significant, a system which is stable according to classical linear stability theory can become nonlinearly unstable. Therefore in non-normal systems, even initial perturbations

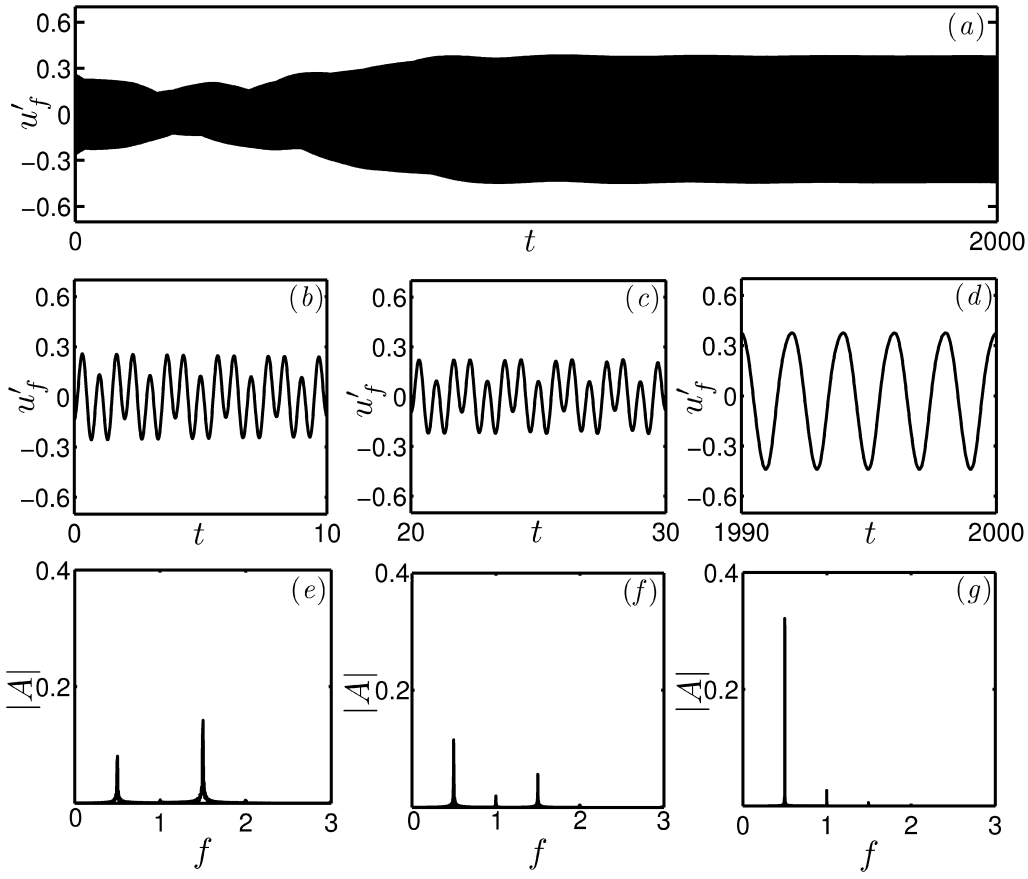

Figure 4.10: (a) Evolution of acoustic velocity with $u'_f(0) = -0.14$ to a limit cycle of amplitude $|u'_f|_{LC} = 0.41$ plotted along the acoustic time scale t. Enlarged views of acoustic velocity evolution between (b) $0 < t \leq 10$, (c) $20 < t \leq 30$ and (d) $1990 < t \leq 2000$. FFT of the signal between (e) $0 < t \leq 10$, (f) $10 < t \leq 30$ and (g) $30 < t \leq 2000$ showing change in the dominant frequency during evolution. System parameters for the linearly stable system are $\alpha = 10^0$, $y_f = 0.2$, $c_1 = 2 \times 10^{-3}$, $c_2 = 2 \times 10^{-4}$, $\phi = 0.6$, $S_L = 0.1231$ m/s and $\triangle q_R = 1.6885 \times 10^6$ J/Kg.

whose amplitude are small enough for linearization to appear apparently legitimate, can cause the nonlinear evolution to reach self-sustaining oscillations.

4.10 Evolution of an initially decaying system

Nonlinear evolution of acoustic velocity for a linearly stable system is shown in Fig. 4.10 (a). It shows an initial decay with a higher frequency and then a shift to a dominant mode of lower frequency. Despite the initial decay, the evolution reaches a self repeating limit cycle asymptotically. Analysis of the frequency content of the evolution

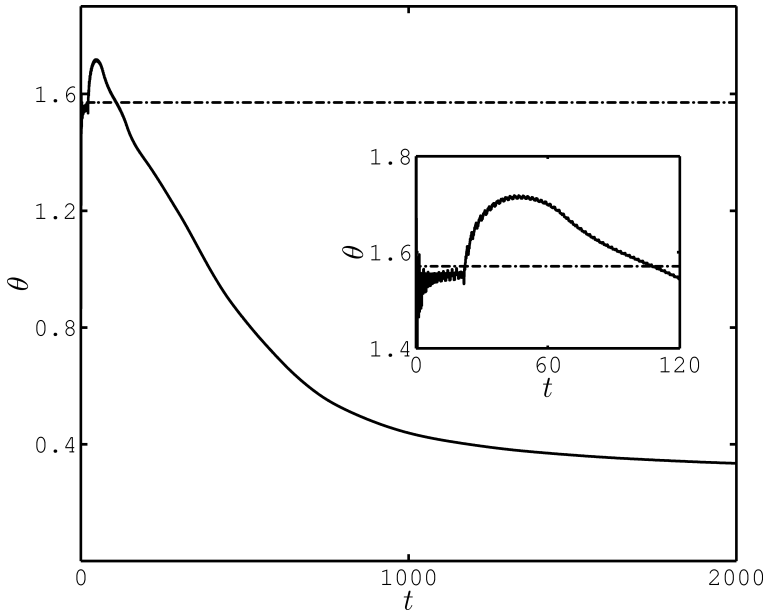

Figure 4.11: Evolution of phase angle θ between acoustic pressure and heat release rate fluctuations for linearly stable system with $\alpha = 10^0$, $y_f = 0.2$, $c_1 = 2 \times 10^{-3}$, $c_2 = 2 \times 10^{-4}$, $\phi = 0.6$, $S_L = 0.1231$ m/s and $\triangle q_R = 1.6885 \times 10^6$ J/Kg for the evolution shown in figure 4.10(a). Inset figure shows short term evolution of the phase angle θ. Evolutions are plotted along the acoustic time scale t.

during different intervals of time is performed in order to identify the dominant modes. Enlarged plots of the acoustic evolution are shown in Figs. 4.10 (b) to 4.10 (d).

Corresponding plots of amplitude $|A|$ versus frequency f are shown in Fig. 4.10(e) to Fig. 4.10 (g). Non-dimensional frequency for the fundamental mode of the duct is 0.5 with higher modes having multiples of this fundamental frequency. Figure 4.10 (e) shows that initially the third mode is dominant during time $0 < t \leq 10$. Comparable amplitudes for the first and the third mode are obtained for the evolution between $10 < t \leq 30$ in Fig. 4.10 (f) and then the first mode is seen to dominate the evolution from Fig. 4.10 (g). Transfer of energy between modes causes the shift in dominant mode during evolution.

The evolution of the phase θ between acoustic pressure and the heat release rate oscillations is shown in Fig. 4.11. In a self evolving thermoacoustic system, the phase between acoustic pressure and the heat release rate fluctuations is free to evolve and change with time. From the inset in Fig. 4.11, it is observed that θ initially remains at acute angles indicative of driving. However, it later evolves to obtuse angles, which is

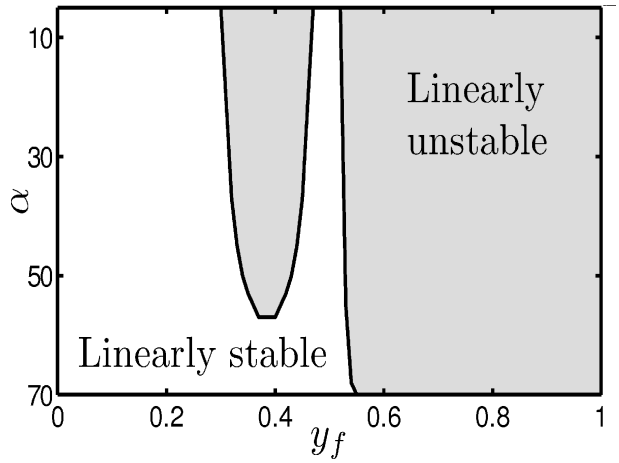

Figure 4.12: Linear stability boundary for the variation of angle of the flame α and the flame location y_f with the other parameters being $c_1 = 2 \times 10^{-3}$, $c_2 = 2 \times 10^{-4}$, $b/a = 0.5$ and $\phi = 0.6$.

indicative of damping and remains at these obtuse values for many cycles. Finally the evolution of the phase settles at an acute angle such that the driving from the unsteady heat release rate balances the damping present in the system as shown by the asymptotic behavior of the evolution of the phase. Phase between heat release rate fluctuations and acoustic pressure is therefore only an indicator of stability that is local in time and cannot be used to predict the asymptotic stability of the system.

4.11 Linear stability boundaries

The linear stability boundaries for the simultaneous variation of two system parameters are obtained using the classical linear stability analysis. When the flame location y_f and the flame angle α are varied, the linear stability boundary is as shown in Fig. 4.12. Grey areas indicate linearly unstable configurations. The laminar flame speed S_L, the flame angle α and the mean flow velocity $\bar{u}$ are related dimensionally as

$$\tilde{\bar{u}} \sin \alpha = S_L \,, \tag{4.54}$$

such that for a given ϕ, a variation in flame angle α translates to a variation in mean flow velocity $\tilde{\bar{u}}$. For an equivalence ratio of $\phi = 0.6$, the range of flame angles shown in Fig. 4.12 translates to mean velocities within the range $0.13 - 0.71\ m/s$. It is ob-

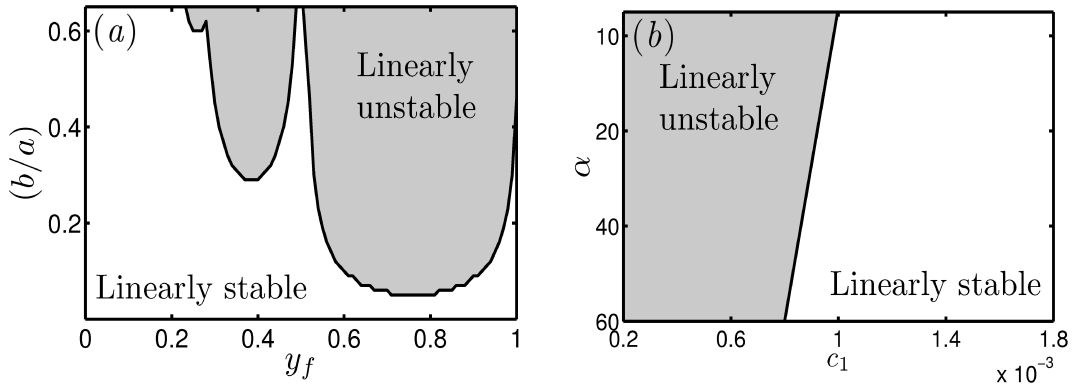

Figure 4.13: (a) Linear stability boundary for the ratio of burner to duct radius (b/a) and the flame location y_f with the other parameters being $\alpha = 10^0$, $c_1 = 2 \times 10^{-3}$, $c_2 = 2 \times 10^{-4}$ and $\phi = 0.6$. (b) Linear stability boundary for the variation of damping coefficient c_1 and the flame angle α with the other parameters being $\alpha = 10^0$, $y_f = 0.2$, $c_2 = 2 \times 10^{-4}$, $b/a = 0.5$ and $\phi = 0.8$.

served that a larger range of flame locations along the duct become unstable for sharper flame, i.e. smaller flame angles. This result is similar to the linear stability boundary determined for the Rijke tube system in Fig. 3.9.

Linear stability boundaries for the simultaneous variation of the heater location y_f with the burner to duct ratio (b/a) is given in Fig. 4.13 (a). It is observed that for low values of burner to duct ratio, the system is linearly stable for all locations along the duct. Low values for the burner to duct ratios indicate smaller fluctuations in heat release rate as related in the expression for Ω defined in Eqn. 4.20. Linear stability boundary for the simultaneous variation of the damping coefficient c_1 and the angle of the flame α is displayed in Fig. 4.13 (b). Increasing values of the damping coefficient stabilizes the system and the region of instability is larger for sharper flames which correspond to larger mean flow velocities.

4.12 Bifurcation plots from numerical continuation

Asymptotic state of the ducted premixed flame system is tracked for the variation of system parameters to obtain bifurcation plots. Initially a periodic solution for a given parameter value is determined by integrating the set of ordinary differential equations to obtain the evolution of state vector χ as a function of time. With this periodic solution

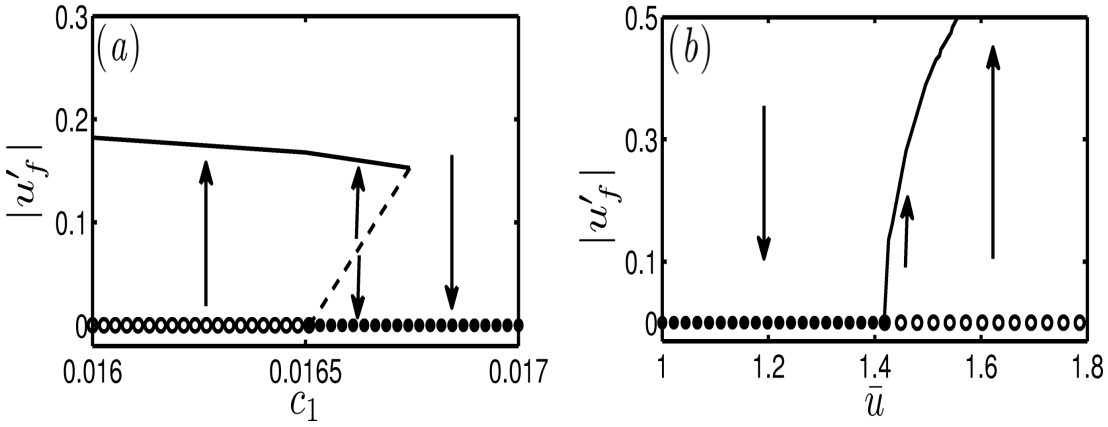

Figure 4.14: (a) Bifurcation plot for the variation of damping coefficient c_1 with other system parameters being $\alpha = 10^0$, $y_f = 0.7$, $c_2 = 1.5 \times 10^{-3}$, $\phi = 0.75$, $S_L = 0.2352$ m/s and $\triangle q_R = 2.0929 \times 10^6$ J/Kg. (b) Bifurcation plot for the variation of mean velocity $\bar{u}$ with other system parameters being $y_f = 0.25$, $c_1 = 2 \times 10^{-2}$, $c_2 = 1.5 \times 10^{-4}$, $\phi = 0.8$, $S_L = 0.2782$ m/s and $\triangle q_R = 2.2263 \times 10^6$ J/Kg. The solid line gives the amplitude of the stable limit cycles, dashed lines indicate unstable limit cycles, $\circ$ indicate unstable steady states and $\bullet$ are stable steady states.

as the initial guess, the asymptotic state of the system for smooth variations of the parameter from the initial value are obtained.

Application of the numerical continuation method described in Chapter 2 to systems becomes progressively expensive when the number of degrees of freedom in the system increase. In this section, numerical continuation is performed for a ducted premixed flame with with $N = 10$ and $P = 100$. This resolution of the system has relative errors $\Phi_{1,2}$ and $\Psi_{1,2}$ less than 10% for further increase in N and P as shown in Fig. 4.3. The results of continuation are shown in Figs. 4.14 (a & b). The measure chosen to display the asymptotic state in the bifurcation plots is the amplitude of acoustic velocity at the flame location $|u'_f|$.

Bifurcation plot for the variation of damping coefficient c_1 displays a hysteretic behavior as shown in Fig. 4.14 (a). Large values for the damping coefficient c_1 leads to linearly stable systems. Decreasing values of the damping coefficient destabilize the system through a sub-critical Hopf bifurcation followed by a fold bifurcation.

In another system configuration, a super-critical Hopf bifurcation is observed for the variation of mean flow velocity $\tilde{\bar{u}}$ as shown in Fig. 4.14 (b). The variation of the mean flow velocity is related to the laminar flame speed as described in Eqn. 4.54. The range

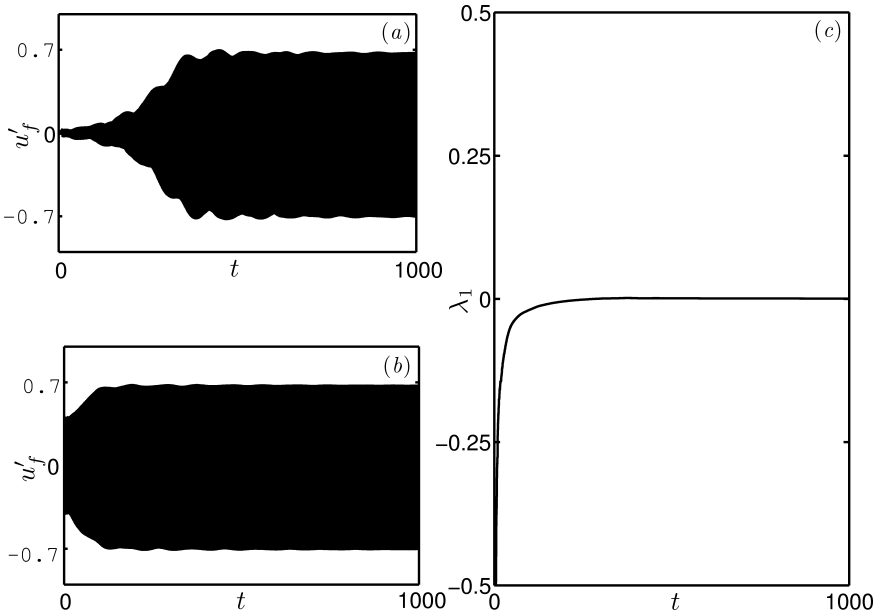

Figure 4.15: Nonlinear evolutions for $\alpha = 10^0$, $y_f = 0.2$, $c_1 = 2 \times 10^{-3}$, $c_2 = 2 \times 10^{-4}$, $\phi = 0.8$, $S_L = 0.2782$ m/s and $\triangle q_R = 2.2263 \times 10^6$ J/Kg for initial conditions with (a) Optimal initial condition with $u'_f(0) = 7.8 \times 10^{-5}$, (b) Initial condition with $u'_f(0) = 0.40$, (c) rate of separation of the two evolutions given in (a) and (b). All evolutions are plotted along the acoustic time scale t.

of flow velocities $\tilde{\bar{u}}$ shown in Fig. 4.14 (b) correspond to a variation in the equivalence ratio ϕ within the range $(0.67 - 0.84)$ when the flame angle α is fixed at 10^0. The occurrence of super-critical Hopf bifurcation is notable, as the Rijke tube model considered in Chapter 3 displays only sub-critical Hopf bifurcation as explained in Section 3.4.2.

4.13 On the asymptotic nature of evolutions

The ducted premixed flame system is observed to display self-sustained oscillations as shown in the inset of Fig. 4.9 (d). The asymptotic nature of the evolution needs to be characterized in order to classify the self-sustained oscillation into a limit cycle, quasi-periodic or chaotic oscillation. For the linearly stable system shown in Figs. 4.8 and 4.9, two nonlinear evolutions which differ only in the initial condition are shown in Figs. 4.15 (a & b).

The two evolutions evolve to the same limit cycle even when all eigenvalues are stable. This asymptotic behavior of the nonlinear evolution is characterized as a limit

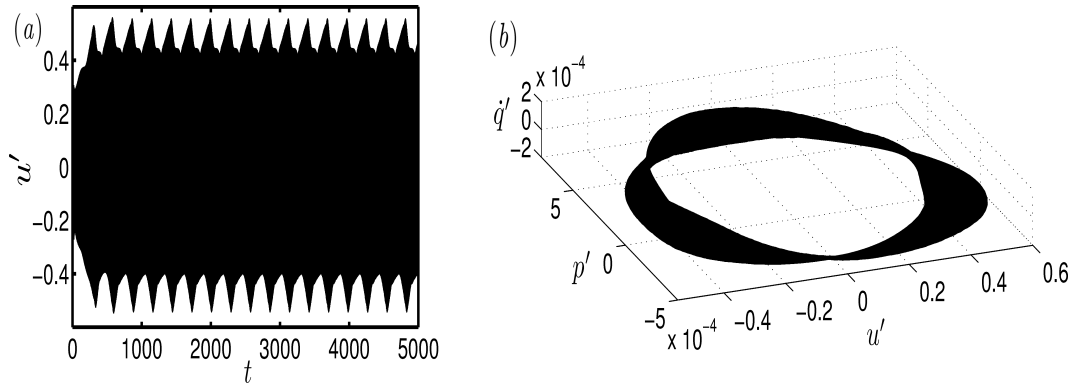

Figure 4.16: (a) Time evolution with periodically modulated evolution and (b) Phase plot of evolution showing a quasiperiodic orbit. The system parameters are $\alpha = 10^0$, $y_f = 0.7$, $c_1 = 2 \times 10^{-3}$, $c_2 = 2 \times 10^{-4}$, $b/a = 0.5$ and $\phi = 0.6$.

cycle using the Lyapunov exponent (Wolf *et al.*, 1985). The first Lyapunov exponent λ_1 is a measure of the rate at which two nearby trajectories asymptotically diverge from each other. A limit cycle is obtained when the value of λ_1 becomes zero. In Fig. 4.15 (c), it is observed that the value of λ_1 asymptotically reaches zero, which confirms that this asymptotic state is a limit cycle.

For the system parameters chosen in Fig. 4.12, the flame angle is fixed at $\alpha = 10^0$ and a flame location of $y_f = 0.7$ is chosen. The asymptotic nature of the evolution for this linear unstable system is evaluated. Time evolution of the acoustic velocity fluctuations displays a strongly modulated repeating evolution in Fig. 4.16 (a). A three-dimensional phase plot of the evolution is obtained by plotting the acoustic velocity u' and pressure p' along with the non-dimensional heat release rate fluctuations $\dot{q}'_f$. This phase plot is shown in Fig. 4.16 (b). The trajectory does not form a closed orbit but is seen to fill the surface of a torus. This indicates the quasiperiodic nature of the asymptotic state. Similar behavior has been observed in the Rijke tube model as shown in Fig. 3.10.

4.14 Summary

The non-normal nature of thermoacoustic interaction in ducted premixed flames is characterized. The unsteady heat release rate from the flame front acts as a source of un-

steady dilatation. Therefore the laminar flame front is modeled as a distribution of monopole sources of sound. The energy due to fluctuations in the premixed flame-acoustic system includes the energy due to the monopole sources in addition to the fluctuations in acoustic pressure and velocity. This total energy due to fluctuations is used as a measure of non-normal transient growth. Parametric study of the variation in transient growth due to change in parameters such as flame angle and flame location is conducted. Larger transient growth is observed when convective effects dominate.

Traditionally, thermoacoustic instabilities have been analyzed in terms of an acoustic model which is driven by combustion. However, the thermoacoustic system has more degrees of freedom than the number of acoustic modes. These additional degrees of freedom represent the internal degrees of freedom of the flame front which we refer to as the internal flame dynamics. In addition to the acoustic variables, the optimal initial condition for a linearly stable thermoacoustic system displays significant projections along the monopole source strength distribution or the heat release rate variables. In order to accurately capture the non-normal effects, the internal degrees of the flame front must be accounted for in the model for the evolution of the thermoacoustic system.

Sub-critical transition to instability has been thought of as being caused by a large amplitude initial perturbation to a linearly stable system. In a linearly stable case, even a small but finite amplitude initial perturbation is shown to reach limit cycle. In contrast, for the same thermoacoustic system an initial condition purely in acoustic variables is seen to monotonically decay. Therefore for non-normal systems, even initial perturbations whose amplitudes are small enough for linearization to appear apparently legitimate, can cause the nonlinear evolution to reach self-sustaining oscillations.

Nonlinear evolutions can display dominant mode change during the evolution in a linearly stable case when the evolution initially decays. For this initially decaying evolution, the phase between acoustic pressure and the heat release rate fluctuations was shown to drift over many cycles between values indicative of driving and damping before settling to a constant value. Therefore, the phase between acoustic pressure and heat release rate fluctuations is an indicator of stability that is local in time and cannot be used to determine the asymptotic stability of a thermoacoustic system.

The linear stability boundary for the simultaneous variation of different system parameters were obtained. It was observed that smaller flame angles, low values for the damping coefficient and larger values for the burner to duct ratio cause the system to become linearly unstable. Bifurcation plots for the variation of system parameters has been obtained by the method of numerical continuation. The ducted premixed flame model exhibits both sub- and super-critical Hopf bifurcations. The asymptotic nature of the evolutions was investigated for different system configurations and behavior such as limit cycle and quasiperiodic states were observed.

CHAPTER 5

CONCLUSIONS & FUTURE WORK

5.1 Conclusions

Investigations of stability in thermoacoustic systems have largely been focussed on modal analysis. Both the linear and nonlinear modal stability analyses do not capture transients in the system. Inability to account for the transient effects can lead to erroneous stability predictions for the thermoacoustic system. Time domain models account for the transients in the system and are used in the present work. Time domain models for two typical thermoacoustic systems are chosen for stability analysis: (1) an electrically heated Rijke tube and (2) a ducted premixed flame. In the Rijke tube, the source of heat release rate oscillations is modelled using a correlation between acoustic velocity fluctuations and the unsteady heat release rate which contains an explicit time delay. For the ducted premixed flame, the unsteady heat release rate is modelled using an evolution equation for a premixed flame front, known as *G*-equation. These models for the unsteady heat release rate can be coupled to the differential equations governing the acoustic field within the duct, to model the coupled thermoacoustic system. The present analysis adopts methods and tools from dynamical systems' theory to determine both the linear and nonlinear stability of thermoacoustic systems.

In the present work, numerical continuation method was implemented to determine the bifurcation plots for a Rijke tube system and a ducted premixed flame system. The present thesis is the first work in which numerical continuation methods have been applied to the investigation of thermoacoustic systems with an explicit time delay. Both the Rijke tube and ducted premixed flame systems display Hopf bifurcations beyond which the system exhibits periodic oscillations. Sub-critical Hopf bifurcations are observed in the Rijke tube system while both sub- and super-critical Hopf bifurcations occur in the ducted premixed flame system. It is shown that only sub-critical bifurcations

are possible for the model of Rijke tube considered in this thesis. In both the thermoacoustic systems considered, a higher heater power or larger mean flow causes increased acoustic driving which destabilizes the system. Also, increased acoustic damping is seen to stabilize the systems. Non-monotonic stability changes are observed when the location of unsteady heat release rate is varied. Analytical and numerical methods from dynamical systems' theory have been employed to characterize regions of global stability, bistability and global instability in thermoacoustic systems. The present work demonstrates the feasibility of employing numerical continuation method to determine both the linear and nonlinear stability of thermoacoustic systems in a unified framework. Numerical continuation can be employed to identify the safe ranges of operation in gas turbines and rocket motors, in order to avoid instabilities.

Previous works consider that the asymptotic state during instability is a limit cycle whose amplitude is determined by the balance of acoustic driving and damping in the system. In the present work, a variety of alternate asymptotic states are observed such as period-2, period-4, quasiperiodic and chaotic oscillations. This is in agreement with the recent findings of Kabiraj *et al.* (2010). It is observed multiple attractors can coexist and that a system could reach any one of the asymptotic states depending on the initial perturbation. Further, it is observed that finite time transient growth can play a role in determining the asymptotic state to which a system evolves.

In order to characterize the transient growth in a system, the energy due to fluctuations is chosen as a measure or norm. The chosen measure should account for contributions from all the state variables. This ensures that all the relevant constituent phenomena in the system, represented by the state variables, are included in the measure. There is no common consensus in the literature, on the appropriate expression for energy due to fluctuations in compressible reacting flows. Therefore, there is a need to define an appropriate disturbance energy for the ducted premixed flame system. A measure for the energy due to fluctuations in a ducted premixed flame is derived in the present thesis. As the unsteady heat addition acts as a volumetric source, the premixed flame front is modelled as a distribution of monopole sources. The energy due to fluctuations considered in this analysis accounts for the energy of the monopole sources in addition to the acoustic energy. This measure is used to characterize the transient

growth in ducted premixed flame system.

Transient growth observed in a non-normal system depends on the distribution of initial perturbation among the different state variables. Optimal initial conditions which cause maximum transient growth, can be identified using singular value decomposition for each system configuration. These optimal initial conditions have significant projections along the monopole source strength distribution. This is evident from the considerably larger transient growth observed for the optimal initial condition when compared with a purely acoustic initial condition. In a ducted premixed flame, larger transient growth is identified with system configurations where convective terms dominate the evolution, i.e. for sharper flames located near the half duct length. Identification of system configurations with large transient growth is important in investigating the role of transient growth in causing sub-critical transition to instability.

Traditionally, sub-critical transition to instability or triggering, has been thought to be caused by a finite amplitude disturbance to a linearly stable system. However, even a small but finite amplitude perturbation can cause triggering in non-normal systems. In a linearly stable case for the ducted premixed flame system, a small but finite amplitude optimal initial perturbation reaches a limit cycle while an initial condition purely in the acoustic variables with the same energy is seen to monotonically decay. Therefore in non-normal systems, even initial perturbations whose amplitudes are small enough for linearization to appear apparently legitimate, can cause the nonlinear evolution to reach self-sustaining oscillations.

The criterion for the occurrence of instability in thermoacoustic systems requires that the phase angle θ between the acoustic pressure and unsteady heat release rate lies between the range which indicates acoustic driving, i.e. $-90^\circ < \theta < 90^\circ$. The acoustic driving due to unsteady heat release rate oscillations must overcome the acoustic damping in the thermoacoustic system in order to cause instability. A linearly stable system configuration is chosen for the ducted premixed flame. An initially decaying nonlinear evolution, which asymptotically evolves to a limit cycle is considered. During the nonlinear evolution, the dominant mode of oscillation changes with time. The phase between acoustic pressure and the heat release rate fluctuations during such a nonlinear evolution is seen to drift between values indicative of driving and damping before set-

tling to a constant value as the evolution reaches a limit cycle. This drift occurs over many cycles of oscillations. Therefore, the phase between acoustic pressure and heat release rate fluctuations is an indicator of stability that is local in time and cannot be used to determine the asymptotic stability of a thermoacoustic system.

In summary, the thesis of the present work proposes that, a non-modal approach to the stability analysis is necessary to characterize the stability of thermoacoustic systems accurately and that tools from dynamical systems' theory can be used effectively to determine both the linear and nonlinear stability of thermoacoustic systems.

5.2 Scope of future work

Stability analysis of thermoacoustic systems is commonly performed using modal analysis methods. This approach does not account for the transient effects in the system. However, the present thesis establishes that it is essential to account for transient growth in the system, in order to accurately capture the asymptotic stability of thermoacoustic systems. In future, low order models of both linear and nonlinear systems can be obtained using linear and nonlinear system identification techniques. The identified low order models can then be used to determine stability of the system accounting for transient growth due to non-normality.

In the present thesis, optimal initial perturbations are identified for the ducted premixed flame system through singular value decomposition of the linear operator. If the variables of the state vector are chosen such that the square of its 2-norm equals the energy due to fluctuations, maximal amplification occurs when the initial perturbation is along the first right singular vector. This method of singular value decomposition cannot be used to obtain the optimal initial condition if the energy due to fluctuations cannot be written as the square of the 2-norm of the state vector. Also, the optimal initial condition obtained from singular value decomposition ensures maximum amplification during the evolution of a linear system. The optimal initial condition for the nonlinear system can be significantly different. The method of singular value decomposition cannot be employed to obtain the nonlinear optimal initial condition. In order to handle the

above mentioned two scenarios, the variational technique of adjoint optimization can be used to identify both the linear and nonlinear optimal initial condition of a system. Future work can focus on obtaining the nonlinear optimal initial condition of the ducted premixed flame system using adjoint optimization technique to compare it with the linear optimal initial condition obtained from singular value decomposition in the present work.

Numerical continuation was employed to obtain stability boundaries and bifurcation plots for the reduced order models of the Rijke tube system and ducted premixed flame system in the present thesis. The bulk of computation time during continuation is utilized to determine the Jacobian and monodromy matrices. Continuation methods which can reduce the time taken for this calculation or bypass this step will be more efficient and would be capable of determining bifurcation plots faster than conventional continuation methods. Matrix free methods in continuation bypass the determination of the Jacobian matrix completely and are therefore efficient. The acceleration in computational time achieved can also make it possible to perform continuation for systems with larger number of degrees of freedom. In future, the application of matrix free continuation methods to the bifurcation analysis of thermoacoustic systems can be explored.

APPENDIX A

Loss of linear stability

Loss of linear stability occurs when a root of Eqn. (3.18) acquires a positive real part. When the heater is located in the first half of the duct, i.e. $0 < y_f < 0.5$, $\lambda = 0$ will never satisfy Eqn. (3.18). Therefore, static bifurcations such as trans-critical, pitchfork and saddle-node bifurcations cannot occur (Strogatz, 2000). Thus, when the heater is placed in the first half of the duct, the steady state becomes unstable only through a Hopf bifurcation. The parameter value at which the Hopf bifurcation occurs can be obtained as illustrated in Section 3.4.1.

When the heater is located in the second half of the duct, i.e. $0.5 < y_f < 1$, the condition $\lambda = 0$ gives the following relation:

$$\triangle(0, \tau) = a_1 + a_2 = 0 \tag{A.1}$$

The following relation between the non-dimensional power K_S required to destabilize the system through a static bifurcation and the heater location y_f is derived with the constants $a_1 = \pi^2$ and $a_2 = \sqrt{3}k\pi/4\sin(2\pi y_f)$ as in Section 3.4.1.

$$K_S = -\frac{4\pi}{\sqrt{3}\sin(2\pi y_f)} \tag{A.2}$$

Similarly, for any heater location in the range $(0.5 < y_f < 1)$, the non-dimensional power K_{H1} required for a Hopf bifurcation can be derived from equation is given as below:

$$K_{H1} = \left(\frac{16(\omega_1^4 + (a_0^2 - 2a_1)\omega_1^2 + a_1^2)}{3\pi^2 \sin^2(2\pi y_f)}\right)^{1/2}; \tag{A.3}$$

In the above expression, we set $\omega_1 = \pi$ in order to approximate the value of K_{H1}. From the figure A.1, we see that the power required for the Hopf bifurcation K_{H1} is much lower than that required for a static bifurcation K_S. Therefore, it is concluded in

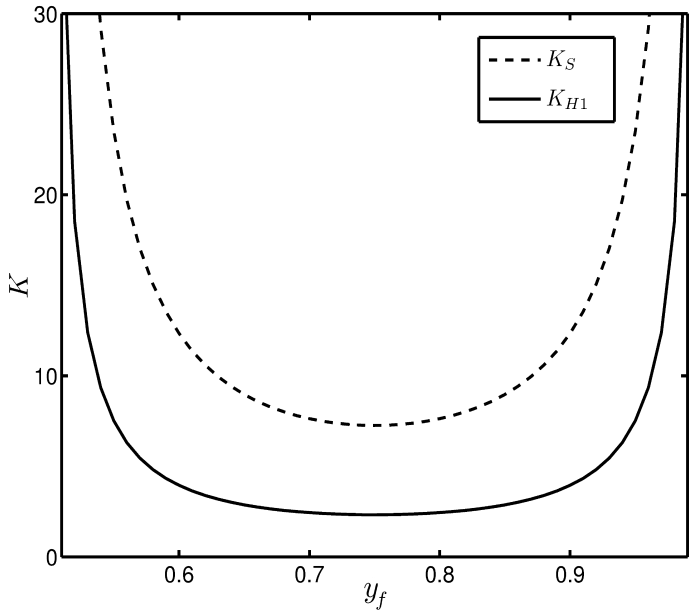

Figure A.1: Comparison of analytical linear stability boundaries for a static or dynamic bifurcation as a function of non-dimensional heater power and heater location. Solid line gives the minimum power required for a dynamic bifurcation K_{H1} and the dashed line gives the minimum power required for a static bifurcation K_S. Common parameters are $c_1 = 0.1$, $c_2 = 0.06$. This result is independent of time lag.

the present model that loss of linear stability occurs only through a Hopf bifurcation. Since both the expressions in Eqns. (A.2) and (A.3) do not involve time lag τ, the above conclusion is valid independent of the value of τ.

APPENDIX B

Expressions for slow flow equations

The expressions for the coefficients of the slow flow amplitude equation B_1 and B_2 as given in Eqn. (3.38) are expanded below:

$$B_1 = \frac{N_1}{D} \quad \text{and} \quad B_2 = \frac{N_3}{D}\,, \tag{B.1}$$

where the denominator D, the numerator for the first order term N_1 and for the third order term N_3 are as given below.

$$\begin{aligned}
D = {} & 512\omega^2\left[\Delta_c^3 + \Delta_c^2\pi^2 + \Delta_c\pi^4 + \pi^6 + 2\cos(2\omega\tau)\left[\pi^4\Delta_c + \pi^2\Delta_c^2\right]\right] \\
& + 512\omega\tau\left[\sin(\omega\tau)\left[\pi^6\Delta_c + \Delta_c^4\right] + \sin(3\omega\tau)\left[\pi^2\Delta_c^3 + \pi^4\Delta_c^2\right]\right] \\
& + 128\left[\zeta_1^2[\pi^2\Delta_c^2 + \pi^4\Delta_c + \pi^6 + \Delta_c^3] + \tau^2[\Delta_c^5 + \pi^4\Delta_c^3 + \pi^6\Delta_c^2 + \pi^2\Delta_c^4]\right] \\
& - 256\tau\zeta_1\cos(\omega\tau)\left[\pi^6\Delta_c + \Delta_c^4 + 2\pi^4\Delta_c^2 + 2\pi^2\Delta_c^3\right] \\
& + 256\cos(2\omega\tau)\left[\zeta_1^2[\pi^4\Delta_c + \pi^2\Delta_c^2] + \tau^2[\pi^4\Delta_c^3 + \pi^2\Delta_c^4]\right] \\
& - 256\tau\zeta_1\cos(3\omega\tau)\left[\pi^2\Delta_c^3 + \pi^4\Delta_c^2\right] \quad ,
\end{aligned} \tag{B.2}$$

$$\begin{aligned}
N_1 = {} & 256\omega\left[\sin(\omega\tau)\left[\pi^6 + \Delta_c^3\right] + \sin(3\omega\tau)\left[\pi^4\Delta_c + \pi^2\Delta_c^2\right]\right] \\
& + 128\delta\tau\left[\pi^6\Delta_c + \pi^4\Delta_c^2 + \pi^2\Delta_c^3 + \Delta_c^4\right] \\
& - 128\delta\zeta_1\cos(\omega\tau)\left[\pi^6 + \Delta_c^3 - 2[\pi^4\Delta_c + \pi^2\Delta_c^2]\right] \\
& + 256\delta\tau\cos(2\omega\tau)\left[\pi^4\Delta_c^2 + \pi^2\Delta_c^3\right] \\
& - 128\delta\zeta_1\cos(3\omega\tau)\left[\pi^2\Delta_c^2 + \pi^4\Delta_c\right] \quad ,
\end{aligned} \tag{B.3}$$

$$
\begin{aligned}
N_3 = 9\omega[&[6\pi^6\Delta_c + 2\pi^2\Delta_c^3 - 4\pi^4\Delta_c^2]\left(\sin\left(2\pi y_f + \omega\tau\right) - \sin\left(2\pi y_f - \omega\tau\right)\right) \\
&+ 4\pi^4\Delta_c^2\left(\sin\left(2\pi y_f + 3\omega\tau\right) - \sin\left(2\pi y_f - 3\omega\tau\right) + 2\sin\left(3\omega\tau\right)\right) \\
&+ 4\sin\left(\omega\tau\right)[\pi^2\Delta_c^3 - 2\pi^4\Delta_c^2 + 3\pi^6\Delta_c]] \\
&- 9\zeta_1\cos\left(\omega\tau\right)[8\pi^4\Delta_c^2 + 6\pi^2\Delta_c^3 + 6\pi^6\Delta_c] \\
&+ 9\tau\cos\left(2\omega\tau\right)[2\pi^2\Delta_c^4 + 10\pi^4\Delta_c^3] - 36\zeta_1\cos\left(3\omega\tau\right)\pi^4\Delta_c^2 \\
&+ 9\tau[2\pi^4\Delta_c^3 + 6\pi^6\Delta_c^2 + 4\pi^2\Delta_c^4]\left(1 + \cos\left(2\pi y_f\right)\right) \\
&- 9\zeta_1[3\pi^2\Delta_c^3 + 3\pi^6\Delta_c + 4\pi^4\Delta_c^2]\left(\cos\left(2\pi y_f + \omega\tau\right) + \cos\left(2\pi y_f - \omega\tau\right)\right) \\
&+ 9\tau[\pi^2\Delta_c^4 + 5\pi^4\Delta_c^3]\left(\cos\left(2\pi y_f + 2\omega\tau\right) + \cos\left(2\pi y_f - 2\omega\tau\right)\right) \\
&- 18\zeta_1\pi^4\Delta_c^2\left(\cos\left(2\pi y_f + 3\omega\tau\right) + \cos\left(2\pi y_f - 3\omega\tau\right)\right)
\end{aligned}
\tag{B.4}
$$

APPENDIX C

WENO scheme

The high resolution WENO scheme uses a six point stencil formed of three sub-stencils each with four points. It will therefore give fifth order accuracy in the smooth regions and third order accuracy in the discontinuous regions. Implementation of WENO assumes that the function $\xi'(X,t)$ is continuous, with piece-wise smooth spatial derivatives; i.e. the discontinuities in the spatial derivative are isolated. The domain can then be discretised with X_i being the set of uniform discretisation points along the flame front with an equidistant spacing of $\triangle X$. If, $\xi_i = \xi(X_i)$ and

$$\Delta^+\xi_k = \xi_{k+1} - \xi_k; \Delta^-\xi_k = \xi_k - \xi_{k-1}\,, \tag{C.1}$$

are as defined above, then the approximation for the spatial derivative at the i^{th} location using a left biased stencil which is written in (C.2) and is given by a weighted average of the values due to the individual stencils 0, 1 and 2 shown in (C.3).

$$\frac{\partial \xi'}{\partial X} = \xi^-_{X,i}\,, \tag{C.2}$$

$$\xi^-_{X,i} = w_{0,NL}\xi^{-,0}_{X,i} + w_{1,NL}\xi^{-,1}_{X,i} + w_{2,NL}\xi^{-,2}_{X,i}\,, \tag{C.3}$$

with

$$\xi^{-,0}_{X,i} = \frac{1}{3}\frac{\Delta^+\xi_{i-3}}{\Delta X} - \frac{7}{6}\frac{\Delta^+\xi_{i-2}}{\Delta X} + \frac{11}{6}\frac{\Delta^+\xi_{i-1}}{\Delta X}\,, \tag{C.4}$$

$$\xi^{-,1}_{X,i} = -\frac{1}{6}\frac{\Delta^+\xi_{i-2}}{\Delta X} + \frac{5}{6}\frac{\Delta^+\xi_{i-1}}{\Delta X} + \frac{1}{3}\frac{\Delta^+\xi_i}{\Delta X}\,, \tag{C.5}$$

$$\xi^{-,2}_{X,i} = \frac{1}{3}\frac{\Delta^+\xi_{i-1}}{\Delta X} + \frac{5}{6}\frac{\Delta^+\xi_i}{\Delta X} - \frac{1}{6}\frac{\Delta^+\xi_{i+1}}{\Delta X}\,, \tag{C.6}$$

where $\xi^{-,s}_{X,i}$ is the third order approximation to $\xi^-_{X,i}$ on the s^{th} sub-stencil. In an ENO scheme, one of the $\xi^{-,s}_{X,i}$ would be chosen based on the relative smoothness of the sub-

stencil. The nonlinear weight of the derivative calculated in a sub-stencil, depends on the smoothness of the function derivative in that sub-stencil. The modified smoothness indicators are given in (C.7)-(C.9) (Jiang and Shu, 1996; Zhang and Shu, 2007):

$$IS_0 = \left(\xi_{i-2} - 4\xi_{i-1} + 3\xi_i\right)^2 , \tag{C.7}$$

$$IS_1 = \left(\xi_{i-1} - \xi_{i+1}\right)^2 , \tag{C.8}$$

$$IS_2 = \left(3\xi_i - 4\xi_{i+1} + \xi_{i+2}\right)^2 , \tag{C.9}$$

which are then used to calculate the nonlinear weights as given below, with typical values for $p = 2$ and $\epsilon = 10^{-6}$,

$$\mu_s = \frac{w_{s,L}}{(\varepsilon + IS_s)^r} , \tag{C.10}$$

$$w_{s,NL} = \frac{\mu_s}{\sum_{s=0}^{2} \mu_s} . \tag{C.11}$$

Here the linear weights $w_{s,L}$ for the s^{th} sub-stencil at point are made to satisfy the consistency condition, such that

$$\sum_{s=0}^{2} w_{s,L} = 1 . \tag{C.12}$$

When the linear weights are $w_{0,L} = 0.3$; $w_{1,L} = 0.6$; $w_{2,L} = 0.1$, we obtain the fifth order accurate solution in the smooth regions. While using WENO with a left biased stencil, we require derivative values for the first three points and the last two points. The appropriate fifth order accurate explicit scheme is used to calculate the first derivative of the function values at boundary cells (Zhong, 1998).

APPENDIX D

Linear operator

If the matrix governing the linearized thermoacoustic system as given in the set of Eqns. (4.41), (4.44) and (4.46) is, they can be written as given in equation (D.1) for the state vector χ in equation (D.2). Then the sub-matrices can be expanded as given in (D.3) to (D.6):

$$\mathrm{B} = \begin{pmatrix} C_{2N\times 2N} & D_{2N\times P} \\ E_{P\times 2N} & F_{P\times P} \end{pmatrix}_{(2N+P)\times(2N+P)}, \tag{D.1}$$

$$\chi = \begin{pmatrix} \eta_1 \\ (-\dot{\eta}_1/\pi) \\ \eta_2 \\ (-\dot{\eta}_2/2\pi) \\ . \\ . \\ (-\dot{\eta}_N/N\pi) \\ H_1 \\ H_2 \\ . \\ . \\ H_P \end{pmatrix}_{(2N+P)\times 1}, \tag{D.2}$$

$$C = \begin{pmatrix} 0 & -\pi & . & . & . & . & . & . \\ \pi & -2\zeta_1 k_1 & . & . & . & . & . & . \\ . & . & 0 & -2\pi & . & . & . & . \\ . & . & 2\pi & -2\zeta_2 k_2 & . & . & . & . \\ . & . & . & . & . & . & . & . \\ & & & & & & 0 & -N\pi \\ . & . & . & . & & . & N\pi & -2\zeta_N k_N \end{pmatrix}_{2N\times 2N}, \tag{D.3}$$

$$D = \sqrt{2}\begin{pmatrix} 0 & 0 & . & . & 0 \\ 0 & \sin(\pi y_f) & . & . & 2\sin(\pi y_f) \\ 0 & 0 & . & . & 0 \\ 0 & \sin(2\pi y_f) & . & . & 2\sin(2\pi y_f) \\ 0 & 0 & . & . & 0 \\ 0 & \sin(3\pi y_f) & . & . & 2\sin(3\pi y_f) \\ 0 & 0 & . & . & 0 \\ . & . & . & . & . \\ . & . & . & . & . \\ 0 & 0 & . & . & 0 \\ 0 & \sin(N\pi y_f) & . & . & 2\sin(N\pi y_f) \end{pmatrix}_{2N\times P} , \tag{D.4}$$

$$E = \begin{pmatrix} 0 & 0 & 0 & 0 & . & . & 0 & 0 \\ \theta_1 cos(\pi y_f) & 0 & \theta_1 cos(2\pi y_f) & 0 & . & . & \theta_1 cos(N\pi y_f) & 0 \\ . & . & . & . & . & . & . & . \\ . & . & . & . & . & . & . & . \\ \theta_1 cos(\pi y_f)/2 & 0 & \theta_1 cos(2\pi y_f)/2 & 0 & . & . & \theta_1 cos(N\pi y_f)/2 & 0 \end{pmatrix}_{P\times 2N} , \tag{D.5}$$

$$F = \begin{pmatrix} 0 & . & . & . & . & . & . & . \\ 0 & -\theta_2 & . & . & . & . & . & . \\ . & \theta_2 & -\theta_2 & . & . & . & . & . \\ . & . & \theta_2 & -\theta_2 & . & . & . & . \\ . & . & . & . & . & . & . & . \\ . & . & . & . & . & . & . & . \\ . & . & . & . & . & . & \theta_2 & -\theta_2 \end{pmatrix}_{P\times P} . \tag{D.6}$$

Here H_i corresponds to the monopole strength averaged over the cross-sectional area of the duct and the values of constants θ_1 and θ_2 are defined in equation (4.46). The spatial derivative is approximated with the first order backward difference formula and the integration for the source term is approximated with a trapezoidal integration over all points along the flame front.

REFERENCES

1. **Abarbanel, H. D. I.**, *Analysis of observed Chaotic data*. Springer, New York, 1996.

2. **Ajjarapu, V.**, *Computational techniques for voltage stability assessment and control*. Springer, New York, 2006.

3. **Allgower, E. L.** and **K. Georg**, *Introduction to Numerical Continuation Methods*. Society for Industrial and Applied Mathematics, Philadelphia, 2003.

4. **Ananthkrishnan, N.**, **S. Deo**, and **F. E. C. Culick** (2005). Reduced-order modeling and dynamics of nonlinear acoustic waves in a combustion chamber. *Combustion Science and Technology*, **177**, 221–248.

5. **Annaswamy, A. M.**, **M. Fleifil**, **J. P. Hathout**, and **A. F. Ghoneim** (1997). Impact of linear coupling on the design of active controllers for the thermoacoustic instability. *Combustion Science & Technology*, **128**, 131–180.

6. **Astrom, K. J.** and **T. Hagglund**, *PID Controllers: Theory, Design and Tuning, Second Edition*. Research Triangle Park, North Carolina, 1995.

7. **Atchley, A. A.** (1992). Standing wave analysis of a thermoacoustic prime mover below onset of self-oscillation. *Journal of Acoustical Society of America*, **92**, 2907–2914.

8. **Bakas, N. A.** (2009). Mechanisms underlying transient growth of planar perturbations in unbounded compressible shear flow. *Journal of Fluid Mechanics*, **639**, 479–507.

9. **Baker, G. L.** and **J. P. Gollub**, *Chaotic Dynamics: an Introduction*. Cambridge University Press, Cambridge, 1990.

10. **Balasubramanian, K.** and **R. I. Sujith** (2008*a*). Non-normality and nonlinearity in combustion-acoustic interaction in diffusion flames. *Journal of Fluid Mechanics*, **594**, 29–57.

11. **Balasubramanian, K.** and **R. I. Sujith** (2008*b*). Nonlinear response of diffusion flames to uniform velocity disturbances. *Combustion Science & Technology*, **180**, 418–436.

12. **Balasubramanian, K.** and **R. I. Sujith** (2008*c*). Thermoacoustic instability in a Rijke tube: Non-normality and nonlinearity. *Physics of Fluids*, **20**, 044103.

13. **Birbaud, A. L.**, **D. Durox**, and **S. Candel** (2006). Upstream flow dynamics of a laminar premixed conical flame submitted to acoustic modulations. *Combustion & Flame*, **146**, 541–552.

14. **Bittani, S.**, **A. D. Marco**, **G. Poncia**, and **W. Prandoni** (2002). Identification of a model for thermoacoustic instabilities in a Rijke tube. *IEEE Transactions on control systems technology*, **10**, 490–502.

15. **Bloomshield, F. S.**, **J. E. Crump**, **H. B. Mathes**, **R. A. Stalnaker**, and **M. W. Beckstead** (1997). Nonlinear stability testing of full scale tactical motors. *Journal of Propulsion & Power*, **13**(3), 356–366.

16. **Bloxsidge, G. J.**, **A. P. Dowling**, and **P. J. Langhorne** (1988). Reheat buzz: an acoustically coupled combustion instability. part 2. theory. *Journal of Fluid Mechanics*, **193**, 445–473.

17. **Bottaro, A.**, **P. Corbett**, and **P. Luchini** (2003). The effect of base flow variation on flow stability. *Journal of Fluid Mechanics*, **476**, 293–302.

18. **Boyer, L.** and **J. Quinard** (1990). On the dynamics of anchored flames. *Combustion Science & Technology*, **82**, 51–65.

19. **Buckmaster, J.** (2002). Edge flames. *Progress in Energy and Combustion Science*, **28**, 435–475.

20. **Burke, S. B.** and **T. E. W. Schumann** (1928). Diffusion flames. *Industrial & Engineering Chemistry*, **20**, 998–1004.

21. **Burnley, V. S.** (1996). *Nonlinear Combustion Instabilities and Stochastic Sources*. Ph.D. thesis, Aeronautics Dept., California Inst. of Technology, Pasadena, CA.

22. **Butler, K. M.** and **B. F. Farrell** (1992). Three-dimensional optimal perturbations in viscous shear flows. *Physics of Fluids A*, **4**, 1637–1650.

23. **Carvalho, J. A.**, **M. A. Ferreira**, **C. Bressan**, and **L. G. Ferreira** (1989). Definition of heater location to drive maximum amplitude acoustic oscillations in a Rijke tube. *Combustion & Flame*, **76**, 17–27.

24. **Chagelishvili, G. D.**, **R. G. Chanishvili**, and **D. G. Lominadze** (1996). Physics of amplification of vortex disturbances in shear flow. *JETP Letters*, **63**, 543–549.

25. **Chagelishvili, G. D.**, **A. D. Rogava**, and **I. N. Segal** (1994). Hydrodynamic stability of compressible plane Couette flow. *Physical Review E*, **50**(6), R4283–R4285.

26. **Chatterjee, S.** (2007). Time delayed feedback control of friction induced instability. *International Journal of Non-linear Mechanics*, **42**, 1127–1143.

27. **Chu, B. T.** (1964). On the energy transfer to small disturbances in fluid flow (part 1). *Acta Mechanica*, **1**(3), 215–234.

28. **Chu, B. T.** and **L. S. G. Kovasznay** (1958). Non-linear interactions in a viscous heat-conducting compressible gas. *Journal of Fluid Mechanics*, **3**(05), 494–514.

29. **Coughanowr, D. R.**, *Process systems Analysis and Control, Second Edition*. McGrawhill, New York, 1991.

30. **Crawford, J. D.** (1991). Introduction to bifurcation theory. *Reviews of Modern Physics*, **63**, 991–1037.

31. **Crocco, L.** and **S. Cheng**, *Theory of Combustion Instability in Liquid Propellant Rocket Motors*. Butterworths Scientific Publications, London, 1956.

32. **Cuenot, B.**, **F. N. Egolfopoulos**, and **T. Poinsot** (2000). An unsteady laminar flamelet model for non-premixed combustion. *Combustion Theory & Modelling*, **4**, 77–97.

33. **Culick, F. E. C.** (1963). Stability of high-frequency pressure oscillations in rocket combustion chambers. *AIAA Journal*, **1**, 1097–1104.

34. **Culick, F. E. C.** (1968). A review of calculations for unsteady burning of a solid propellant. *AIAA Journal*, **6**, 2241–2255.

35. **Culick, F. E. C.** (1976). Nonlinear behavior of acoustic waves in combustion chambers. part i. *Acta Astronautica*, **3**, 715–734.

36. **Culick, F. E. C.** (1994). Some recent results for nonlinear acoustics in combustion chambers. *AIAA Journal*, **32**, 146–169.

37. **Culick, F. E. C.** (1997). A note on ordering perturbations and insignificance of linear coupling in combustion instabilities. *Combustion Science and Technology*, **126**, 359–379.

38. **Culick, F. E. C.**, *Unsteady motions in combustion chambers for propulsion systems*. AGARDograph, NATO, 2006.

39. **Das, S. L.** and **A. Chatterjee** (2002). Multiple scales without center manifold reductions for delay differential equations near Hopf bifurcations. *Nonlinear Dynamics*, **30**, 323–335.

40. **Dowling, A. P.** (1997). Nonlinear self-excited oscillations of a ducted flame. *Journal of Fluid Mechanics*, **346**, 271–290.

41. **Dowling, A. P.** (1999). A kinematic model of a ducted flame. *Journal of Fluid Mechanics*, **394**, 51–72.

42. **Dowling, A. P.** and **F. A. Williams**, *Sound and sources of sound*. Ellis Horwood Publishing, 1983.

43. **Drazin, P. G.** and **W. H. Reid**, *Hydrodynamic stability*. Cambridge Univeristy Press, Cambridge, 2004.

44. **Durox, D.**, **T. Schuller**, and **S. Candel** (2005). Combustion dynamics of inverted conical flames. *Proceedings of the Combustion Institute*, **30**, 1717–1724.

45. **Engelborghs, K.**, **T. Luzyanina**, and **D. Roose** (2002). Numerical bifurcation analysis of delay differential equations using dde-biftool. *ACM Transactions on Mathematical Software*, **28**, 1–21.

46. **Engelborghs, K.** and **D. Roose** (1999). Numerical computation of stability and detection of Hopf bifurcations of steady state solutions of delay differential equations. *Advances in Computational Mathematics*, **10**, 271–289.

47. **Farrell, B. F.** (1988*a*). Optimal excitation of neutral Rossby waves. *Journal of Atmospheric Science*, **45**, 163–172.

48. **Farrell, B. F.** (1988*b*). Optimal excitation of perturbations in viscous shear flow. *Physics of Fluids*, **31**, 2093–2102.

49. **Farrell, B. F.** and **P. J. Ioannou** (1993). Stochastic forcing of perturbation variation in unbounded shear and deformation flows. *Journal of Atmospheric Science*, **50**, 200–211.

50. **Farrell, B. F.** and **P. J. Ioannou** (1996). Generalised stability theory. part I: Autonomous operators. *Journal of Atmospheric Science*, **12**, 2025–2040.

51. **Farrell, B. F.** and **P. J. Ioannou** (2000). Transient and asymptotic growth of two-dimensional perturbations in viscous compressible shear flow. *Physics of Fluids*, **12**, 3021–3028.

52. **Fichera, A.**, **C. Losenno**, and **A. Pagano** (2001). Experimental analysis of thermo-acoustic combustion instability. *Applied Energy*, **70**, 179–191.

53. **Flandro, G. A.** (1995*a*). Effects of vorticity on rocket combustion stability. *Journal of Propulsion & Power*, **11**, 607–625.

54. **Flandro, G. A.**, On flow turning. *In Proceedings of 31st ASME, SAE and ASEE Joint Propulsion Conference and Exhibit*. 1995*b*.

55. **Fleifil, M.**, **A. Annaswamy**, **Z. Ghoneim**, and **A. Ghoneim** (1996). Response of a laminar premixed flame to flow oscillations: A kinematic model and thermoacoustic instability results. *Combustion & Flame*, **106**, 487–510.

56. **Giaque, A.**, **T. Poinsot**, **M. J. Brear**, and **F. Nicoud**, Budget of disturbance energy in gaseous reacting flows. *In Proceedings of the 2006 Summer Program, Center for Turbulence Research*. 2006.

57. **Gustavsson, L. H.** (1981). Resonant growth of three-dimensional disturbances in plane Poiseuille flow. *Journal of Fluid Mechanics*, **112**, 253–264.

58. **Hamilton, M. F.**, **Y. A. Illinski**, and **E. A. Zabolotskya** (2002). Nonlinear two-dimensional model for thermo-acoustic engines. *Journal of Acoustical Society of America*, **111**, 2076–2086.

59. **Hantschk, C. C.** and **D. Vortmeyer** (1999). Numerical simulation of self-excited thermoacoustic instabilities in a Rijke tube. *Journal of Sound and Vibration*, **227**, 511–522.

60. **Heckl, M. A.** (1990). Nonlinear acoustic effects in the Rijke tube. *Acustica*, **72**, 63–71.

61. **Hertzberg, J. R.** (1997). Condition for a split diffusion flame. *Combustion & Flame*, **109**, 314–323.

62. **Hillborn, R. C.**, *Chaos and nonlinear dynamics*. Oxford University Press, New York, 1994.

63. **Hireche, O.**, **C. Weisman**, **D. Baltean-Carlès**, **P. L. Quéré**, and **L. Bauwens** (2010). Low Mach number analysis of idealized thermoacoustic engines with numerical solution. *Journal of Acoustical Society of America*, **128**, 3438–3448.

64. **Hirsch, M. W.**, **S. Smale**, and **R. L. Devaney**, *Differential Equations, Dynamical Systems and an Introduction to Chaos*. Academic Press, Elsevier, 2004.

65. **Howe, M. S.**, *Acoustics of Fluid-Structure interactions*. Cambridge University Press, 1998.

66. **Jahnke, C. C.** and **F. E. C. Culick** (1994). Application of dynamical systems theory to nonlinear combustion instabilities. *Journal of Propulsion and Power*, **10**, 508–517.

67. **Jiang, G. S.** and **C. W. Shu** (1996). Efficient implementation of weighted WENO schemes. *Journal of Computational Physics*, **126**, 202–228.

68. **Juniper, M. P.** (2010). Triggering in the horizontal Rijke tube: non-normality, transient growth and bypass transition. *Journal of Fluid Mechanics*, **667**, 272–308.

69. **Kabiraj, L.**, **A. Saurabh**, **P. Wahi**, and **R. I. Sujith**, Experimental study of thermoacoustic instability in ducted premixed flames: periodic, quasi-periodic and chaotic oscillations. *In Proceedings of n3l - Int'l Summer School and Workshop on Non-Normal and Nonlinear Effects in Aero- and Thermoacoustics*. TU, Munich, 2010.

70. **Kalmar-Nagy, T.**, **G. Stepan**, and **F. C. Moon** (2001). Subcritical Hopf bifurcation in the delay equation model for Machnie tool vibrations. *Nonlinear Dynamics*, **26**, 121–142.

71. **Karimi, N.**, **M. Brear**, **S.-H. Jin**, and **J. P. Monty** (2009). Linear and nonlinear forced response of conical, ducted, laminar, premixed flames. *Combustion & Flame*, **156**, 2201–2212.

72. **Kato, T.**, *Perturbation Theory for Linear Operators*. Princeton Univeristy Press, 2005.

73. **Katto, Y.** and **A. Sajiki** (1977). Onset of oscillation of a gas-column in a tube due to the existence of heat-conduction field - a problem of generating mechanical energy from heat. *JSME Bulletin*, **20**, 1161–1168.

74. **Kedia, K. S.**, **S. B. Nagaraja**, and **R. I. Sujith** (2008). Impact of linear coupling on thermoacoustic instabilities. *Combustion Science & Technology*, **180**, 1588–1612.

75. **Kerstein, A. R.**, **W. T. Ashurst**, and **F. A. Williams** (1988). Field equation for interface propagation in an unsteady homogenous flow field. *Physical Review A*, **37**(7), 2728–2731.

76. **King, L. V.** (1914). On the convection of heat from small cylinders in a stream of fluid: Determination of the convection constants of small platinum wires, with applications to hot-wire anemometry. *Proceedings of the Royal Society of London. Series A, Containing Papers of a Mathematical and Physical Character*, **90**, 271–289.

77. **Krechetnikov, R.** and **J. E. Marsden** (2009). On the origin and nature of finite-amplitude instabilities in physical systems. *Journal of Physics A: Mathematical and Theoretical*, **42**, 412004.

78. **Kreiss, H. O.** (1971). Difference approximations for initial boundary-value problems. *Proceedings of the Royal Society A*, **323**, 255–261.

79. **Kulkarni, R.**, **K. Balasubramanian**, and **R. I. Sujith** (2011). Non-normality and its consequences in active control of thermoacoustic instabilities. *Journal of Fluid Mechanics*, **670**, 130–149.

80. **Kwon, Y. P.** and **B. H. Lee** (1985). Stability of the Rijke thermoacoustic oscillation. *Journal of the Acoustical Society of America*, **78**, 1414–1420.

81. **Langhorne, P. J.** (1988). Reheat buzz: an acoustically coupled combustion instability. part 1. experiment. *Journal of Fluid Mechanics*, **193**, 417–443.

82. **Lei, S.** and **A. Turan** (2009). Nonlinear/chaotic behaviour in thermo-acoustic instability. *Combustion Theory & Modelling*, **13**, 541–557.

83. **Levine, J. N.** and **J. D. Baum** (1993). A numerical study of nonlinear instability phenomena in solid rocket motors. *AIAA Journal*, **21**, 557–564.

84. **Lieuwen, T.** (1998). *Investigation of Combustion Instability Mechanisms in Premixed Gas Turbines*. Ph.D. thesis, Georgia Instotute of Technology, GA.

85. **Lieuwen, T.** (2002). Experimental investigation of limit-cycle oscillations in an unstable gas turbine combustor. *Journal of Propulsion & Power*, **18**, 61–67.

86. **Lieuwen, T.** and **B. T. Zinn** (1998). The role of equivalence ratio oscillations in driving combustion instabilities in low no_x gas turbines. 27^{th} *International Symposium on Combustion, the Combustion Institute*, 1809–1816.

87. **Lighthill, M. J.** (1952). On sound generated aerodynamically. I: General theory. *Proceedings of the Royal Society of London. Series A. Mathematical and Physical sciences*, **211**, 564–587.

88. **Lighthill, M. J.** (1954). The response of laminar skin friction and heat transfer to fluctuations in the stream velocity. *Proceedings of the Royal Society of London. Series A, Mathematical and Physical Sciences*, **224**, 1–23.

89. **Mack, L. M.**, *Boundary-layer stability theory*. Technical Report Doc. 900-277. JPL, 1969.

90. **Mangesius, H.** and **W. Polifke**, A simple state-space approach for the investigation of non-normal effects in thermoacoustic systems. *In Proceedings of n3l - Int'l Summer School and Workshop on Non-Normal and Nonlinear Effects in Aero- and Thermoacoustics*. TU, Munich, 2010.

91. **Mariappan, S.**, **P. J. Schmid**, and **R. I. Sujith**, Role of transient growth in subcritical transition to thermoacoustic instability in a horizontal Rijke tube. *In 16th AIAA/CEAS Aeroacoustics Conference*. AIAA, 2010. AIAA 2010-3857.

92. **Mariappan, S.** and **R. I. Sujith**, Modeling nonlinear thermoacoustic instability in an electrically heated Rijke tube. *In 48th AIAA Aerospace Sciences Meeting Including the New Horizons Forum and Aerospace Exposition*. AIAA, 2010*a*. AIAA 2010-25.

93. **Mariappan, S.** and **R. I. Sujith** (2010*b*). Thermoacoustic instability in a solid rocket motor: non-normality and nonlinear instabilities. *Journal of Fluid Mechanics*, **653**, 1–33.

94. **Matveev, K. I.** (2003*a*). A model for combustion instability involving vortex shedding. *Combustion Science and Technology*, **175**, 1059–1083.

95. **Matveev, K. I.** (2003*b*). *Thermo-acoustic instabilities in the Rijke tube: Experiments and modeling*. Ph.D. thesis, California Institute of Technology, Pasadena, CA.

96. **Matveev, K. I.** and **F. E. C. Culick** (2003). A study of the transition to instability in a Rijke tube with axial temperature gradient. *Journal of Sound & Vibration*, **264**, 689–706.

97. **McManus, K.**, **T. Poinsot**, and **S. M. Candel** (1993). A review of active control of combustion instabilities. *Progress in energy and combustion science*, **19**, 1–29.

98. **Meirovitch, L.**, *Analytical methods in vibration*. Macmillan, New York, 1967.

99. **Moler, C.**, *Numerical computing with MATLAB*. Society for Industrial and Applied Mathematics, Philadelphia, 2008.

100. **Morfey, C. L.** (1971). Sound transmission and generation in ducts with flow. *Journal of Sound & Vibration*, **14**(1), 37–55.

101. **Morse, P. M.** and **K. U. Ingard**, *Theoretical Acoustics*. McGraw-Hill, New York, 1968.

102. **Myers, M. K.** (1991). Transport of energy by disturbances in arbitrary steady flows. *Journal of Fluid Mechanics*, **226**, 383–400.

103. **Nagaraja, S. B.**, **K. S. Kedia**, and **R. I. Sujith** (2009). Characterizing energy growth during combustion instabilities: Singularvalues or eigenvalues? *Proceedings of the Combustion Institute*, **32**, 2933–2940.

104. **Nair, V.**, **S. Sarkar**, and **R. I. Sujith**, Uncertainty quantification of subcritical bifurcation in a Rijke tube. *In 16th AIAA/CEAS Aeroacoustics conference*.

105. **Nayfeh, A. H.** and **B. Balachandran** (1990). Motion near a Hopf bifurcation of a three dimensional system. *Mechanics Research Communications*, **17**, 191–198.

106. **Nayfeh, A. H.** and **B. Balachandran**, *Applied Nonlinear Dynamics*. Wiley & sons, New York, 1995.

107. **Nicoud, F.**, **L. Benoit**, **C. Sensiau**, and **T. Poinsot** (2007). Acoustic modes in combustors with complex impedances and multidimensional active flames. *AIAA Journal*, **45**, 426–441.

108. **Nicoud, F.** and **T. Poinsot** (2005). Thermoacoustic instabilities: Should rayleigh criterion be extended to include entropy changes? *Combustion & Flame*, **142**, 153–159.

109. **Nicoud, F.** and **K. Wieczorek** (2009). About the zero Mach number assumption in the calculation of thermoacoustic instabilities. *International Journal of Spray & Combustion Dynamics*, **1**, 67–111.

110. **Noiray, N.**, **D. Durox**, **T. Schuller**, and **S. Candel** (2006). Self-induced instabilities of premixed flames in a multiple injection configuration. *Combustion & Flame*, **145**, 435–446.

111. **Noiray, N.**, **D. Durox**, **T. Schuller**, and **S. Candel** (2008). A unified framework for nonlinear combustion instability analysis based on the flame descrbing function. *Journal of Fluid Mechanics*, **615**, 139–167.

112. **Orzag, S. A.** (1971). Accurate solution of the Orr-Sommerfeld stability equation. *Journal of Fluid Mechanics*, **50**, 689–703.

113. **Peracchio, A. A.** and **W. M. Proscia** (1999). Nonlinear heat-release/acoustic model for thermo-acoustic instability in lean premixed combustors. *ASME Journal of Engineering for Gas Turbines and Power-Transactions*, **121**, 415–421.

114. **Poinsot, T. J.**, **A. C. Trouve**, **D. P. Veynante**, **S. M. Candel**, and **E. J. Esposito** (1987). Vortex-driven acoustically coupled combustion instabilities. *Journal of Fluid Mechanics*, **177**, 265–292.

115. **Press, W. H.**, *Numerical recipes in FORTRAN: the art of scientific computing*. Cambridge university Press, UK, 1999.

116. **Price, E. W.** (1984). Fundamentals of solid-propellant combustion. *Progress in Astronautics and Aeronatutics*, **90**, 479–513.

117. **Putnam, A. A.**, **F. E. Belles**, and **J. A. C. Kentfield** (1986). Pulse combustion. *Progress in Energy and Combustion Science*, **12**, 43–79.

118. **Rabinowitz, P. H.**, *Applications of bifurcation theory*. Academic Press, New York, 1977.

119. **Rayleigh, L.** (1878). The explanation of certain acoustical phenomena. *Nature*, **18**, 319–321.

120. **Reddy, S. C.** and **D. S. Henningson** (1993). Energy growth in viscous channel flows. *Journal of Fluid Mechanics*, **252**, 209–238.

121. **Reinstra, S. W.** and **A. Hirschberg**, *An introduction to acoustics*. IWDE Report 92-06, 2008.

122. **Rijke, P. L.** (1859). The vibration of the air in a tube open at both ends. *Philosophical Magazine*, **17**, 419–422.

123. **Saha, A.**, **B. Bhattacharya**, and **P. Wahi** (2009). A comparative study on the control of friction-driven oscillations by time-delayed feedback. *Nonlinear Dynamics*, **60**, 15–37.

124. **Schmid, P. J.** (2007). Nonmodal stability theory. *Annual Review of Fluid Mechanics*, **39**, 129–162.

125. **Schmid, P. J.** and **D. S. Henningson**, *Stability and transition in shear flows*. Springer, 2001.

126. **Schuermans, B.**, **V. Belucci**, **F. Guethe**, **F. Meili**, **P. Flohr**, and **O. Paschereit**, A detailed analysis of thermoacoustic interaction mechanisms in a turbulent premixed flame. *In Proceedings of ASME Turbo Expo 2004: Power for Land, Sea, and Air*. 2004.

127. **Schuller, T.**, **D. Durox**, and **S. Candel** (2003). A unified model for the prediction of laminar flame transfer functions: Comparisons between conical and v-flame dynamics. *Combustion & Flame*, **134**, 21–34.

128. **Selimefendigil, F.** and **W. Polifke**, A frequency domain system model with coupled modes for limit cycle prediction of thermoacoustic systems. *In Proceedings of n3l - Int'l Summer School and Workshop on Non-Normal and Nonlinear Effects in Aero- and Thermoacoustics*. TU, Munich, 2010.

129. **Selimefendigil, F.**, **R. I. Sujith**, and **W. Polifke**, Identification of heat transfer dynamics for nonmodal stability analysis of thermoacoustic systems. *In AIP conference proceedings 1168, 2009*. 2010.

130. **Selimefendigil, F.**, **R. I. Sujith**, and **W. Polifke** (2011). Identification of heat transfer dynamics for non-modal analysis of thermoacoustic stability. *Applied Mathematics and Computation*, **217**, 5134–5150.

131. **Sen, S.**, **S. Mittal**, and **G. Biswas** (2009). Steady separated flow past a circular cylinder at low Reynolds numbers. *Journal of Fluid Mechanics*, **620**, 89–119.

132. **Seydel, R.**, *From equilibrium to chaos*. Elsevier, New York, 1988.

133. **Song, W.-S.**, **S. Lee**, **D.-S. Shin**, and **Y. Na** (2006). Thermo-acoustic instability in the horizontal Rijke tube. *Journal of Mechanical Science & Technology*, **20**, 905–913.

134. **Sterling, J. D.** and **E. E. Zukowski** (1991). Nonlinear dynamics of laboratory combustor pressure oscillations. *Combustion Science and Technology*, **77**, 225–238.

135. **Strogatz, S. H.**, *Nonlinear Dynamics and Chaos: with applications to Physics, Biology, Chemistry, and Engineering*. Westview Press, Colorado, 2000.

136. **Suresh, S.**, *Fatigue of Materials*. Cambridge University Press, 1998.

137. **Sutton, G. P.**, *Rocket Propulsion*. Wiley-IEEE, 2001.

138. **Swift, G. W.** (1988). Thermoacoustic engines. *Journal of Acoustical Society of America*, **84**, 1145–1180.

139. **Tangirala, A.**, *Responses of LTI systems*. //arunkt.yolasite.com/resources/ch3040/lectures/, 2011.

140. **Trefethen, L. N.** and **M. Embree**, *Spectra & Pseudospectra: The behavior of nonnormal matrices and operator*. Princeton University Press, 2005.

141. **Trefethen, L. N.**, **A. E. Trefethen**, **S. C. Reddy**, and **T. A. Driscoll** (1993). Hydrodynamic stability without eigenvalues. *Science*, **261**, 578–5851.

142. **Tulsyan, B.**, **K. Balasubramanian**, and **R. I. Sujith** (2009). Revisiting a model for combustion instability involving vortex shedding. *Combustion Science & Technology*, **181**, 457–482.

143. **Tyagi, M.**, **S. R. Chakravarthy**, and **R. I. Sujith** (2007*a*). Unsteady response of a ducted non-premixed flame and acoustic coupling. *Combustion Theory & Modelling*, **11**, 205–226.

144. **Tyagi, M.**, **N. Jamadar**, and **S. R. Chakravarthy** (2007*b*). Oscillatory response of an idealised two-dimensional diffusion flame: Analytical and numerical study. *Combustion & Flame*, **149**, 271–285.

145. **van Kampen, J. F.** (2006). *Acoustic pressure oscillations induced by confined turbulent premixed natural gas flames*. Ph.D. thesis, University of Trente.

146. **Vidyasagar, M.**, *Nonlinear System Analysis*. Prentice-Hall, New Jersey, 1993.

147. **Wahi, P.** and **A. Chatterjee** (2005). Regenerative tool chatter near a codimension 2 Hopf point using multiple scales. *Nonlinear Dynamics*, **40**, 323–338.

148. **Watanabe, M.**, **A. Prosperetti**, and **H. Yuan** (1997). A simplified model for linear and nonlinear processes in thermoacoustic prime movers. part i. model and linear theory. *Journal of Acoustical Society of America*, **102**, 3484–3496.

149. **Waugh, I.**, **M. Geu**β, and **M. Juniper** (2011). Triggering, bypass transition and the effect of noise on a linearly stable thermoacoustic system. *Proceedings of the Combustion Institute*, **33**, 2945–2952.

150. **Waugh, I. C.**, **M. P. Juniper**, and **M. Geuss**, Triggering in a thermoacoustic system with stochastic noise. *In Proceedings of n3l - Int'l Summer School and Workshop on Non-Normal and Nonlinear Effects in Aero- and Thermoacoustics*. TU, Munich, 2010.

151. **Weiczorek, K.** (2010). *Numerical study of Mach number effects on combustion instability*. Ph.D. thesis, University of Montpellier, France.

152. **Wicker, J. M.**, **W. D. Greene**, **S. I. Kim**, and **V. Yang** (1996). Triggering of longitudinal combustion instabilities in rocket motors: nonlinear combustion response. *Journal of Propulsion & Power*, **12**, 1148–1158.

153. **Wieczorek, K.**, **C. Sensiau**, **W. Polifke**, and **F. Nicoud**, Assessing non-normal effects in thermoacoustic systems with non-zero base flow. *In Proceedings of n3l - Int'l Summer School and Workshop on Non-Normal and Nonlinear Effects in Aero- and Thermoacoustics*. TU, Munich, 2010.

154. **Wolf, A.**, **J. B. Swift**, **H. L. Swinney**, and **A. J. Vastano** (1985). Determining Lyapunov exponents from a time series. *Physica* D, **16**, 285–317.

155. **Wright, T. G.**, *EigTool*. http://www.comlab.ox.ac.uk/pseudospectra/eigtool/, 2002.

156. **Wu, X.**, **M. Wang**, **P. Moin**, and **N. Peters** (2003). Combustion instability due to nonlinear interaction between sound and flame. *Journal of Fluid Mechanics*, **497**, 23–53.

157. **Yang, V.**, **S. I. Kim**, and **F. E. C. Culick** (1990). Triggering of longitudinal pressure oscillations in combustion chambers, i. nonlinear gas dynamics. *Combustion Science & Technology*, **75**, 183–214.

158. **Yoon, H. G.**, **J. Peddison**, and **K. R. Purdy** (2001). Nonlinear response of a generalized Rijke tube. *International Journal of Engineering Science*, **39**, 1707–1723.

159. **You, D.**, **Y. Huang**, and **V. Yang** (2005). A generalized model of acoustic response of turbulent premixed flame and its application to gas-turbine combustion instability analysis. *Combustion Science & Technology*, **177**, 1109–1150.

160. **Yuan, H.**, **S. Karpov**, and **A. Prosperetti** (1997). A simplified model for linear and nonlinear processes in thermoacoustic prime movers. part ii. nonlinear oscillations. *Journal of Acoustical Society of America*, **102**, 3497–3506.

161. **Zhang, S.** and **C. W. Shu** (2007). A new smoothness indicator for the WENO schemes and its effects on the convergence to steady state solutions. *Journal of Scientific Computing*, **31**, 273–305.

162. **Zhong, X.** (1998). Upwind compact and explicit high order finite difference schemes for direct numerical simulation of high speed flows. *Journal of Computational Physics*, **144-2**, 662–709.

163. **Zinn, B. T.** and **T. C. Lieuwen**, *Combustion instabilities: Basic concepts - Combustion Instabilities in Gas Turbine Engines: Operational Experience, Fundamental Mechanisms, and Modeling*. AIAA, USA, 2006.

164. **Zinn, B. T.** and **M. E. Lores** (1971). Application of the Galerkin method in the solution of non-linear axial combustion instability problems in liquid rockets. *Combustion Science & Technology*, **4**, 269–278.

LIST OF PAPERS BASED ON THESIS

1. Subramanian, P. and R. I. Sujith (2011). Non-normality & internal flame dynamics in premixed flame-acoustic interaction, *accepted for publication with the Journal of Fluid Mechanics*.

2. Subramanian, P., S. Mariappan, R. I. Sujith & P. Wahi (2010). Bifurcation analysis of thermoacoustic instability in Rijke tube, *International Journal of Spray and Combustion Dynamics*, **2** (4), 325-356.